Synthetic and natural polymer precursor derived hierarchically porous conducting carbon and its Co_3O_4-based nanocomposite for electrochemical energy storage applications

Thesis Submitted to AcSIR for the Award of the Degree of

DOCTOR OF PHILOSOPHY
In Physical Sciences

By

Dhanya P

Registration Number: 10PP11J26131

Research Guide
Dr. Satishchandra Ogale

Research Co-guide
Dr. Sreekumar Kurungot

CSIR-National Chemical Laboratory, Pune-411008, India

2015

Certificate

This is to certify that the work incorporated in this Ph.D. thesis entitled **"Synthetic and natural polymer precursor derived hierarchically porous conducting carbon and its Co_3O_4-based nanocomposite for electrochemical energy storage applications"** submitted by **Ms. Dhanya P** to Academy of Scientific and Innovative Research (AcSIR) in fulfillment of the requirements for the award of the Degree of **Doctor of Philosophy in Physical Sciences,** embodies original research work under my supervision. I further certify that this work has not been submitted to any other University or Institution in part or full for the award of any degree or diploma. Research material obtained from other sources has been duly acknowledged in the thesis. Any text, illustration, table etc., used in the thesis from other sources, have been duly cited and acknowledged.

Research Student

Ms. Dhanya P

Research Guide

Dr. Satishchandra Ogale

Research Co-guide

Dr. Sreekumar Kurungot

Declaration

I hereby declare that the thesis entitled **"Synthetic and natural polymer precursor derived hierarchically porous conducting carbon and its Co_3O_4-based nanocomposite for electrochemical energy storage applications"** submitted for the degree of **Doctor of Philosophy** in **Physical Sciences** to the Academy of Scientific & Innovative Research (AcSIR), has been carried out by me at the Physical and Materials Chemistry Division of National Chemical Laboratory, Pune under the guidance of **Dr. Satishchandra Ogale and Dr. Sreekumar Kurungot**. Such material as obtained from other sources has been duly acknowledged in this thesis. The work is original and has not been submitted in part or full by me for any other degree or diploma to other University.

Date
National Chemical Laboratory,
Pune - 411008

Research Student
Dhanya P

Acknowledgment

I take this opportunity to thank each and every one who has been instrumental in the completion of my PhD research and thesis directly or indirectly.

Foremost, I am thankful to the God Almighty for fulfilling my dream and being with me all the way.

I express my deep gratitude and special appreciation to my research supervisor Dr. Satishchandra Ogale for his able guidance, support and constant encouragement. His patience, immense knowledge and timely advice were helpful for the successful completion of this work in the available time frame. I would also like to thank my co-supervisor Dr. Sreekumar Kurungot for his constant support, encouragement and comforting influence.

I express my gratitude to doctoral advisory committee members, Dr. Chinnakonda Gopinath, Dr. (Mrs) Manjusha V Shelke, and Dr. Sarika M Bhattacharya for their insightful comments and important suggestions during course work evaluations and presentations. I take this opportunity to thank Dr. S. Sivram and Dr. Sourav Pal (former Directors, CSIR-NCL), Dr. Vijayamohanan K Pillai (Director, CSIR-NCL), Dr. Vivek Ranade (Dy. Director, CSIR-NCL), and Dr. Anil Kumar (Head of Physical and Materials Chemistry Division) for providing the infrastructure and advanced facilities for research and giving me an opportunity to work at CSIR-NCL. I am thankful to Council for Scientific and Industrial Research, Govt. of India for providing me with research fellowships during my PhD study period.

I would further like to acknowledge the immense help of Dr. Madhavi Srnivasan, and Dr. Vanchiappan Aravindan from NTU, Singapore, and Mr. Sreekuttan M. Unni and Dr. Bihag for all the help and support during the course of the research work.

I am also thankful to Mr. Ravi Pandit (Co-founder, Chairman and Group CEO of KPIT Technologies Ltd.) and Mr. Tejas Kshatriya for giving me an opportunity to take part in a project with KPIT on developing energy storage technology for hybrid electric vehicles.

I take this opportunity to express my deep gratitude to all the faculties of the Department of Physics, University of Calicut for their teaching in giving me a strong

background in physics and their encouragement to pursue research career. I would like to thank all my teachers from MES KVM College for their constant motivation, support and help during my B.Sc. days.

I wish to also thank staff members from the Centre for Materials Characterization for helping with different characterizations such as X-ray diffraction, Raman Spectroscopy, SEM, HRTEM and XPS. My thanks are also due to Dr. Rahul Banerjee and his students Suman, Arjun and Sharath for the BET surface area measurements.

I deeply acknowledge my laboratory seniors/friends Dr. Vivek Dhas, Dr. Subas Muduli, Dr. Abhimanyu Rana, Dr. Arif Shaikh, Dr. Parvez Shaikh, Dr. Vivek Antad, Dr. Harish Gholap, Dr. Ashish, Dr. Sambhaji, Dr. Prasad, Dr. Onkar, Dr. Datta, Dr. Rohan, Dr. Abhik, Dr. Mandakini, Dr. Sarika, Dr. Meenal Deo, Dr. Shruti, Dr. Lily, Vishal, Pradeep, Anil, Wahid, Yogesh, Umesh, Reshma, Dipti, Rounak, Satyawan, Aniruddha, Divya, Pooja, Shraddha, Mukta, Dr.Supriya, Ketaki, Dr.Nilima, Upendra, Kush, Sumit, Tanya, Poonam, Srashti, Ishita, Shital, Swati, Golu, Roma, Dr. Monika, Dr. Surendar, Kaustubh, Varun, Rajesh, Kingshook and Neha for creating a wonderful laboratory atmosphere and co-operation during the research work. Special thanks to Ajay, Harshita, Bini, Neha and Jensheer for their tremendous help during my work as a part of their internship.

I take this opportunity to thank my NCL friends Sreekuttan, Jijil, Beena, Bihag, Anjali, Jaya, Prajitha, Jhumur, Sushma and Manasi for creating a happy environment during my PhD.

Words are not enough to express my deep sense of gratitude to my parents for their love, affection and support throughout my life. I also wish to express my love for my sisters for their support and encouragement and sharing my joys and sorrows always. I am also thankful to my grandmother, cousins and other relatives for their help and best wishes.

Though, many have not been mentioned by name, I commemorate their help and support throughout.

Dhanya

List of Abbreviations

Abbreviation	Name
AC	Activated Carbon
BET	Brunauer–Emmett–Teller
CAC	Commercial Activated Carbon
CNS	Carbon nanosphere
CNFs	Carbon Nano Fibers
CNTs	Carbon Nanotubes
CV	Cyclic Voltammogram
CVD	Chemical Vapour Deposition
DMF	Dimethylformamide
EDAX	Energy dispersive Analysis of X-rays
EDLC	Electrochemical double layer capacitor
EES	Electrical Energy Storage
EIS	Electrochemical Impedance Spectroscopy
ESR	Equivalent Series Resistance
EV	Electric Vehicle
FE SEM	Field emission scanning electron microscopy
FWHM	Full width at half maximum
HEV	Hybrid Electric Vehicle
HR TEM	High resolution transmission electron microscopy
HTC	Hydrothermal Carbonization
IMPC	Interconnected Microporous Carbon
Li-HEC	Lithium ion hybrid electrochemical capacitor
LIBs	Lithium ion batteries

MWNTs	Multi-walled carbon nanotubes
NMP	N-Methyl-2-Pyrrolidone
PAN	Polyacrylonitrile
PG	Porous Graphene
PTFE	Poly tetrafluoro-ethylene
PVA	Poly Vinyl Alcohol
PVDF	Polyvinylidene fluoride
SAED	Selected Area Energy Dispersive
SWNTs	Single-walled carbon nanotubes
SEM	Scanning electron microscopy
TEM	Transmission electron microscopy
TGA	Thermogravimetric analysis
UV	Ultraviolet
WPC	Waste paper derived Carbon
XPS	X-ray photoelectron Spectroscopy
XRD	X-ray diffraction

Content

Abstract

In recent years, the rapidly growing demand for energy has accelerated research efforts on clean and sustainable energy technologies because of environmental concerns that arise due to usage of conventional fuels. Growing realization about hazards of this approach has driven communities to think and act seriously about enhancing the use of green energy in the all sectors of energy usage. Although energy conversion technologies appear to have matured fairly well, the time domains of harvesting renewable energies and their usage do not necessarily coincide and hence large scale and efficient energy storage and retrieval are a huge necessity and invite much further research.

Electrochemical energy storage systems have emerged as promising solutions for efficient storage of energy for the future. Li-ion battery and supercapacitor are two important ones among them. Supercapacitors have the advantages of very high power density and stability, whereas Li-ion battery offers the benefit of very high energy density though with a relatively lower power density. Supercapacitors store energy by surface adsorption of electrolyte ions and hence exhibit fast charge/discharge and cyclic stability. In Li ion batteries the charge storage occurs in the bulk of the material and hence they possess higher energy density. The major disadvantage of supercapacitors is their lower energy density and this limits their large scale commercial use. Increasing the energy density of supercapacitor without compromising its power density is still a big challenge for the researchers. Varieties of carbon materials have already been explored as active materials for the electrodes of supercapacitors. The charge storage capacity and energy density can be increased by increasing the surface area and tuning the porosity in the material with optimum mesopore to micropore ratio. The energy density of Li-ion battery can be further improved by replacing electrodes by comparatively higher capacity electrodes. Current Li-ion battery uses graphite as anode which has a theoretical capacity of 372mAhg^{-1}. Transition metal oxides with multiple valences possess higher theoretical capacity. However the major drawbacks are lower power density and stability due to lower electrical conductivity of oxides. This can be solved by making composite of the active material with carbon nanoforms such as graphene, CNT and CNF. This helps to improve the conductivity as well as the accessible surface area of electrode. The energy density of supercapacitor can be improved either by increasing the charge storage

capacity, operating potential window, or both. The charge storage capacity of carbon material can be further improved by tuning the properties such as porosity, surface area, functional groups and electrical properties.

The main focus of this thesis is on the development of high surface area conducting porous carbons from natural and synthetic polymer and their applications as active materials in or active material support for the electrochemical energy storage devices. Thus 3D porous carbon was derived from various carbonaceous precursors and tested for electrode material for double layer capacitor and support for active material for Li-ion battery anode material. The thesis demonstrates that 3D porous carbon can be synthesized without using any external activation agent or template using alkali metal salt of polymer as the source for carbon as well as activation agent. Furthermore use of the white waste office printing paper was also made as a precursor for the synthesis of 3D porous carbon for the supercapacitor electrode. Hydrothermal carbonization followed by high temperature pyrolysis in the presence activation agent was performed to obtain the porous carbon. This material also performed well as an electrode for double layer capacitor and cathode for Li-ion hybrid supercapacitor. Three dimensional porous graphene with hierarchical porosity in the form of hexagonal porous structure was also synthesized from sodium salt of polymer. Composite of the 3D porous graphene with Co_3O_4 was developed for Li-ion battery anode.

The importance of green energy and electrochemical energy storage system is discussed briefly in **chapter 1**. It also discusses different types of energy storage devices in detail along with their properties, advantages and drawbacks. Different electrode materials that have been explored as electrode materials for supercapacitors and Li-ion batteries, and the specific importance 3D porous carbon forms in this context are also discussed.

A brief description on the basic synthesis protocols and characterization techniques used in the work reported in the thesis is given in **chapter 2**

Chapter 3 deals with non-templated synthesis of interconnected microporous carbon (IMPC) sheets having beehive type morphology by direct pyrolysis of poly(acrylamide-co-acrylic acid) potassium salt in an inert atmosphere without any external activation agent. The presence of the alkali metal in the selected polymer precursor results in a high specific surface area of 1327 m^2g^{-1}. Importantly, 80% of the pore volume is contributed

by micropores with pore size ranging from 1–2 nm which is ideal for use as a material for the electrode of a supercapacitor. The rest of the accessible surface area is contributed by the small fraction of mesopores and macropores due to the interconnected structure. The presence of three different types of pores makes the material ideal for supercapacitor electrodes. The IMPC was tested as an electrode in aqueous and non-aqueous supercapacitors. The material also showed better performance as cathode material for Lithium-ion hybrid capacitor in comparison with commercial supercapacitor carbon.

In chapter 4, hydrothermal processing followed by controlled pyrolysis of waste (used) white office paper (a globally collectable shredded paper waste) was performed to obtain high surface area carbon with hierarchical pore size distribution. The BET specific surface area of such carbon is 2341 m^2g^{-1}. The interconnected macroporous structure along with the concurrent presence of mesopores and micropores makes the material ideal for ultracapacitor application. Such waste paper derived carbon (WPC) shows remarkable performance in all solid-state supercapacitor fabricated with ionic liquid-polymer gel electrolyte. The Li-ion electrochemical capacitor constructed using WPC as cathode also shows an excellent energy storage capacity of 61 $Whkg^{-1}$.

Increased surface to volume ratio and tunable electronic and optical properties of nanomaterials have expanded their use in a variety of applications, importantly the energy conversion and storage applications. **Chapter 5** reports synthesis of Co_3O_4/porous graphene (PG) nanocomposite by a simple solvothermal route and its application as Li-ion battery anode. The ratio of graphene to Co_3O_4 is optimized to get its best possible performance. Amongst the different compositions investigated, the composite PG-600 (with 50% PG) shows a discharge capacity of 700 mAh g^{-1} at a current density of 500 mAg^{-1} and maintains 90% retention after 80 cycles. The high surface area of PG sheets helps the Co_3O_4 nanoparticles to form a uniform dispersion on it. The increased surface area and electrical conductivity of the composite result into an enhancement in the capacity, cycling stability and rate capability as compared to native Co_3O_4 phase.

Chapter 6 provides an overall conclusion of the research work presented and discussed in different chapters. Furthermore this chapter also discusses some future directions for research work in the field of electrical energy storage.

Chapter 1

Introduction

This chapter gives a basic introduction to the premise of the research work described in this thesis. A broad introduction to the renewable energy and different types of electrical energy storage devices and their importance and drawbacks are presented. The role of carbon materials and their functional composites in such charge storage systems is also highlighted. This chapter also lays out a roadmap for the direction of research presented in this thesis.

1.1 Need for renewable green energy technologies

Explosive increase in the world population demands a non-linear increase in the global energy needs. But the fossil fuel reserves which are considered as the backbone of modern societies are not sufficient to support the current and more importantly the future energy needs. The depletion of fossil fuel reserves on earth is one aspect which has led us to think of the new and renewable alternatives. The indiscriminate use of the remaining reserves to go hand in hand with the energy demands has aggravated the global energy problem even further due to the corresponding severe and negative environmental impact. The green-house gas emission has been the worst possible offshoot of the current unsustainable strategy. Figure 1.1a shows fossil fuel reserves on earth available till 2081. It has become a major challenge to meet the energy requirements for development and improved life style without causing any environmental pollution.[1] Figure 1.1b shows an increase in the CO_2 emission in the past 30 years.

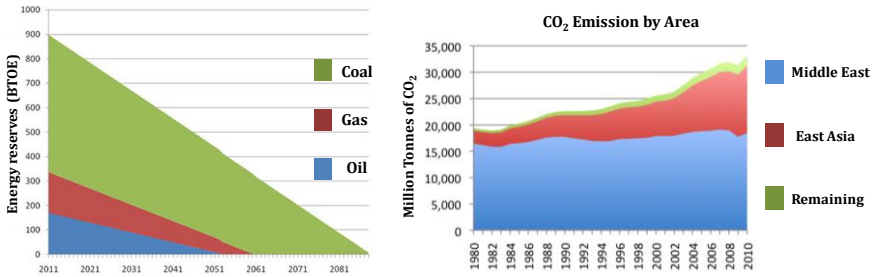

Figure 1.1 (a) Fossil fuel reserve available till 2081 (https://www.ecotricity.co.uk/our-green-energy/energy-independence/the-end-of-fossil-fuels) and **(b)** graph representing increase in the CO_2 emission from 1980-2010 (http://ourfiniteworld.com/2011/11/30/thoughts-on-why-energy-use-and-co2-emissions-are-rising-as-fast-as-gdp/)

Search towards greener and safer energy alternatives has pushed an intensive research towards the development of low cost, environmentally benign and energy efficient technologies from renewable sources.[2, 3] The different forms of renewable energy sources are discussed below. Figure 1.2 shows a schematic of different forms of such renewable sources of energy.

1.1.1 Solar Energy: Solar energy is considered to be one of the potential sources of energy to meet the human requirement in the future considering the large amount solar energy available on earth every day and everywhere.[4] Technologies for generating electrical energy from light energy have already been developed in various countries. Continuous effort on improving the performance of such photovoltaic technologies with reduction in the production cost has resulted in the reduction of total cost of the device. However, photovoltaic technology still lacks the suitability for many applications because of its rather low power conversion efficiency. Research is still being conducted for developing solar cells with high photon conversion efficiency.[5]

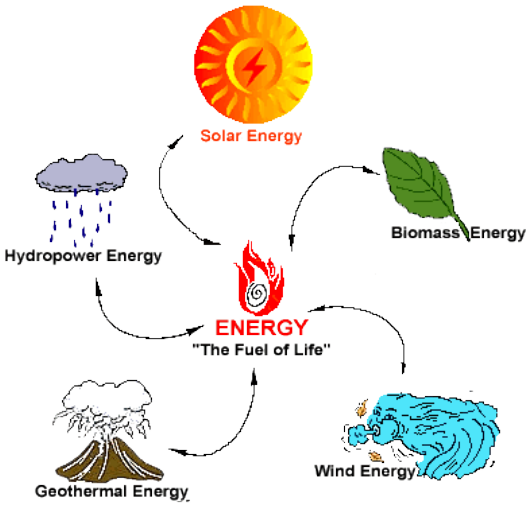

Figure 1.2 Different forms of renewable energy
(http://www.thefuture.net.nz/alternative.htm)

1.1.2 Wind power: In this, mechanical or electrical energy is produced from the air flow using wind turbines. This technology has already been established by many countries around the world for generating electrical energy at grid level.[6]

1.1.3 Tidal power: The energy in tides is converted into electrical energy through different methods named as tidal steam generator, tidal barrage, dynamic tidal power and tidal lagoon. The main disadvantages of tidal power are its high operating cost and limited areas with high speed tides. However the tidal power technology is still trying to improve in terms of cost and efficiency.[7]

Direct use of electrical energy generated from renewable sources for many applications (mobile applications such as electric vehicles, portable electronics) is

still a challenge. The primary solution is to develop an efficient and robust device to store the energy generated as the duration over which the energy being harvested from the renewable sources is not necessarily the duration over which it is required or used.[8] The commonly used electrical energy storage systems (EES) are batteries and electrical capacitors.[9] Normal parallel plate capacitors store energy by electric field induced dielectric polarization and the storage and retrieval are quite fast. However the values of maximum capacitance in such cases are quite low to really serve as any effective storage device for important applications. Supercapacitors on the other hand store energy directly in the form of electric charges through surface adsorption and hence they possess high power density and stability. However, since the charges are stored only on the surface of electrodes, they have less energy density. Batteries store energy through reversible electrochemical reactions. Since the bulk of the electrodes are involved in the reaction process they possess very high energy density. Being a bulk process however they suffers from limitations of lower power density and limited cyclic stability. To overcome these limitations intense research is still going on new and novel energy storage technologies by developing new materials and designs to improve their performance to meet the requirements of the modern world for electric/hybrid vehicles (non-polluting) and portable electronics.[10]

1.2 Classification of energy storage devices

The performance of energy storage devices are evaluated based on different parameters such as charge storage capacity, operating voltage, energy density, power density and cyclic stability.[9]

The energy storage devices are classified on the basis of factors like storage mechanism and performance. Figure 1.3 shows a plot known as Ragone plot that compares the energy density and power density of various types of storage devices and corresponding applications.[11]

Table 1.1 compares the characteristics of different energy storage systems (dielectric capacitors, supercapacitors and Li-ion batteries).

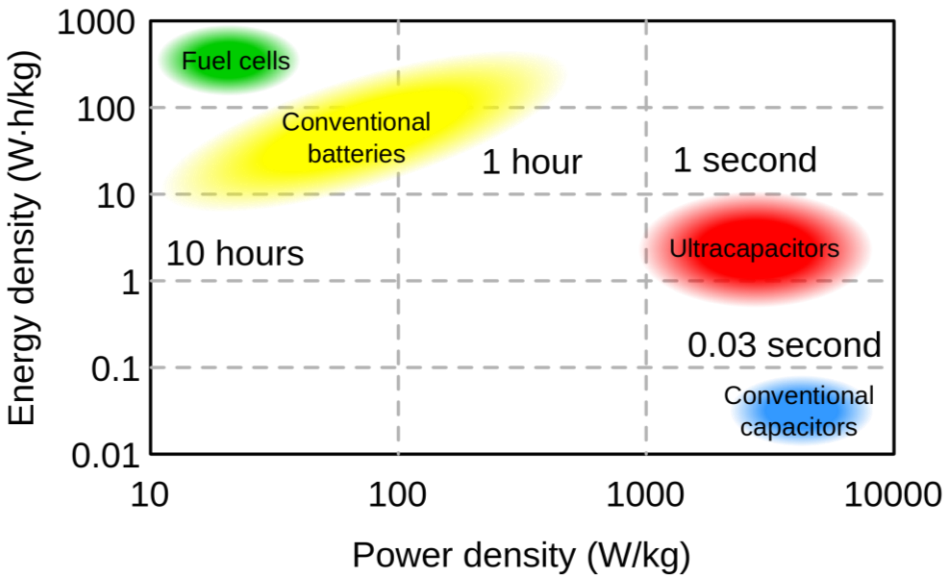

Figure 1.3 The Ragone plot comparing the specific energy and specific power of different energy storage system (https://en.wikipedia.org/wiki/Ragone_chart)

Parameter	Supercapacitors	Capacitors	Batteries
Energy storage	W-second of energy	W-second of energy	W-hour of energy
Charge Methods	Voltage across terminal	Voltage across terminal	Constant current & constant Voltage
Power Delivered	rapid discharge, linear or exponential voltage decay	rapid discharge, linear or exponential voltage decay	Constant Voltage over long time period
Charge/Discharge Time	ms to s	ps to ms	1 to 10 h
Form factor	small	small to large	small to large
Weight	1 g to 2 g	1 g to 10 kg	1 g to 10 kg
Energy Density	1 to 5 Wh/kg	0.01 to 0.05 Wh/kg	8 to 600 Wh/kg
Operating Voltage	2.3 V to 2.75 V /cell	6 V to 800 V /cell	1.2 V to 4.2 V /cell
Lifetime	>100K cycles	>100K cycles	150 to 1500 cycles
Operating Temp	-40 to +85^{0}C	-20 to +100^{0}C	-20 to +65^{0}C

Table 1.1 Comparison of different parameters of dielectric capacitors, supercapacitors and batteries

1.2.1 Dielectric Capacitors (Ceramic Capacitor):

A dielectric capacitor consists of two metal plates separated by a thin dielectric medium. When a potential difference is applied between the two electrodes, electric field is developed across dielectric medium with the dielectric medium undergoing polarization and charges moving towards electrodes with opposite polarity. The schematic of a parallel plate dielectric capacitor is shown in the figure 1.4.

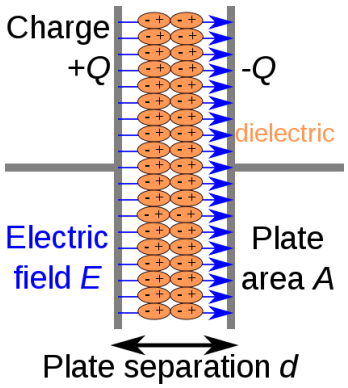

Figure 1.4 Schematic representation of parallel plate dielectric capacitor (https://en.wikipedia.org/wiki/Dielectric)

For a capacitor, the charge stored is expressed in terms its capacitance given by the equation

$$C = \frac{Q}{V}$$

Where Q is the magnitude of the charge stored on each metal plate and V the potential difference between them.

The simplest configuration of a capacitor consists of two conducting plates parallel to each other separated by a dielectric medium. The capacitance of a parallel plate capacitor can be expressed as

$$C = \frac{\varepsilon A}{d}$$

Where ε the permittivity of the dielectric is medium, A is the area of each metal plate and d is the distance between them. The capacitance increases with increase in the area of the metal plate and decreasing the inter-electrode distance. The maximum amount of the energy stored in a capacitor of capacitance C is

$$E = {}^{1}/_{2}\, CV^{2}$$

Where, V is the breakdown (or highest possible applicable) voltage of the capacitor. The energy varies linearly with capacitance and square of the breakdown voltage. The major drawback of this kind of capacitors is its lower energy storage capacity although they possess high power density. The capacitance and hence the energy density can be increased by increasing the surface area of the electrode and decreasing the distance between the electrodes.

1.2.2 Supercapacitors

1.2.2.1 Historical Background

Supercapacitors, also known as ultracapacitors, are electrochemical energy storage devices that store energy in the form of electrical charges at the electrode-electrolyte interface.[12] The first electrolytic capacitor was developed by H. Becker of General Electric Corp. in 1957 and the electrical double layer capacitor was developed by Robert A. Rightmire in 1966 using high surface area porous carbon electrodes and organic electrolyte. This technology was commercialized by Nippon Electric Company Limited. Initially the supercapacitors were used as the backup for computers because of its lower energy density. Metal oxide based supercapacitor was first developed by B. E. Conway and co-workers and such supercapacitors are known as pseudocapacitors. Panasonic made the first commercial supercapacitor in 1978 with a brand name of Goldcaps. Current supercapacitor industry is 1000 million dollar worth and is expected to be 3.5 Billion by 2020. The current major supercapacitor manufacturers are Maxwell technologies, Nesscap, loxus etc. Figure1.5 shows the commercial supercapacitors from Maxwell Supercapacitors for different ranges of capacitance and operating voltage values.

In the Ragone plot supercapacitors have an intermediate energy and power density that can bridge the gap between the conventional dielectric capacitors and batteries.[13] The major advantages of supercapacitors over batteries are their high power density, wide operation temperature range and long cyclic stability.

Figure 1.5 Commercial supercapacitors from Maxwell supercapacitors (http://www.maxwell.com/products/ultracapacitors/)

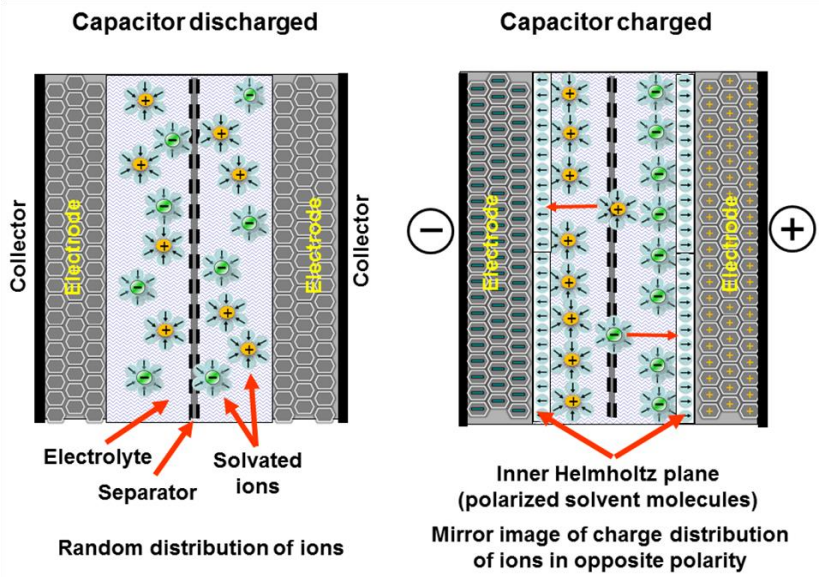

Figure 1.6 Schematic representing the mechanism of charging and discharging in a supercapacitor (https://en.wikipedia.org/wiki/Supercapacitor)

Figure1.6 shows the schematic for a typical supercapacitor. These have conducting high surface area carbon electrodes with an electrolyte sandwiched between them. The two electrodes are separated by an electrically insulating "separator" which can pass ions but not electrons. The two interfaces formed at two electrode surfaces form electric double layers leading to high capacitance at each end. Note that the dielectric separation in the double layer is of the order of nanometer; hence the capacitance at each electrode is extremely high. This construction acts as two capacitors connected

in series and hence the effective capacitance of the supercapacitor device can be expressed as

$$C = \frac{C_1 \times C_2}{C_1 + C_2}$$

Where, C_1 and C_2 are the capacitance values of the individual electrodes. When both the electrodes have the same materials type and same amount of material loading the capacitance of both electrodes will be equal and effective capacitance of the capacitor will be equal to

$$C = \frac{C_1}{2}$$

Figure 1.7 shows the classification of supercapacitors. Supercapacitors are basically classified into two categories known as electrical double layer capacitor and pseudocapacitor based on the charge storage mechanisms involved as discussed below in details.[14]

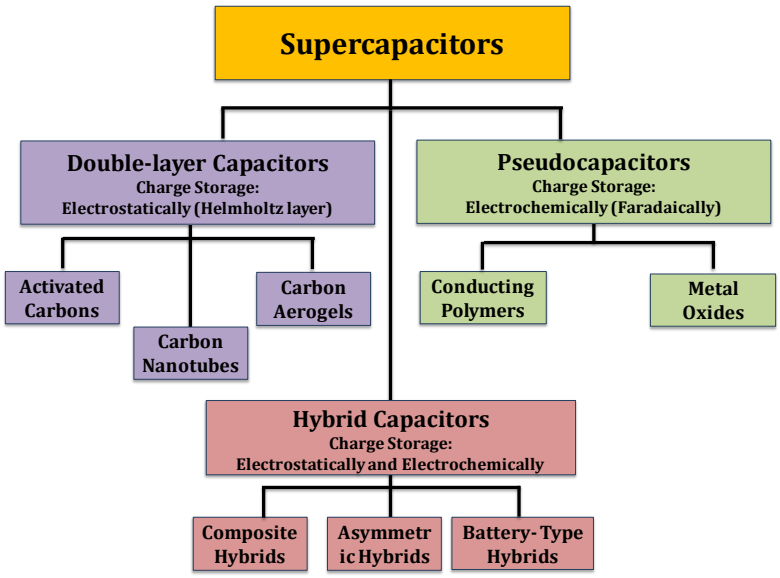

Figure 1.7 Taxonomy of supercapacitors according to charge storage mechanism

1.2.2.2 Electrical Double Layer Capacitors (EDLC):

Electrical double layer is a boundary formed between an electrode and an electrolyte. A potential difference is generated (due to differences in the chemical potentials) when a solid electrode and liquid electrolyte come in contact with each other. This potential difference results into the formation of a double layer at the interface

through redistribution of charges. In the first layer the electrolyte ions are adsorbed on the surface of the solid electrode through strong electrostatic interaction, whereas the second layer consists of ions which are loosely bound to the surface via the first layer. The structure of double layer depends on various factors including characteristics of the electrode material (surface area) and the electrolyte (solvent, electrolyte ion etc.). The double layer has been explained by different models such as Helmholtz double layer model, Diffuse Layer Model and Stern model. Stern model combines Helmholtz model with diffuse layer model as both fail to explain the capacitance at a highly charged surface. Figure 1.8 shows the schematic for a double layer model at the interface of a negatively charged electrode. This model suggested the existence three regions which includes the inner Helmholtz plane (IHP) that passes through the center of specifically adsorbed ion, the outer Helmholtz plane (OHP) that refer to the distance of closest approach for the solvated ions and the diffuse layer beyond OHP.

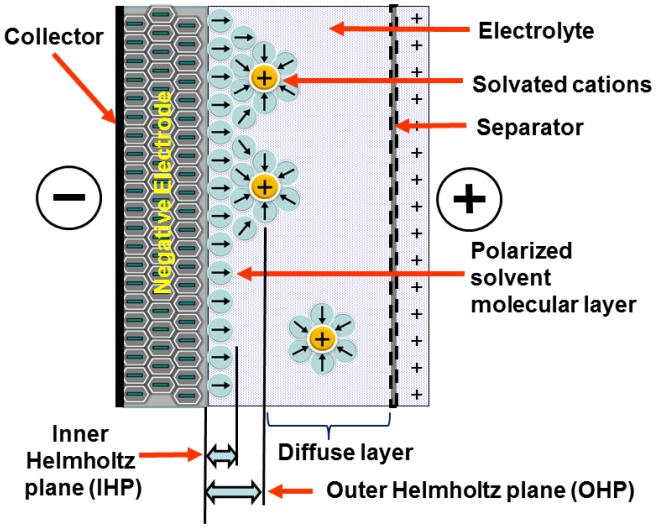

Figure 1.8 Schematic representation of electrical double layer model at the interface of a negatively charged electrode (http://www.wikiwand.com/en/Double-layer_capacitance)

In an electrical double layer capacitor the energy is stored at the electrode-electrolyte interface through reversible adsorption of electrolyte ions on the surface of the electrodes. EDLCs are also known as non-faradaic supercapacitors as there is no electrochemical reaction involved.[15] The adsorption of electrolyte ions at the Helmholtz plane parallel to the electrode surface results in double layer formation called Helmholtz double layer as shown in the figure 1.8. When a potential difference

is applied between the two electrodes, solvated electrolyte ions move towards the electrodes with opposite polarity.

Figure 1.9 shows the mechanism of charging discharging in EDLC.[16] The double layers formed at each interface acts as two parallel plate capacitors connected in series. Hence the capacitance of a supercapacitor is also directly proportional to the surface area of the electrode and inversely proportional to the thickness of the double layer on each side.

Supercapacitors have both gravimetric and areal capacitances much higher than that of conventional capacitors. This is because of the close charge separation of approximately 5 Å for the compact layer and 1000 Å for the outer layer which is much less than the separation between the metal plates in a conventional capacitor which is of the order of 5 μm. Apart from this, the high surface area electrode materials also increase the area for charge storage. Supercapacitors thus possess higher energy density as compared to that of conventional capacitors as the energy density of a capacitor is directly proportional to capacitance according to the equation $E = {}^{1}/_{2}\, CV^{2}$.[17]

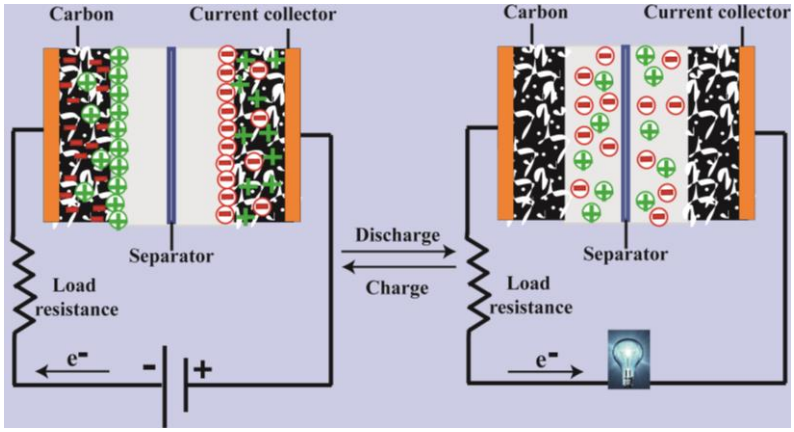

Figure 1.9 Schematic of mechanism of charging discharging in an electrical double layer capacitor

Since only the surface of the electrodes are involved in the charge storage, the adsorption of electrolyte ions are highly reversible and have very less response time to potential change. Hence they have high cyclic stability and can be charged or discharged at a fast rate.

However the major disadvantage of supercapacitor as compared to batteries which rely on bulk redox reactions in the material is lower energy density because of the inaccessibility to bulk of the material. The energy density of the supercapacitor can be improved either by increasing the operating potential or by increasing the capacitance. Researchers have explored materials that store charges through fast and reversible redox reactions at the surface instead of surface adsorption. Such supercapacitors are called pseudocapacitors.

1.2.2.3 Pseudocapacitors

In pseudocapacitors charges are stored at the electrode surface by reversible redox reactions. Since electrochemical reactions are involved, it is also known as faradaic supercapacitor.[18] Because of the charge transfer through faradaic reactions involved, more amount of charge can be stored and hence pseudocapacitors possess higher specific capacitance than EDLCs.

Figure 1.10a and b show the charge storage mechanism and cyclic voltammogram for a pseudocapacitor, respectively. Metal oxides and conducting polymers are the most widely explored materials for pseudocapacitors. MnO_2 and RuO_2 are most explored metal oxides for pseudocapacitors due to their various properties such as high theoretical capacitance, fast redox reactions, higher operating potential and stability.

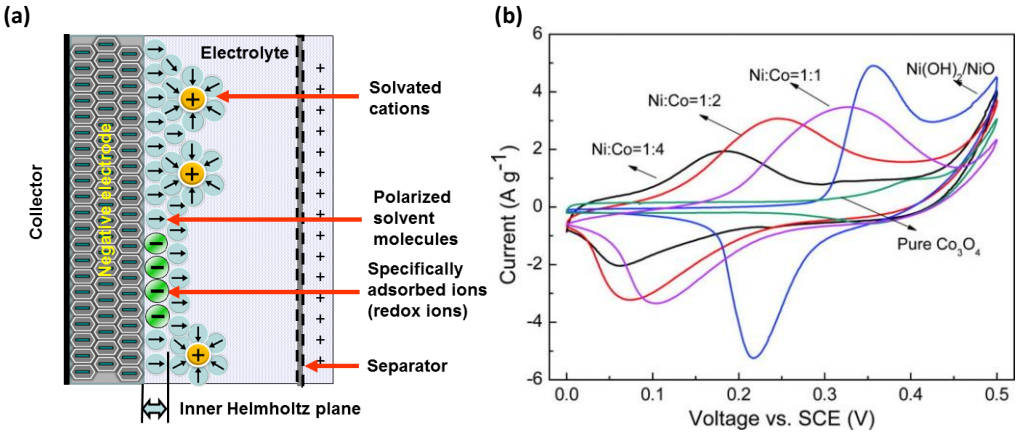

Figure 1.10 (a) Charge storage mechanism in pseudocapacitor electrode material (https://en.wikipedia.org/wiki/Supercapacitor) and **(b)** the cyclic voltammogram for a nickel cobalt oxide based pseudocapacitor material in the three electrode system (http://jes.ecsdl.org/content/162/5/A5185.full.pdf)

Polyaniline and polypyrole are most explored polymers for pseudocapacitor as they have high theoretical capacitance compared to other polymer materials such as PEDOT.[12]

Pseudocapacitors suffer from lower power density as compared to EDLCs due to slow kinetics involved in the faradaic process. Another major drawback of pseudocapacitors is their limited cycle life because of the volume expansion and phase changes that occur upon cycling due to the redox reactions or ion insertion in the bulk of the material. Since only the atoms on and near to the surface take part in the redox reaction, they have lower energy density than batteries. Unlike in EDLCs, the capacitance of a pseudocapacitor is potential dependent as the redox reactions for the materials occur only at particular potentials.

The three different possible mechanisms that can occur at the electrode-electrolyte interface are (i) reversible adsorption of hydrogen on the electrode surface, (ii) oxidation and reduction in the case multivalent transition metal oxides and (iii) doping and de-doping in the case of conducting polymers. The theoretical value of capacitance, C for a pseudocapacitive material can be expressed as

$$C = \frac{n \times F}{M \times V}$$

Where, n is the number electrons transferred during the redox reactions, F is the Faraday's constant, M is the molecular mass of the material and V is the operating potential window.

Although pseudocapacitive materials possess higher capacitance, they have a major drawback of limited potential window (less than 1V) which limits their energy density as the energy density varies linearly with square of the operating potential window. Furthermore they have lower power density than EDLCs because of the lower electrical conductivity of the electrode materials compared to that for EDLC electrodes.

1.2.2.4 Hybrid supercapacitors

1.2.2.4.1 Composite Type

In this class of hybrid systems, composite of the pseudocapacitive material (metal oxides and/or conducting polymers) with conducting carbon forms are used as the electrode materials. Usually carbon forms with high electrical conductivity and high surface area are used as support.[19] This helps to improve the electrical conductivity as well as the accessible surface area of the electrode and hence high power density. The amount of carbon and the active material in the composite can be optimized to get the best performance of the material.

1.2.2.4.2 Hybrid Type

Hybrid capacitor, also called third generation capacitor, is a combination of electrical double layer capacitor and pseudocapacitor material. In a hybrid supercapacitor one electrode is made of EDLC material and the other of pseudocapacitive material and hence the charge storage mechanism involves both surface adsorption and faradaic reaction.[17]

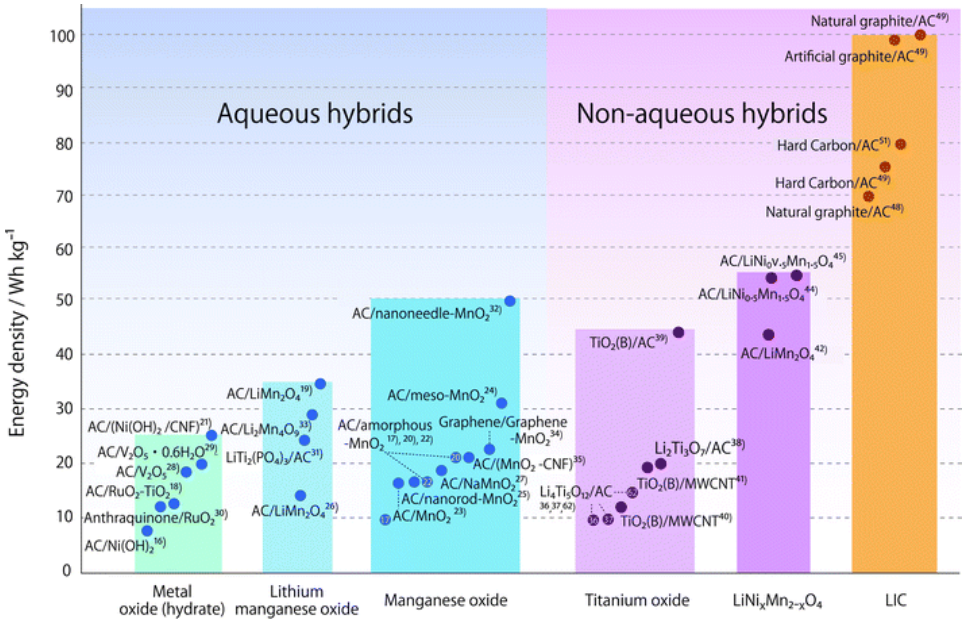

Figure 1.11 Different combinations of anode and cathode material for hybrid supercapacitor for both aqueous and organic electrolytes (Reprinted with permission from *Ref 20*)

Hybrid supercapacitor has energy density higher than EDLCs and power density higher than pure pseudocapacitors. The major advantage of hybrid capacitor is its extended operating potential (>1.2V) even in aqueous based electrolytes. The higher water splitting overpotential for the neutral electrolytes such as Li_2SO_4, Na_2SO_4 and LiCl results in a higher operating potential and hence improved energy density. Figure 1.11 shows the different combinations of electrode material for hybrid supercapacitors.[20]

1.2.2.5 Components of supercapacitors:

Figure 1.12 a and b show the construction of cylindrical and stacked supercapacitors, respectively. The thesis mainly deals with the electrical double layer capacitors and is discussed in detail. An electrical double layer capacitor is comprised of two symmetric electrodes separated by an ionic conducting polymer membrane, called a separator, soaked in electrolyte.

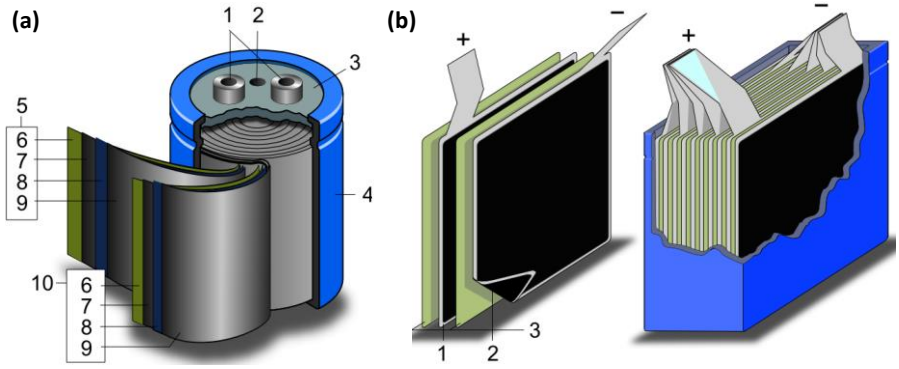

1. Terminals, 2. Safety vent, 3. Sealing disc, 4.Aluminiumcan, 5. Positive electrode, 6. Separator, 7. Carbon coating, 8. Current collector, 9. Carbon electrode, 10. Negative electrode

1. Positive electrode,
2. Negative electrode,
3. Separator

Figure 1.12 Schematic representation of construction of **(a)** Cylindrical (wound) supercapacitors and **(b)** stacked supercapacitor (https://en.wikipedia.org/wiki/Supercapacitor)

The electrode is made of active material coated on a conducting substrate usually in the form of conducting carbon coated aluminium foil. Electrodes are usually made of high surface area conducting carbon with porous structure. Organic salts dissolved in

organic solvents are the commonly used electrolytes for carbon based supercapacitors. Porous polymer membranes such as polypropylene, electrospun PAN fibre and cellulose etc. are used as the separators in supercapacitors.

1.2.2.6 Challenges in Supercapacitors

Despite the high power density and long cyclic stability of supercapacitors, its lower energy density limits its applicability for high energy devices. Hence research on EDLCs mainly focuses on improving the energy density through the development of materials with high specific capacitance. Carbon based materials are commonly used as the electrode materials for electrical double layer capacitors.[21] Figure 1.13 shows different carbon forms that are used for supercapacitor electrodes.[16]

Graphitized carbon with high surface area and porous structure satisfies all the conditions such as electrical conductivity and open porosity that are required for EDLC electrode material.[22]

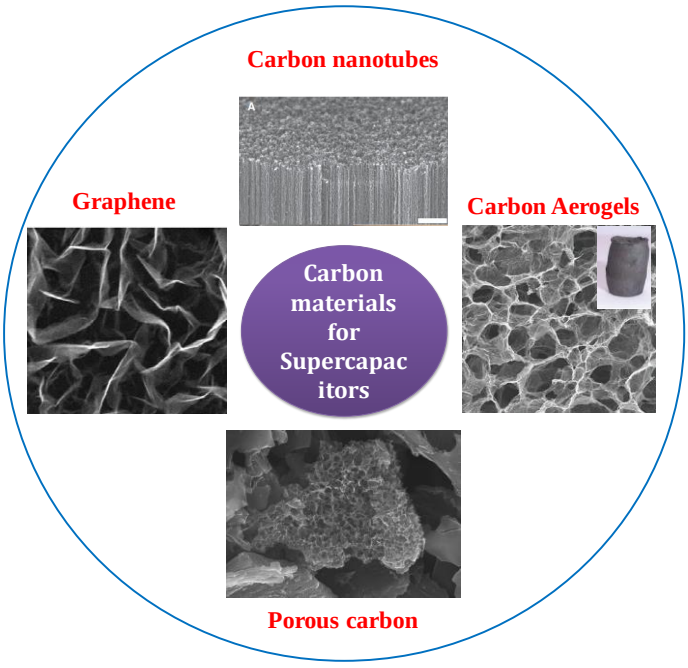

Figure 1.13 Different forms of carbon materials used as electrode materials for supercapacitors (Reprinted with permission)

Different carbon forms such as activated carbon, templated carbon, carbide derived carbon, carbon aerogels, carbon nanotubes, onion like carbon, carbon nanofiber, graphene etc. are well explored as electrode materials for supercapacitors.[23, 24]

Because of its high electrical conductivity and full access to adsorption of ions, onion like carbon has very high power density with limited energy capacity.[25] However lower surface area 1D forms of carbon like carbon nanotubes and carbon nanofiber have high energy density as well as power density since their tubular structure supports fast ion transport and electrical conductivity supports fast electron transport. However, their high manufacturing cost restricts the use in commercial devices. Although carbide derived carbon has high specific capacitance because of high surface area and porosity, the presence of high micropore density and lower electrical conductivity limits its high current performance as well as power capability.[26] Because of the high surface area and electrical conductivity, graphene which is the two dimensional form of carbon, has also been well studied for supercapacitor electrodes.[27] The major disadvantage of graphene is restacking of sheets during electrode preparation and drying. Thus, activated carbons are still widely used because of their high surface area, porous structure and ease of preparation.[28]

1.2.2.7 Charge Storage mechanism in Carbon materials:

Porous carbon materials with high surface area are commonly used electrode materials for EDLCs.[29] The pores are classified into three different categories based on the pore size and are known as micropores (<2 nm), mesopores (2 nm-50 nm) and macropores (>50 nm). Activated carbons have a specific capacitance of 200 Fg^{-1} - 300 Fg^{-1} in the aqueous based electrolytes. The limited operating potentials window of aqueous based electrolytes because of the water oxidation above 1.23V limits the energy density. As an alternative to achieve higher energy density non-aqueous based electrolytes such as organic salts dissolved in organic solvents and ionic liquids have also been explored as the electrolytes as they have an operating potential beyond 3V. This helps increase the energy density as it is directly proportional to square of the operating potential. However the activated carbon typically has a specific capacitance of 100-120 Fg^{-1} in organic electrolytes which is lower than that in the aqueous electrolytes. This is because of the lower conductivity and larger electrolyte ion size. Hence the pore size distribution required for the carbon materials is different for different electrolytes.

1.2.2.8 Dependence of Capacitance on pore size:

Based on the principle of ion transport and adsorption, the capacitance of activated carbons is expected to increase linearly with the surface area and pore volume. It has been observed however that capacitance does not increase further with an increase in the surface area after certain limiting value. After analysing the capacitance of various activated carbons with different porous structure in different electrolytes researchers have reached a conclusion that the specific capacitance does not change linearly with surface area and pore volume but it is also affected by the pore size distribution of the material.[12, 30, 31]

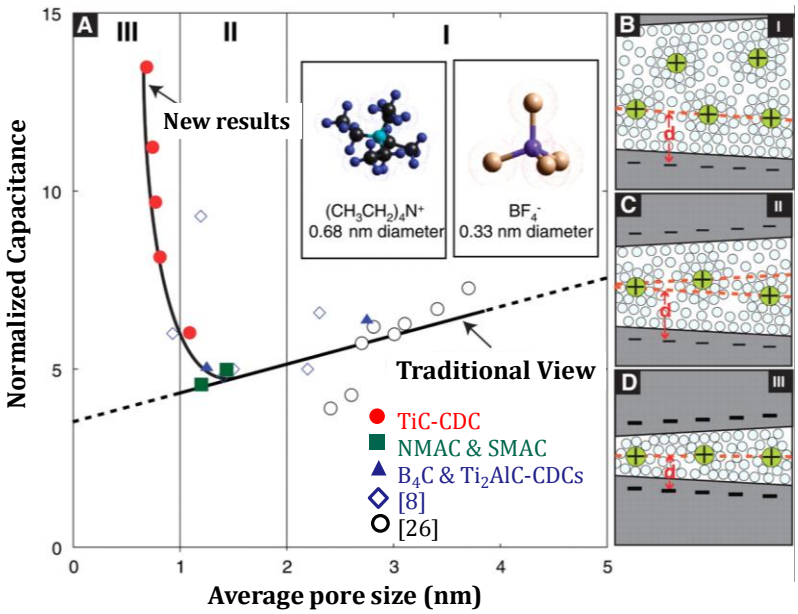

Figure 1.14 (a) Specific capacitance normalized to BET specific surface area as a function of pore size distribution for carbon materials. Huge increase in the normalized capacitance with decreasing pore size below certain value (Zone lll), (B to D) Schematic of solvated ions residing between adjacent walls of pores with distance between the walls **(b)** greater than 2 nm, **(c)** between 1 and 2 nm and **(d)** less than 1 nm (Reprinted with permission from Ref. 26)

Figure 1.14 shows graph plotted with capacitance normalized to surface area against average pore size for various carbon materials. It has been realized that micropores with pore diameter less than 0.5 nm are not accessible to electrolyte ions as the solvated electrolyte ions have ionic radius higher than this in both aqueous and organic electrolytes. Carbon materials with pore size distribution in the range of 2-5

nm are thus identified as a way to improve the energy density and power density of supercapacitors.

Later it has been observed that the capacitance of activated carbon is limited to 100-120 Fg^{-1} for organic electrolytes and 150-300 Fg^{-1} for aqueous electrolyte.[31] This indicates that an optimum micropore to mesopore ratio is necessary to improve the capacitance.[32, 33] However, high capacitance was achieved for carbon materials with high micropore density. In contradiction to solvated ion adsorption theory, specific capacitance of 120 Fg^{-1} and 80 Fcm^{-3} was obtained in organic electrolyte. Raymundo-Pinero et.al have reported that the maximum capacitance was achieved for pore sizes 0.7 nm and 0.8 nm, respectively, in both aqueous and organic electrolytes.[33] Figure 1.15 shows pore size distribution dependence of normalized capacitance for carbide derived carbon in the electrolyte ethyl-methylimidazolium/trifluoro-methane-sulphonylimide (EMI,TFSI).[34]

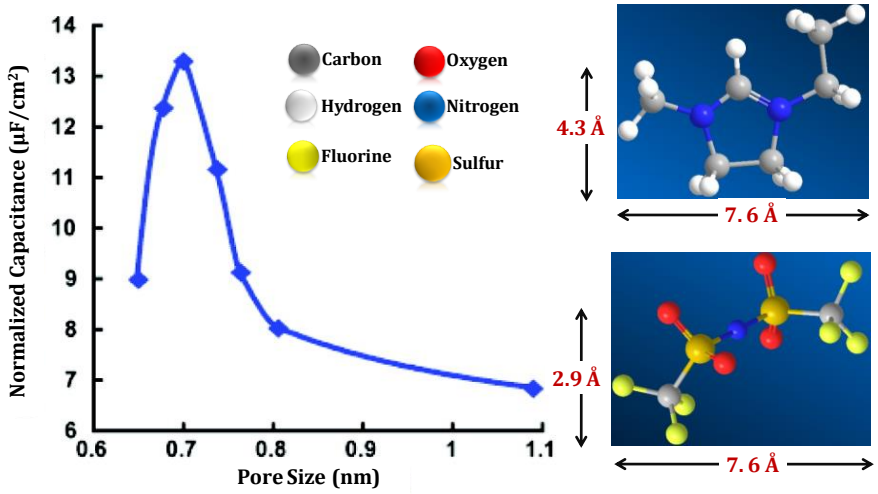

Figure 1.15 Dependence of specific capacitance normalized to surface area as a function of pore size for porous carbon derived metal carbide (Reprinted from Ref. 34 with permission). The measurements were performed with EMI TFSI as the electrolyte. The structures of EMI cation and TFSI anion are given in the inset.

Porous carbon derived from metal carbides has also been employed to study the dependence of pores size on the specific capacitance because the pore size can be fine-tuned in such systems.[35] A narrow uniform pore distributions with pore size in the range 0.6-1.1 nm can be achieved for such materials. The supercapacitor measurements were performed in the electrolyte EMI TFSI. The areal specific

capacitance of the material was observed to decrease with decrease in the pore size down to 1 nm and increased sharply until the pore size reached the size of the electrolyte ion. It has been observed that a maximum capacitance was obtained for the pore size 0.7 nm.[34] This indicates that single ion per pore results in maximum capacitance. Although high density of micropores with pore size equal to size of the electrolyte ions results in maximum capacitance, lack of capacitance retention was observed at higher discharge rates as the fast diffusion of electrolyte ions to the inner micropores are difficult. Therefore the presence of pores with higher dimension is also significant.

Chmiola et al. have reported that the capacitance increases with increase in the pore size until the pore size reaches the size of electrolyte ion and decreases with further increase in the pore size, and the specific capacitance increases when the pore size reaches twice the size of the ion.[30]

Improving the energy density of supercapacitors without compromising its power density and cyclic stability is still a challenge. Wide pore size distribution is essential for obtaining high energy density along with power density as the micropores help for high capacitance and mesopores facilitate the fast ion diffusion in electrodes. The properties of such materials can be further improved through engineering the porous structure. Such carbon materials can also be used as the support for pseudocapacitive materials (oxides) to enhance the electrical conductivity and accessible surface area to improve the high current performance and stability.

Three dimensional networks of carbon materials with wide pore distribution have received much attention as the electrode material as well as active materials support for supercapacitors.[36] 3D carbon structures possess high electrical conductivity and hierarchical porous structure.

Figure 1.16 (a-d) show electron microscopy images of different 3D carbon forms obtained from different carbon precursors such as polymers and biomass.[37, 38] The present thesis is directed to focus on the synthesis of 3D porous carbon and their composite with metal oxide for electrochemical energy storage applications

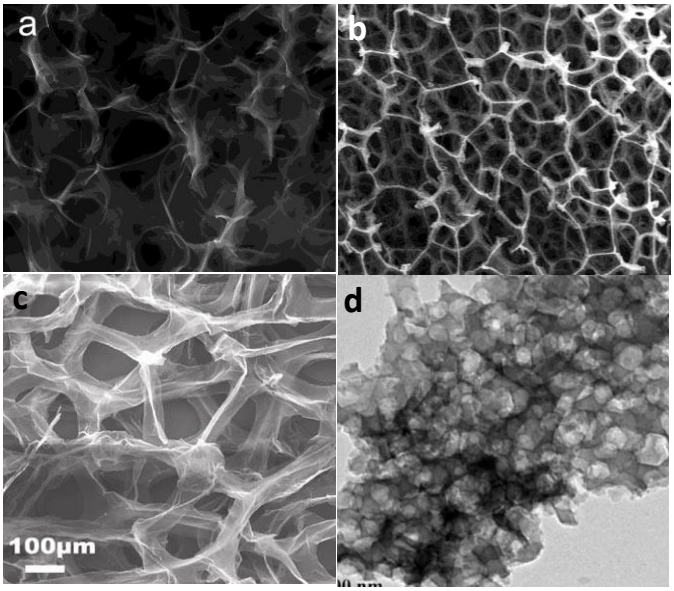

Figure 1.16 (a-d) Electron microscopic images of different 3D porous carbon derived from various carbon precursors. (a and d Reprinted with permission from Ref. 37 and 38, **(b)** http://acsmaterial.com/product.asp?cid=99&id=126)

1.2.2.9 Methods for Porous Carbon Synthesis

1.2.2.9.1 High temperature Pyrolysis

Synthesis of activated carbons from various precursors by different methods is well established. Soft and hard carbons are formed depending upon the precursor used. Carbons that are graphitized below 2000°C are known as soft carbons. Soft polymers and coal tar are the soft carbon precursors. Carbon derived from precursors such as biomass, phenolic resins and carbohydrates undergo graphitization at temperature above 3000°C. Such carbons are called hard carbons. Both hard and soft carbons are partially graphitized with microcrystalline graphitic domains and are also known as turbostratic carbon.

Carbonaceous materials such as biomass, natural products and polymers are the precursors used for the synthesis of porous carbons.[39] Among these, biomass is the most explored precursor because of its rich compositions of carbohydrates, proteins, nucleic acids, fatty acids and many other carbon containing chemical backbones, availability in large scale and low cost. The biomass precursors include natural waste materials such as wood, dead leaves etc. or food wastes which are available in plenty. The two extensively used techniques for the synthesis of carbon materials from

biomass are high temperature (800-1200^{o}C) pyrolysis in inert atmosphere and hydrothermal carbonization.

Pyrolysis is a technique in which the organic molecule is decomposed at elevated temperature through thermo-chemical decomposition in the absence of oxygen. It is also used to convert carbonaceous precursors into activated carbon, charcoal, organic fuels and other chemicals in industrial scale. Pyrolysis starts at temperatures above 200^{o}C and only carbon remains at temperatures above 600^{o}C; hence the process is called as carbonization. Pyrolysis is different from other carbonization techniques such as combustion and hydrolysis as there are no reactions with oxygen or water involved. Depending upon the precursor used, remaining carbon residue may contain functional groups. The carbon obtained after the treatment can be porous or non-porous.

Porosity can be generated in carbon materials either by using templates or by addition of activation agents.[40] Different types of templates called hard templates and soft templates have also been used for synthesis of porous carbons.[41] Organic molecules and polymers are commonly used soft templates. The soft templates simultaneously decompose carbonization because of thermal instability. Hard templates are materials with inherited porosity. Mesoporous silicates are the most commonly used hard templates. This includes zeolites, SBA-15, colloidal silica nanoparticle etc. Porous carbons are obtained by etching out the templates by vigorous treatment in the presence of sodium hydroxide or hydrofluoric acid after carbonization.[42]

Another method to create porosity is through activation in which the carbon precursor reacts with the activation agent during high temperature pyrolysis.[43] The activation agent etches the carbon walls leaving pores in the carbon matrix. The byproducts are removed by suitable chemical treatment. Based on the porogen (activation agent) used activation methods are classified into chemical activation or physical activation. Physical activation is done by passing carbon dioxide or steam along with inert gas during the high temperature pyrolysis. KOH, NaOH, $ZnCl_2$ and H_3PO_4 are used as porogen for chemical activation.[44] The carbon precursor is mixed uniformly with the porogen prior to high temperature pyrolysis. The inorganic byproducts are removed out of the pores by washing with dilute acids followed by water. Use of activation

agent at high temperature introduces surface oxygen functionalities which can reduce the electrical conductivity.

KOH is the most commonly used activation agent for chemical activation. The high temperature treatment of carbon precursor in the presence of KOH results in the formation of –OK functional groups using the oxygen from alkali salt. Such potassium and oxygen bonds result in the oxidation of carbon atoms during activation. The reaction of carbonaceous material with KOH in inert atmosphere leads to porous carbon with potassium and potassium carbonate as the byproduct as per the chemical reaction formula.

$$6KOH + 2C \longrightarrow 2K + 3H_2 + 2K_2CO_3$$ [43]

Apart from biomass, polymers are also well explored as precursors for carbon materials.[38, 45] Polymers offer the advantage of morphology and pore size tunability. With the use of polymers our spectrum of choice increases as the host of natural and synthetic polymers are easily available.

Synthetic polymers such polyacrylonitrile and PVP are used for the synthesis of carbon nanofibers by electrospinning. Nitrogen containing polymers including polyaniline, polypyrole, polyacrylonitrile and polydopamine etc have been employed for the synthesis of nitrogen doped carbon materials. However in all these cases an external activation is required to generate porosity. The main disadvantage of such methods is lack of uniformity in the porosity. Hence alkali metal salts (sodium or potassium salts) of polymers are interesting precursor as the metal present in the monomer unit itself acts as porogen in this case.[38, 46] The amount of the activation agent can be varied by changing the ratio of carbon atoms to alkali element in the monomer unit.

Prasad and co-workers have reported synthesis of high surface area hexaporous graphene using a suitably chosen polymer precursor for supercapacitor applications.[38] These authors used the polymer poly(4-styrenesulfonic acid-co-maleic acid) sodium salt and pyrolyzed it at a high temperature to obtain very high surface area carbon with hexagonal pores. The as-obtained carbon had sheet-like nature. Raman spectroscopy confirmed the single or few layer graphene character of the interesting 3D carbon morphology obtained. The specific surface area of this carbon was 1750

m^2/g. The high surface area was attributed to the presence of carboxylic groups and sodium. During pyrolysis -CO_2 group is detached from carbon backbone and Na_2CO_3 formation takes place. Further washing removes Na_2CO_3 yielding porous carbon. The uniqueness about this approach is the direct formation of a 3D assembly of single or few layer graphene through proper selection of the polymer precursor.

The First chapter of this thesis reports the use polymer salt as the precursor for synthesis of 3D porous carbon for supercapacitor electrode. The potassium salt of the copolymer polyacrylamide co-acrylic acid was used as the carbon precursor. Later researchers have reported alkali salts of oligomers and organic small molecules as carbon precursors.

1.2.2.9.2 Hydrothermal Carbonization

Another method is hydrothermal carbonization in which the carbon precursor is heated at moderate temperature under high pressure in presence of water or diluted acid. Hydrothermal carbonization (HTC) is a powerful technique used for the synthesis of carbon materials from crude biomass.[47]

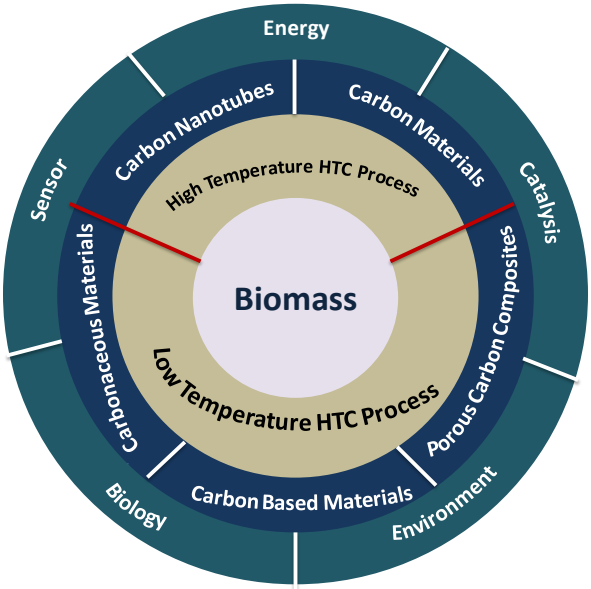

Figure 1.17 schematic representation of different forms of carbon synthesized from biomass by hydrothermal carbonization and its applications in different fields

High temperature hydrothermal carbonization is employed for the synthesis of higher conducting carbon forms such as carbon nanotubes, activated carbons and graphite. The morphology and size of the carbon material can be tuned by hydrothermal

carbonization prior to high temperature treatment. Carbohydrates, waste biomass and organic molecule are the commonly used precursors for synthesis of carbon by hydrothermal carbonization. Figure 1.17 is a schematic representation of different carbon forms derived biomass precursors using hydrothermal carbonization.

Hydrothermal carbonization is usually performed at temperatures in the range of 150-250^{o}C in the presence of dilute acid at high pressure of around 0.1 MPa. The carbonaceous materials undergo variety of changes inside super hot aqueous medium maintained at high pressures. The dehydration, condensation, polymerisation, fragmentation are the dominant reactions of an organic molecules in a hydrothermal process.[47] Dehydration is major contributor for the initiation of the carbonisation process as it removes most of the O, and H atoms from the backbone as water. The high temperature activated carbon backbones. Further high pressure inside an autoclave accelerates the physical and chemical interaction between the reactants and the solvent and allows the polymerization and fragmentation reactions to operate and finally precipitates the carbonaceous precursors. The process is accelerated in presence of acid or base.[47] Based on the temperature, hydrothermal carbonization can be classified as high temperature HTC and low temperature HTC. High temperature carbonization usually performed in the temperature range of 300-800^{o}C. During the process the carbon precursor undergoes dehydration and polymerization. Hydrothermal carbonization has been used for the synthesis of different carbon nanostructures such as carbon nanotube,[48, 49] Three dimensional carbon structures and graphene.[50] Figure 1.18 shows the TEM and SEM images of different forms of carbon synthesized by high temperature hydrothermal carbonization. Low temperature HTC process is used to generate monodispersed carbon spheres from carbohydrates such as cellulose, sugar and glucose etc.[51]

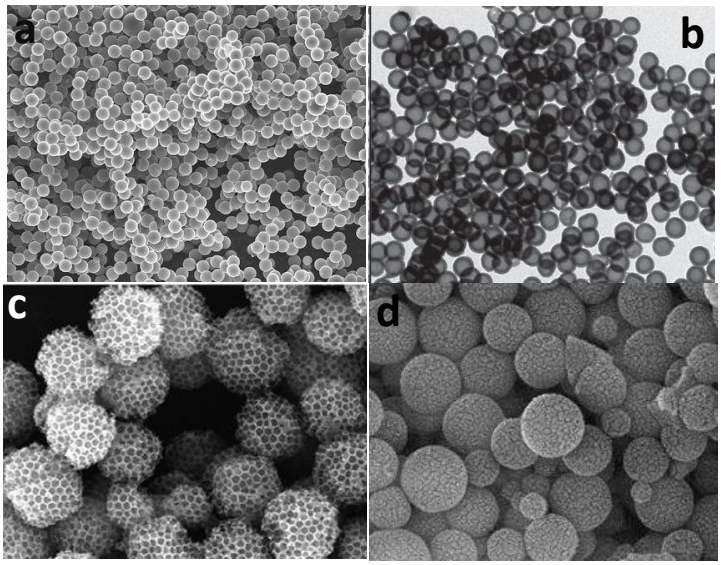

Figure 1.18.Electron microscopy image of the carbon spheres synthesized by hydrothermal carbonization (Reprinted with permission from Ref. 52 and 53) (https://www.flickr.com/photos/argonne/3974987272/in/photostream/, http://imgarcade.com/1/activated-carbon-sem/)

Monodispersed carbon spherules synthesized by low temperature HTC are shown in figure 1.18b.[52] In the low temperature HTC the carbon precursor undergoes dehydration followed by condensation, polymerization and aromatization. The main advantages of HTC over other carbonization techniques are the use of renewable sources as precursors, low toxicity, ease of processing techniques and low energy consumption. Catalysts can be used to accelerate the process. The chemical structure of the intermediate compounds and final product obtained after hydrothermal carbonization is very complicated and has not been reported yet. In the case of biomass containing glucose, sucrose, maltose etc. an intermediate product 5-hydroxymethyl furfural which undergoes polymerization and condensation resulting into final carbon product with large amount of reactive oxygen functional groups and lower electrical conductivity.

The electrical conductivity can be further improved by removing the functional groups by high temperature treatment.[47] The shape and size of the carbon material can be tuned by reaction temperature, concentration and duration. Such materials have already used as electrode materials for supercapacitors, Li-ion batteries and Na-ion batteries. The carbonaceous material obtained directly after low temperature HTC

possesses low surface area (<100 m^2g^{-1}) and micropore density. Post carbonization can improve the surface area up to 400 m^2g^{-1}.

The porosity can be introduced either by incorporating hard templates such as colloidal silica nanoparticles or mesoporous silica during the hydrothermal reaction followed by a high temperature treatment.[53] The templates are removed by treating the product with HF, NaOH or KOH after the heat treatment. Activation techniques such as physical activation and chemical activation can also be employed during the high temperature treatment to get porosity as in the case of pyrolysis.

Hydrothermal carbonization is a powerful technique for synthesis of porous carbon from carbonaceous precursors. In this thesis, low temperature hydrothermal carbonization followed by high temperature treatment in the presence of activation agent is performed to obtain three dimensional porous carbonas electrode material EDLCs by using white paper which is a cellulose-rich precursor.

1.2.3 Li-ion battery

Lithium-ion (Li-ion) batteries are projected to become the most popular battery technology for hybrid and electric vehicles, and mobile electronics applications as they possess high charge storage capacity and energy density.[8, 54] Although Li-ion battery technology is found in nearly all consumer electronics, additional technological advances are necessary to improve its performance further. The major challenges are to improve the durability and safety along with cost reduction without hampering the energy density.[54] The current cost of lithium-ion batteries for vehicle applications is four to eight times that of lead acid batteries and one to four times that of nickel metal hydride batteries.

Li-ion battery construction constitutes four major components, namely the cathode, the anode, the electrolyte and the separator.[8] Li-ion batteries store electricity by means of electrochemical reaction at the cathode and anode through movement of Li^+ ions between them through the electrolyte. The cathode and anode materials undergo conversion during the charging and discharging cycles. Cathode materials are lithium metal oxides which give Li-ion during charging and receive Li during discharging and vice versa for the anode materials.

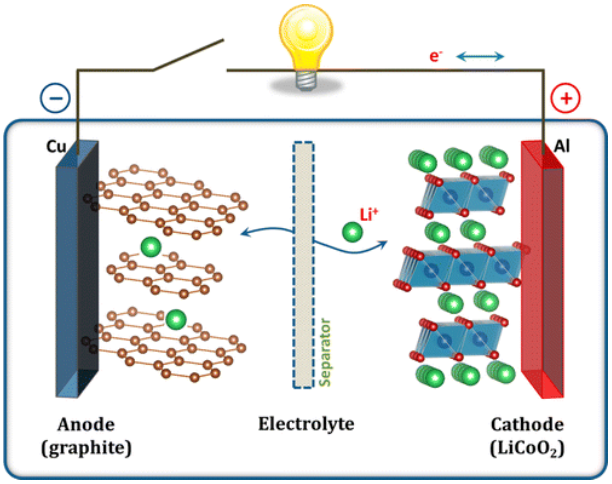

Figure 1.19 Schematic of Li-ion battery with graphitic carbon as anode material and lithium metal oxide as cathode. (Reprinted with permission from Ref. 55)

Role of the electrolyte is to pass Li-ions between cathode and anode during charge discharge cycles and lithium salts in organic solvents are commonly used as electrolytes. Porous polymer membrane used as separator prevents short circuit between cathode and anode, and allows passing Li-ions between cathode and anode.[55]

A schematic showing the device construction and charge discharge mechanism is given in figure 1.19.[55] During charging positive potential is applied to cathode and negative potential to anode and the Li ions move from the cathode to anode through the electrolyte. During discharging Li ions move back to the cathode material releasing electrons from anode to cathode through external circuit which results into the electricity. Current Li-ion battery technology uses graphite powder as the anode material and lithium cobalt oxide as cathode material.[55] During charging Li-ions move from $LiCo_2O_4$ to graphite and get intercalated in the layers of graphite forming LiC_6 and during the discharging cycle the Li^+ ions move back to cathode.

The reaction involved in the charge-discharge cycle can be expressed as

$$\text{At Cathode}$$

$$LiCoO_2 \rightleftharpoons Li_{1-x}CoO_2 + xLi^+ + xe^-$$

$$\text{At Anode}$$

$$6C + xLi^+ + xe^- \rightleftharpoons Li_xC_6$$

$$LiCoO_2 + 6C \underset{\text{Net reaction}}{\rightleftharpoons} Li_{1-x}CoO_2 + Li_xC_6$$

Current Li-ion battery technology is not sufficient to satisfy the requirement of electric vehicles (EV) or plug-in hybrid electric vehicle (PHEV) in terms of energy density and power density. Development of Li-ion battery for electric vehicles at lower cost with durability is still a challenge. Thus the cost, safety, cycle life, energy, and power are some of the major issues for successfully adopting the lithium ion technology for transportation. These parameters can be controlled by tuning the properties of the component materials. The energy and power density of the device can be improved by manipulating the cathode and anode materials design.

Other than $LiCoO_2$ the suitable candidates for Li-ion battery cathode are $LiNiO_2$ (Lithium Nickelate), $LiMn_2O_4$ (Lithium Manganate) and polyanions such as $Li_3V_2(PO4)_3$, $LiFePO_4$, $LiFeSO_4$ etc. because of their high capacity, operating potential and stability. Still intense research is being conducted on cathode materials for improving the energy density further and understanding the reason for capacity degradation upon cycling.[56]

Apart from cathode materials, tremendous research efforts are going on anode materials as well for improving the specific capacity of Li-ion battery as the current anode material, namely graphite, which is used in commercial Li-ion batteries, has limited theoretical capacity of 372 $mAhg^{-1}$.[57]

The theoretical capacity of a Li-ion battery electrode (anode or cathode) can be expressed as

$$C(mAhg^{-1}) = \frac{n \times F}{Molar\ Mass \times 3.6}$$

Where ‘n’ is the number of Li-ions stored per molecule and F is the Faraday’s constant (96400 C). Transition metal oxides are promising candidates as one oxygen atom in the oxide can be replaced by two Li^+ ions. There are three types of storage mechanisms in anode materials which are called insertion, conversion and alloying. Figure 1.20 represents the schematic for different types of lithium ion battery

electrode materials and their classification according to charge storage mechanism.[58] Insertion type materials include Nb_2O_5, TiO_2 and $Li_4Ti_5O_{12}$ in which the Li+ ions intercalate into the anode material during charging. No major structural changes occur in such materials during the Li intercalation de-intercalation process and hence are highly stable upon cycling.

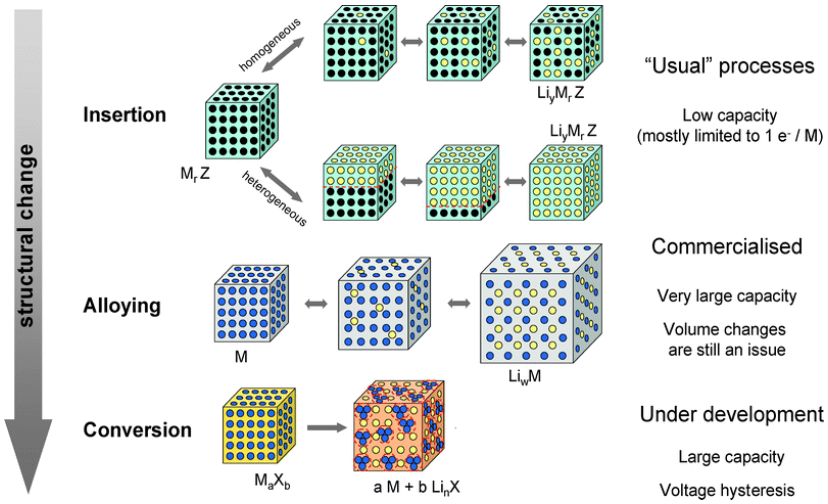

Figure 1.20 Schematic representation of classification of electrode materials for Li-ion battery based on the storage mechanism involved in it. The black, blue and yellow circles represent the void in the crystal structure, metal and lithium respectively. (Reprinted with permission from Ref 58)

Alloying type materials, representing another class of anode materials, have higher theoretical capacity. Lithium ions make alloys with the electrode material during the electrochemical reaction. Silicon, antimony, aluminium and tin are the alloying type anode material explored for Li-ion battery.[59] Silicon has a theoretical charge storage capacity of 4200 $mAhg^{-1}$. The reaction of Lithium with Si forms an alloy $Li_{4.4}Si$ which indicates an increase of 440% in the number of atoms per active particle. As a result there will be huge volume expansion in the electrode material upon charge discharge process which leads to loss of contact between the electrode material and the current collector as well as disintegration of the electrodes. This results into fast decrease in the capacity of the material upon cycling and hence poor cyclic stability. Researchers are still working on improving the stability of such materials by making composites with carbon materials, yolk-shell structure with carbon coating and making alloys with transition metals.[59] Another class of anode materials are conversion type materials. Conversion reaction is usually defined as reaction of

transition metal compounds M_aX_b (M= transition metal and X= O, S, F, P, N etc.) with lithium ions to form metallic nanoparticles. During the reaction the transition metal oxide in the oxidized state is reduced to metallic state resulting in a high theoretical capacity.[60] In a conversion type material the electrode material undergoes changes in oxidation state during the Li^+ ion insertion. Such materials possess a higher theoretical capacity than intercalation type electrodes.[61] Research on the materials resulting from conversion reaction during charge discharge cycles has also been accelerated recently. The conversion reaction of transition metals mostly happens in the potential range of 0.3-1V vs. Lithium. However the large voltage hysteresis between the charging and discharging is the major drawback of these materials.

Among various conversion type materials Cobalt oxide (Co_3O_4) has attracted extensive interest because of its high theoretical capacity of 890 $mAhg^{-1}$ which is more than double that of graphite (372 $mAhg^{-1}$); the present commercial Li-ion battery anode.[62] Some disadvantages of such materials are poor performance at higher discharge rates and capacity fading upon cycling due to volume expansion in the charge discharge cycles. These issues restrict the practical implementation of such materials for commercial applications.

Nanomaterials are identified as the ideal for conversion type electrode material because of their increased surface area and short diffusion length. This can improve the power density as it facilitates the electrochemical reaction because of the improved mass transport and charge transfer.[63] However, they undergo huge volume expansion or contraction during lithium intercalation and de-intercalation process which eventually leads to loss of inter-particle contact because of electrode pulverization. As a result a large decrease in the irreversible capacity upon cycling is observed. Different strategies have been explored to avoid these issues. This includes making nanostructure and carbon composite of active material. However maintaining high reversible capacity at high current discharge rates along with long cyclic stability still remains a challenge in this field. Different carbon nanostructures have been explored as conductive support for the Co_3O_4 for lithium ion battery electrode.[63] This includes graphene, carbon nanotube, carbon nanofiber etc. Among these graphene, the two dimensional form of carbon which has very high surface area compared to other nanoforms is considered to be promising material because the graphene layers

act as a support for uniform dispersion of nanoparticle besides acting as a conductive matrix for facilitating electron transport in the material to improve the power capability.[63, 64] The high surface area support also prevents the volume expansion and aggregation of nanoparticles during the charge discharge process. However the grapheme sheets undergo restacking after removing the solvent. This can be avoided by making a 3D porous network of graphene sheets. The 3D network of graphene can effectively reduce the restacking of graphene layers maintaining a high accessible surface area. Recent works have reported that rate performance and cyclic stability are improved for 3D graphene based composites as compared to the pristine material.[65]

The third chapter of this thesis deals with the use of high surface area 3D porous graphene as a support for the active material (Co_3O_4) and study of its performance as anode material for Li-ion battery.

1.2.4 Li-ion hybrid electrochemical capacitor (Li-HEC)

Single energy storage device concept such as a supercapacitor or a battery is not yet capable of satisfying all the needs of future applications such as mobile electronic devices and electric/hybrid vehicles due to their limitation in delivering high energy and power densities simultaneously. Therefore current research is focussing on developing energy storage devices with high energy density without compromising its power density and stability. Hybrid supercapacitors possess high energy density and broad potential window as compared with the symmetric supercapacitor and higher power density compared with Li-ion batteries.[66] The energy density (E) of an energy storage device is directly proportional to the capacity (Q) and operating potential (V). Monodispersed carbon spherules synthesized by low temperature HTC a**r**e shown in figure 1.18b.[52] In the low temperature HTC the carbon precursor undergoes dehydration followed by condensation, polymerization and aromatization. The main advantages of HTC over other carbonization techniques are the use of renewable sources as precursors, low toxicity, ease of processing techniques and low energy consumption. Catalysts can be used to accelerate the process. The chemical structure of the intermediate compounds and final product obtained after hydrothermal carbonization is very complicated and has not been reported yet. In the case of biomass containing glucose, sucrose, maltose etc. an intermediate product 5-

hydroxymethyl furfural which undergoes polymerization and condensation resulting into final carbon product with large amount of reactive oxygen functional groups and lower electrical conductivity.

The energy density can be increased either by increasing the capacitance or cell voltage or both. This can be made by use of asymmetric combinations of different cathodes and anodes, producing a higher working voltage and specific capacitance. An example is the combination of an EDLC electrode with a battery-like one. In such systems, termed as "asymmetric hybrid capacitors or Li-ion hybrid electrochemical capacitor (Li-HEC)", the battery-like electrode provides high capacity and energy density while the EDLC electrode enables high power capability through the fast adsorption and desorption of electrolyte ions in the system.[67] By designing electrolytes for optimum performance in such asymmetric configurations, the critical need for high-voltage operation may be achieved without compromising stability or long-term cycleability.

Figure 1.21 shows the Ragone plot that compares the energy density and power density of different types of supercapacitors.[68] It shows that the hybrid supercapacitors and organic asymmetric capacitor have energy density one order higher than that for carbon based supercapacitors without compromising its power density.

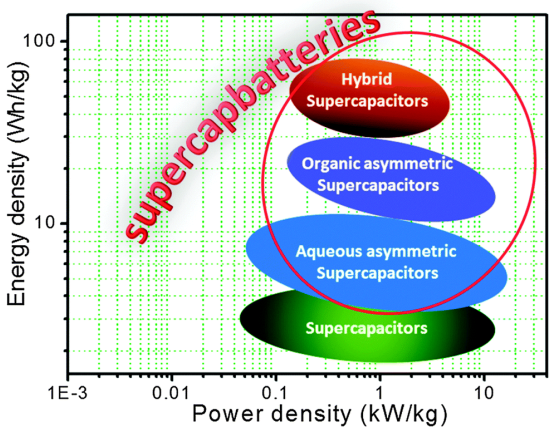

Figure 1.21 Ragone plot comparing the energy density and power density of different types of supercapacitors (Reprinted with permission from Ref. 68)

Li-ion hybrid electrochemical capacitor (Li-HEC) also known as non-aqueous hybrid supercapacitor is another class of asymmetric capacitor. This utilizes both the storage

mechanisms of battery as well as supercapacitor for energy storage. The energy storage is through intercalation of Li^+ ions on the negative electrode (anode) and surface adsorption of negative ions on the positive electrode (cathode). The advantage of Li-HEC over aqueous asymmetric supercapacitor is its higher operating potential and hence higher energy density. Li-HEC has energy density and power density between that of supercapacitors and Li-ion battery. Low power density of Li ion battery and low energy density of supercapacitor makes Li ion capacitor very important for next generation energy storage devices. The storage capacity of Li-HEC is mainly affected by the Li storage capacity of the anode material and double layer storage capacity of the cathode material. High surface area porous carbon is used as cathode and Li intercalation material is used as anode.

Li ion capacitor uses both the faradic reaction as well as the non-faradic adsorption for charge storage. High surface area porous carbons, graphene, CNT etc have been tried for double layer adsorption of ions whereas insertion materials such as $Li_4Ti_5O_{12}$, graphite, TiO_2, V_2O_5 etc. are used as the intercalation electrode.

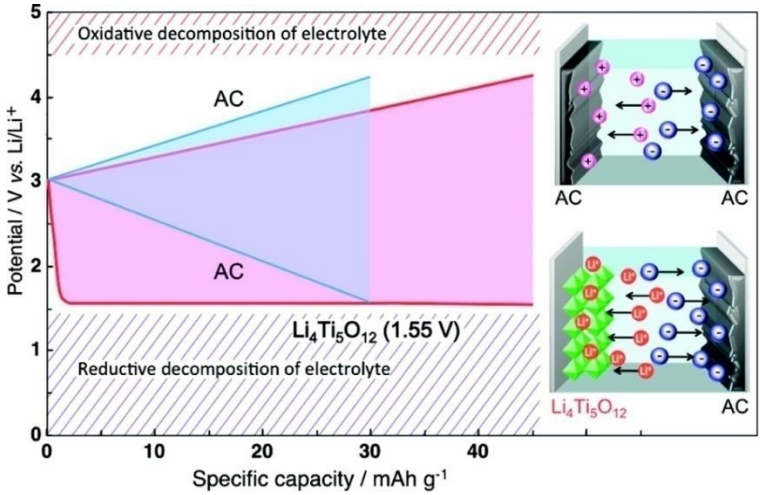

Figure 1.22 Schematic comparing the configuration and working potential range for a symmetric supercapacitor with those for Li-ion hybrid supercapacitor (Reprinted with permission from Ref. 67)

A comparison of charge storage mechanism, capacity and operating potential range for Li-ion hybrid capacitor with double layer capacitor is given in the figure 1.22 schematically.[67] The operating potential of the Li ion capacitor depends on the insertion potential of Li faradaically into the electrode materials. Proper utilization of

the combination of insertion-type electrodes with supercapacitor carbon electrode certainly leads to the substantial increase in the net operating potential as well as the energy density. In the thesis, three dimensional porous carbons with high surface area obtained from the polymer precursor pyrolysis were tested as cathode materials for Li-HEC as well.

1.4 Scope and Objective of the thesis

The above brief review on the current status of energy storage technologies indicate that concerted effort is required for making it efficient enough to use in future applications including mobile electronics and electric vehicles. In context of the above mentioned background, the present thesis compiles development of electrode material for advanced energy storage systems. 3D porous carbon materials and their nanocomposites were developed as electrode for electrochemical energy storage devices such as supercapacitors and Li-ion batteries. High temperature pyrolysis and hydrothermal carbonization, large scale processes were employed to develop 3D forms of porous carbon from polymeric precursor. 3D porous graphene obtained from polymer salt pyrolysis was used as active material support for Li-ion battery anode.

Carbon material with interconnected hierarchical structure was synthesized by direct pyrolysis of poly(acrylamide-co-acrylic acid) potassium salt in inert atmosphere without any external activation agent. The presence of the alkali metal in the selected polymer precursor results in a high specific surface area of 1327 m^2g^{-1}. The presence of three different types of pores makes the material ideal for supercapacitor electrodes. The IMPC was tested as an electrode in aqueous and non-aqueous supercapacitors. The material showed better performance as cathode material for Lithium-ion hybrid capacitor in comparison with commercial supercapacitor carbon.

Hydrothermal processing followed by controlled pyrolysis of waste (used) white office paper (a globally collectable shredded paper waste) was performed to obtain high surface area carbon with hierarchical pore size distribution. Such waste paper derived carbon (WPC) shows remarkable performance in all solid-state supercapacitor fabricated with ionic liquid-polymer gel electrolyte. The Li-ion electrochemical capacitor constructed using WPC as cathode also shows an excellent energy storage capacity of 61 $Whkg^{-1}$.

Co_3O_4/porous graphene(PG) nanocomposite synthesized by a simple solvothermal route and its application as Li-ion battery anode. The ratio of graphene to Co_3O_4 is optimized to get its best possible performance. Among the different compositions investigated, the composite PG-600 (with 50% PG) shows a discharge capacity of 700 mAh g^{-1} at a current density of 500 mA g^{-1} and maintains 90% retention after 80 cycles. The increased surface area and electrical conductivity of the composite result into an enhancement in the capacity, cycling stability and rate capability as compared to native Co_3O_4 phase.

1.5 References

1. P. Nejat, F. Jomehzadeh, M. M. Taheri, M. Gohari and M. Z. Abd. Majid, *Renewable and Sustainable Energy Reviews*, 2015, **43**, 843-862.
2. L. Shi and M. Y. L. Chew, *Renewable and Sustainable Energy Reviews*, 2012, **16**, 192-207.
3. X. Chen, C. Li, M. Gratzel, R. Kostecki and S. S. Mao, *Chem. Soc. Rev.*, 2012, **41**, 7909-7937.
4. B. O'Regan and M. Gratzel, *Nature*, 1991, **353**, 737-740.
5. W. A. Badawy, *Journal of Advanced Research*, 2015, **6**, 123-132.
6. G. M. Joselin Herbert, S. Iniyan, E. Sreevalsan and S. Rajapandian, *Renewable and Sustainable Energy Reviews*, 2007, **11**, 1117-1145.
7. C. P. Kuang, H. C. Huang, Y. Pan and J. Gu, *Adv Mater Res-Switz*, 2012, **512-515**, 900-904.
8. B. Dunn, H. Kamath and J.-M. Tarascon, *Science*, 2011, **334**, 928-935.
9. P. J. Hall and E. J. Bain, *Energy Policy*, 2008, **36**, 4352-4355.
10. M. Winter and R. J. Brodd, *Chem. Rev.*, 2004, **104**, 4245-4270.
11. R. F. Service, *Science*, 2006, **313**, 902.
12. P. Simon and Y. Gogotsi, *Nature Mater.*, 2008, **7**, 845-854.
13. J. R. Miller and P. Simon, *Science*, 2008, **321**, 651-652.
14. S. Roldan, D. Barreda, M. Granda, R. Menendez, R. Santamaria and C. Blanco, *Phys. Chem. Chem. Phys.*, 2015, **17**, 1084-1092.
15. A. Ghosh and Y. H. Lee, *Chemsuschem*, 2012, **5**, 480-499.
16. L. L. Zhang and X. S. Zhao, *Chem. Soc. Rev.*, 2009, **38**, 2520-2531.
17. J. Zhang and X. S. Zhao, *Chemsuschem*, 2012, **5**, 818-841.

18. Q. Lu, J. G. Chen and J. Q. Xiao, *Angew. Chem. Int. Ed.*, 2013, **52**, 1882-1889.
19. S. Bose, T. Kuila, A. K. Mishra, R. Rajasekar, N. H. Kim and J. H. Lee, *J. Mater. Chem.*, 2012, **22**, 767-784.
20. K. Naoi, S. Ishimoto, J.-i. Miyamoto and W. Naoi, *Energy Environ. Sci.*, 2012, **5**, 9363-9373.
21. A. Davies and A. Yu, *The Canadian Journal of Chemical Engineering*, 2011, **89**, 1342-1357.
22. L. Weinstein and R. Dash, *Mater. Today*, 2013, **16**, 356-357.
23. M. D. Stoller, S. Park, Y. Zhu, J. An and R. S. Ruoff, *Nano Lett.*, 2008, **8**, 3498-3502.
24. Y. Zhai, Y. Dou, D. Zhao, P. F. Fulvio, R. T. Mayes and S. Dai, *Adv. Mater.*, 2011, **23**, 4828-4850.
25. D. Pech, M. Brunet, H. Durou, P. Huang, V. Mochalin, Y. Gogotsi, P.-L. Taberna and P. Simon, *Nat Nano*, 2010, **5**, 651-654.
26. J. Chmiola, C. Largeot, P.-L. Taberna, P. Simon and Y. Gogotsi, *Science*, 2010, **328**, 480-483.
27. C. Liu, Z. Yu, D. Neff, A. Zhamu and B. Z. Jang, *Nano Lett.*, 2010, **10**, 4863-4868.
28. Y. Zhu, S. Murali, M. D. Stoller, K. J. Ganesh, W. Cai, P. J. Ferreira, A. Pirkle, R. M. Wallace, K. A. Cychosz, M. Thommes, D. Su, E. A. Stach and R. S. Ruoff, *Science*, 2011, **332**, 1537-1541.
29. L. Borchardt, M. Oschatz and S. Kaskel, *Materials Horizons*, 2014, **1**, 157-168.
30. J. Chmiola, G. Yushin, Y. Gogotsi, C. Portet, P. Simon and P. L. Taberna, *Science*, 2006, **313**, 1760-1763.
31. H. Shi, *Electrochim. Acta*, 1996, **41**, 1633-1639.
32. A. B. Fuertes, G. Lota, T. A. Centeno and E. Frackowiak, *Electrochim. Acta*, 2005, **50**, 2799-2805.
33. E. Raymundo-Piñero, K. Kierzek, J. Machnikowski and F. Béguin, *Carbon*, 2006, **44**, 2498-2507.
34. C. Largeot, C. Portet, J. Chmiola, P.-L. Taberna, Y. Gogotsi and P. Simon, *J. Am. Chem. Soc.*, 2008, **130**, 2730-2731.

35. A. Jänes, L. Permann, M. Arulepp and E. Lust, *Electrochem. Commun.*, 2004, **6**, 313-318.
36. H. Jiang, P. S. Lee and C. Li, *Energy Environ. Sci.*, 2013, **6**, 41-53.
37. H. Wang, Z. W. Xu, A. Kohandehghan, Z. Li, K. Cui, X. H. Tan, T. J. Stephenson, C. K. King'ondu, C. M. B. Holt, B. C. Olsen, J. K. Tak, D. Harfield, A. O. Anyia and D. Mitlin, *ACS Nano*, 2013, **7**, 5131-5141.
38. P. Yadav, A. Banerjee, S. Unni, J. Jog, S. Kurungot and S. Ogale, *Chemsuschem*, 2012, **5**, 2159-2164.
39. A. M. Abioye and F. N. Ani, *Renewable and Sustainable Energy Reviews*, 2015, **52**, 1282-1293.
40. J. Lee, J. Kim and T. Hyeon, *Adv. Mater.*, 2006, **18**, 2073-2094.
41. B. Sakintuna and Y. Yürüm, *Industrial & Engineering Chemistry Research*, 2005, **44**, 2893-2902.
42. J. Lee, S. Han and T. Hyeon, *J. Mater. Chem.*, 2004, **14**, 478-486.
43. J. Wang and S. Kaskel, *J. Mater. Chem.*, 2012, **22**, 23710-23725.
44. M. Molina-Sabio and F. Rodríguez-Reinoso, *Colloids and Surfaces A: Physicochemical and Engineering Aspects*, 2004, **241**, 15-25.
45. L. Wei, M. Sevilla, A. B. Fuertes, R. Mokaya and G. Yushin, *Adv. Funct. Mater.*, 2012, **22**, 827-834.
46. D. Hines, A. Bagreev and T. J. Bandosz, *Langmuir*, 2004, **20**, 3388-3397.
47. B. Hu, K. Wang, L. H. Wu, S. H. Yu, M. Antonietti and M. M. Titirici, *Adv. Mater.*, 2010, **22**, 813-828.
48. D. C. Lee, F. V. Mikulec and B. A. Korgel, *J. Am. Chem. Soc.*, 2004, **126**, 4951-4957.
49. P. Dubey, D. Muthukumaran, S. Dash, R. Mukhopadhyay and S. Sarkar, *Pramana - J. Phys.*, 2005, **65**, 681-697.
50. Y. G. Gogotsi and M. Yoshimura, *Nature*, 1994, **367**, 628-630.
51. M. Zheng, Y. Liu, Y. Xiao, Y. Zhu, Q. Guan, D. Yuan and J. Zhang, *J.Phys.Chem.C*, 2009, **113**, 8455-8459.
52. J. Sun, J. Zhang, M. Zhang, M. Antonietti, X. Fu and X. Wang, *Nat Commun*, 2012, 1139.
53. Y. Kim, C.-Y. Cho, J.-H. Kang, Y.-S. Cho and J. H. Moon, *Langmuir*, 2012, **28**, 10543-10550.
54. J. M. Tarascon and M. Armand, *Nature*, 2001, **414**, 359-367.

55. J. B. Goodenough and K.-S. Park, *J. Am. Chem. Soc.*, 2013, **135**, 1167-1176.
56. J. W. Fergus, *J. Power Sources*, 2010, **195**, 939-954.
57. P. Poizot, S. Laruelle, S. Grugeon, L. Dupont and J. M. Tarascon, *J. Power Sources*, 2001, **97–98**, 235-239.
58. M. R. Palacin, *Chem. Soc. Rev.*, 2009, **38**, 2565-2575.
59. C.-M. Park, J.-H. Kim, H. Kim and H.-J. Sohn, *Chem. Soc. Rev.*, 2010, **39**, 3115-3141.
60. M. V. Reddy, G. V. Subba Rao and B. V. R. Chowdari, *Chem. Rev.*, 2013, **113**, 5364-5457.
61. P. Poizot, S. Laruelle, S. Grugeon, L. Dupont and J. M. Tarascon, *Nature*, 2000, **407**, 496-499.
62. S. A. Needham, G. X. Wang, K. Konstantinov, Y. Tournayre, Z. Lao and H. K. Liu, *Electrochem Solid St*, 2006, **9**, A315-A319.
63. D. S. Su and R. Schlogl, *Chemsuschem*, 2010, **3**, 136-168.
64. S. Choi, J.-K. Lee and Y. Kang, *Nano Res*, 2015, **8**, 1584-1594.
65. B. G. Choi, S.-J. Chang, Y. B. Lee, J. S. Bae, H. J. Kim and Y. S. Huh, *Nanoscale*, 2012, **4**, 5924-5930.
66. K. Naoi, S. Ishimoto, J. Miyamoto and W. Naoi, *Energy Environ. Sci.*, 2012, **5**, 9363-9373.
67. K. Naoi, W. Naoi, S. Aoyagi, J. Miyamoto and T. Kamino, *Acc. Chem. Res.*, 2013, **46**, 1075-1083.
68. D. P. Dubal, O. Ayyad, V. Ruiz and P. Gomez-Romero, *Chem. Soc. Rev.*, 2015, **44**, 1777-1790.

Chapter 2

Synthesis and Characterization Techniques

This chapter briefly describes the experimental procedures, characterization techniques and measurement systems used for the research that is presented in the thesis.

2.1 Synthesis Methods

2.1.1 High temperature Pyrolysis

Pyrolysis is a technique used to synthesize carbon material in which the carbon precursor is heated at elevated temperature in the inert atmosphere using a split tube furnace shown in figure 2.1. This process is extensively used for large scale production of charcoal, activated carbon and other chemicals.[1, 2] It is also used for the synthesis different forms of carbon such as graphene, carbon nanotubes, carbon nanofiber etc. from biomass and various polymers etc.[3-5]

Figure 2.1 Image of a split tube furnace used for synthesis of carbon by high temperature pyrolysis

High surface area porous carbons (activated carbon) are prepared by pyrolysis of carbonaceous materials such as biomass or polymers either by addition of external activation agents or using templates.[6-8] Activation techniques are classified in to two known as physical activation and chemical activation based on the activation agents.

2.1.2 Hydrothermal Carbonization

Hydrothermal Carbonization is another technique widely used for synthesis of carbon material from biomass at moderate conditions.[9, 10] This is done by keeping the biomass suspension in water at elevated temperature and high pressure. This involves a combined dehydration and decarboxylation of biomass which results into high carbon content.[11] The hydrothermal carbonization is performed in lab scale using teflon lined steel autoclave as shown in figure 2.2.

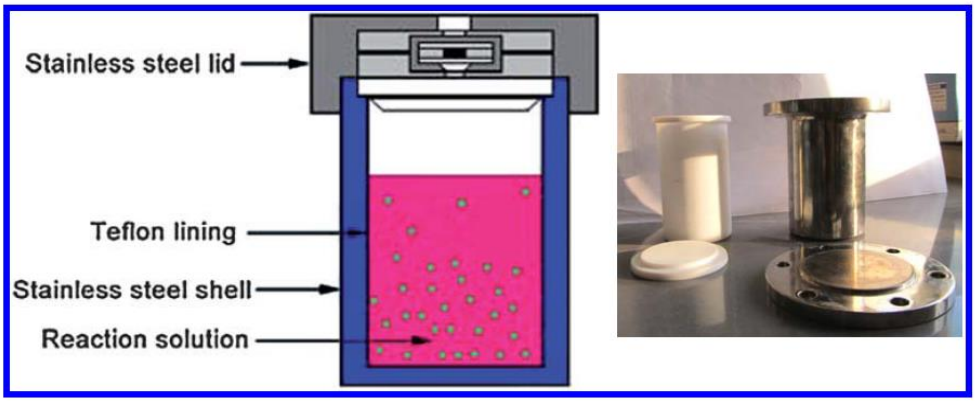

Figure 2.2 Schematic of Teflon lined stainless steel autoclave for high pressure hydrothermal reaction. (Reprinted with permission from Energy Environ. Sci., 2011, 4, 818-841)

2.2 Characterization technique

2.2.1 Powder X-Ray diffraction

Powder X-ray diffraction is a widely used non-destructive technique used to get information about the crystalline structure of the material.[12] This is widely used preliminary technique to identify the structure of the material. In addition to crystal structure, X-ray diffraction also provides information about lattice parameter, average crystallite size etc.[13] Figure 2.3 shows the schematic of a powder X-ray diffractometer.

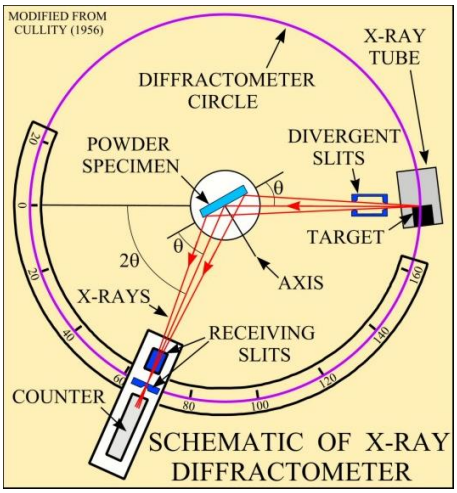

Figure 2.3 schematic of X-ray diffractometer and working principle (http://pubs.usgs.gov/of/2001/of01-041/htmldocs/xrpd.htm)

X-ray diffractometer works on the basis of Bragg's diffraction law.[14, 15] According to Bragg's law monochromatic X-rays undergo scattering from a crystalline solid. The scattered beams interfere constructively or destructively to produce diffraction pattern. The scattered waves undergo constructive interference when the path difference between them is an integral multiple of nλ, where λ is the wavelength of the incident X-ray beam. The path difference between the waves scattered at an angle 'θ' from crystal from two planes with inter-planar distance 'd' is 2d sinθ (from figure 2.4).

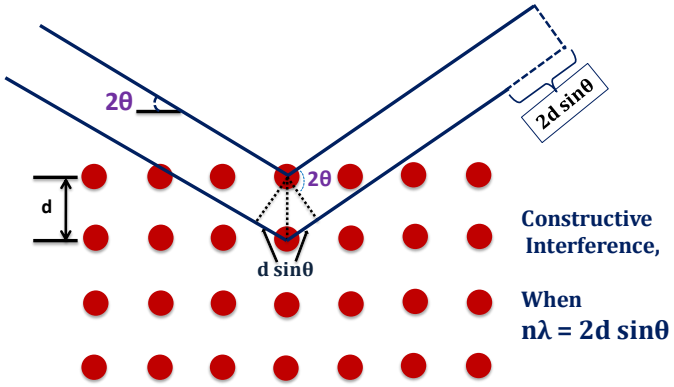

Figure 2.4 Schematic of Principle of X-ray diffraction

The condition for constructive interference leads to Bragg equation 2d sinθ = nλ, where n is an integer.

During X-ray diffraction measurements monochromatic X-rays are incident on the analyte, which is generally in the powder form. For crystals and films special attachments and geometries can be used. The beams diffracted from the crystal planes at different angles form constructive diffraction pattern according to Bragg's diffraction equation is discussed above. Each diffraction angle corresponds to particular plane (h, k, l). A pattern in which the intensity of the diffracted X-ray beam is plotted against diffraction angle (2θ) is obtained after the measurements. The lattice parameter (interplanar distance) and the corresponding miller indices for different sets of planes can be obtained from diffraction pattern using Bragg equation. The diffraction peak broadens for tiny crystals depending upon their size. So the crystallite size can be obtained from X-ray diffraction pattern using the Scherrer formula.

$$t = \frac{0.9\lambda}{\beta cos\theta}$$

Where, t is the crystallite size, λ is the wavelength of the X-ray, β is the full width at half maxima (FWHM) of the peak corresponds to the diffraction angle θ.

2.2.2 Raman Spectroscopy

Raman spectroscopy is a powerful technique used to get information about rotational, vibrational and other low frequency transitions in molecules.[16, 17] Raman spectroscopy is based on the inelastic scattering of photons. When a beam of light passes through material, it can undergo scattering. Elastic scattering occurs when the energy of the scattered radiation is same as that of incident one and is called Rayleigh scattering. However, the incident photon may interact and exchange energy with the sample and the scattered photon will have energy different from that of the incident photon. This is called inelastic or Raman scattering. Raman scattering can be of two different types. The energy level diagram for Raman and Rayleigh scattering is shown in the figure 2.5. In the case of Rayleigh scattering a photon with energy '*hv*' interacts with the particle and it results in the excitation of electrons from ground state to the excited state and later de-excite back to ground state by emitting photons of same energy 'hv'.

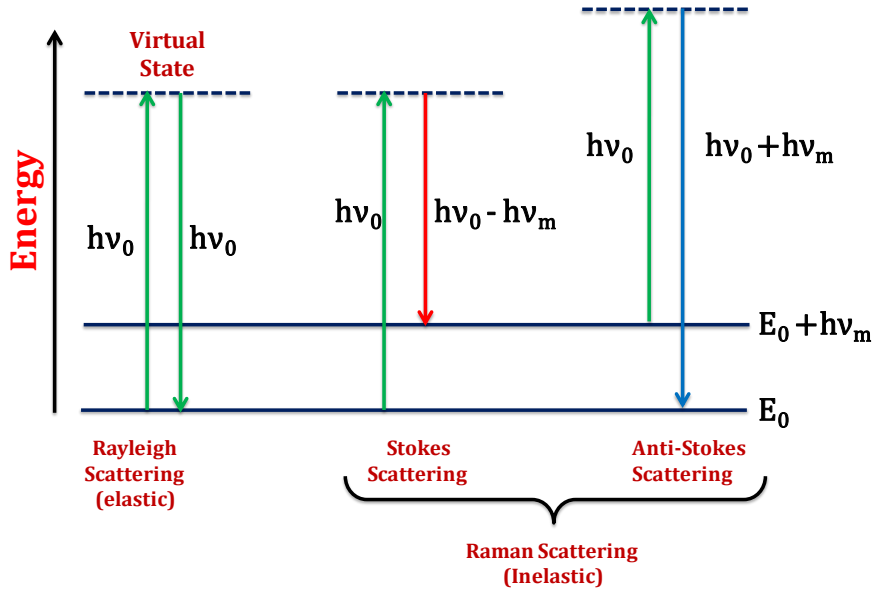

Figure 2.5 Energy level diagram illustrating the states involved in Raman scattering

In the case of Raman scattering the photon undergoes inelastic scattering either by gaining or loosing energy due to the transition in the energy level of the molecule. As a result of these interactions, the resultant Raman spectrum shows either Stokes or

anti-Stokes lines. In case of Raman Stokes scattering, the re-emitted radiation by the molecule/particle is hν-ΔE i.e. a fraction of energy from the incident radiation is absorbed by the molecule. That absorbed amount is ΔE and the corresponding frequency is ν-ΔE/h. When the energy of the photon scattered by the molecule/particle is more than the incident photon energy, i.e hν+ΔE the scattering is termed as Raman anti-Stokes scattering. Hence the additional energy is radiated by the particle/molecule during the scattering process and the resultant frequency is ν+ΔE/h. Stokes scattering is more prominent than anti-stokes as anti-stokes scattering can occur only when molecule is initially in an excited state.

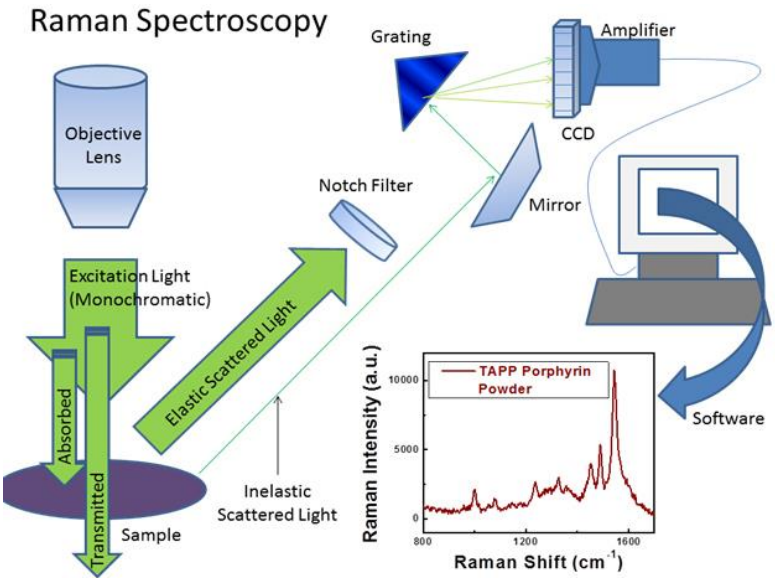

Figure 2.6 Schematic showing the process involved in collecting Raman Spectra (https://www3.nd.edu/~kamatlab/facilities_spectroscopy.html)

The schematic diagram of a Raman Spectrometer is shown in the Figure 2.6. The four major constituents of a Raman spectrometer are laser, sample illumination system and light collection optics, wavelength selector, and a detector. A sample is illuminated by a monochromatic intense laser beam in the ultraviolet, visible or near IR range. The scattered light is then collected by a lens and then passed in to grating monochromator to obtain the Raman spectrum. The signal is measured by a sensitive PMT and after amplification; it is usually processed by a computer which plots the Raman spectrum.

2.2.3 Thermogravimetric Analysis (TGA)

Thermogravimetric analysis a technique used to study the changes in the physical and chemical properties a material with change in the temperature. TGA is commonly used to understand the decomposition or oxidation of material while heating under different conditions based on the mass loss or gain based on the reaction during heating. Thermal stability of wide variety of materials such as metals, polymers, organic compounds, plastics, ceramics, glasses, composites and carbon materials can be analyzed.[18-21] TGA can also provide information about reaction kinetics, decomposition mechanism and percentage of organic as well as inorganic contents in the sample.

Figure 2.7 shows the schematic diagram of a TGA apparatus. The main components of TGA are high precision weighing balance and a high temperature programmable furnace. The sample to be analysed is placed on an electric furnace. The furnace is equipped with a thermocouple to measure the temperature accurately.

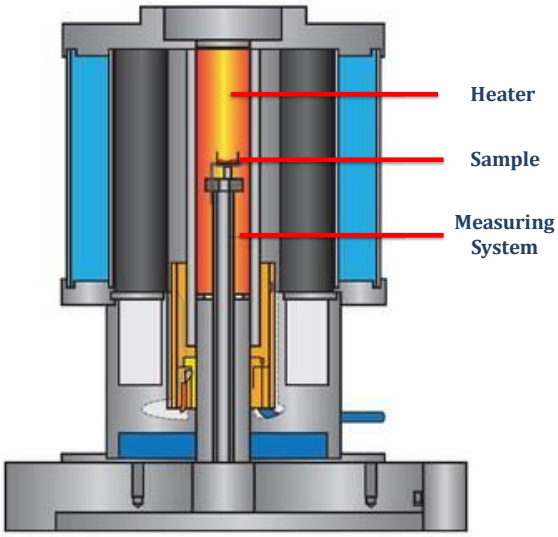

Figure 2.7 Schematic representation of a TGA apparatus (http://www.linseis.com/our-products/thermogravimetry/)

TGA monitors the weight of the sample during heating. During heating the sample undergoes decomposition or oxidation depending upon the atmosphere present (inert/air) and a change in the weight will be observed as a result. A plot with temperature on X- axis and weight or weight loss on the Y-axis will be obtained. TGA data of porous graphene in air atmosphere is shown in figure 2.8.

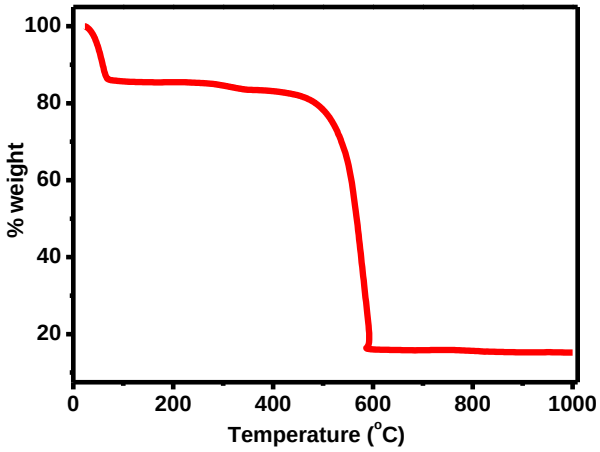

Figure 2.8 TGA plots of porous graphene in air.

2.2.4 Field Emission Scanning Electron Microscope (FESEM)

Electron microscopy techniques use electron beam to image sample. FESEM is a surface imaging technique used to analyse the morphology of materials at high resolution.[22, 23] FESEM uses high energy electrons ejected from a field emission gun to generate the images of sample surface. The schematic diagram of FESEM is shown in figure 2.9.

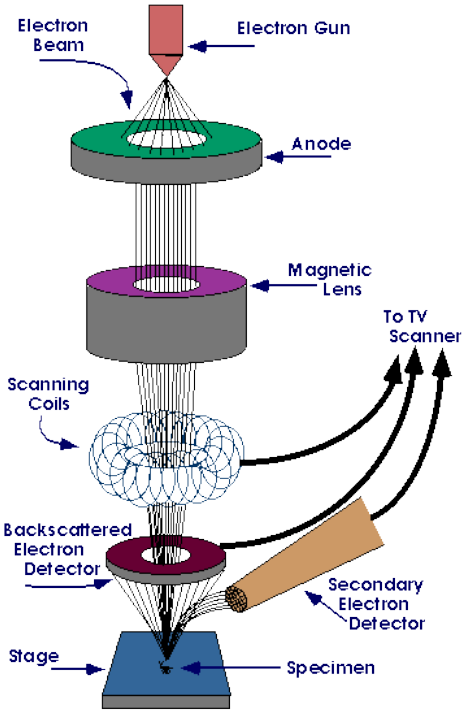

Figure 2.9. Scanning electron microscopy (https://www.purdue.edu/ehps/rem/rs/sem.htm)

It consists of a tip having diameter in the order of 100nm made of a field emission material from which a high intensity beam of electrons emanates under an applied field. The electrons are accelerated by an electric field gradient and are deflected and focussed by magnetic lenses to produce narrow beam of electrons.

When an electron impinges on the sample, various types of signals are originated from the surface of the sample. The secondary electrons emitted from the atom due to inelastic scattering are used for the SEM imaging.

These electrons are collected and accelerated by applying high positive potential. Photomultiplier tube generate electrical signal corresponding to the intensity of secondary electrons and the electrical signal is displayed as a 2D intensity distribution which can be viewed as digital image. When an electron gets removed from the inner shell the atom rearranges itself by dropping an electron from the outer shell by emitting an electron called Auger electron and is used to study the compositional information.

2.2.5 Energy Dispersive X-ray Analysis (EDAX)

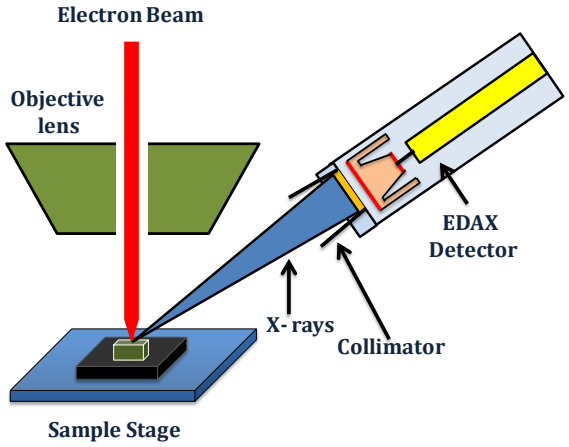

Figure 2.10 Schematic representation energy dispersive X-ray analyses

Energy dispersive X-ray analysis, also called as energy dispersive X-ray spectroscopy, is a technique used to get the chemical composition of the sample.[24] The basic working principle of EDAX is that each element has unique X-ray emission spectrum due to unique atomic structure. When an electron get removed from the inner shell by creating a hole, the atom equilibrates itself by dropping an electron from the outer shell by emitting an X-ray radiation of energy equal to the difference

between the two levels. The emitted X-rays are detected by energy dispersive measurement. Figure 2.10 shows a typical schematic of an energy dispersive X-ray spectrometer. EDAX spectrum and the elemental composition (inset) obtained are shown in figure 2.11.

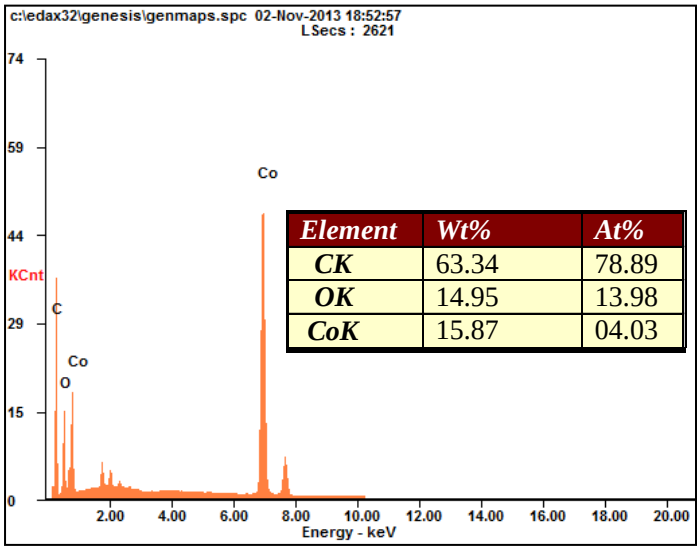

Figure 2.11 Elemental composition obtained from EDAX

2.2.6 Transmission Electron Microscope (TEM)

TEM is the most powerful technique used in the field of nanoscience and nanotechnology. The advantage of TEM over SEM is its unique capability to resolve the crystal lattice as it uses several hundred kilovolts of electron energy. The schematic diagram of a typical TEM is shown in figure 2.12. Here, high energy electrons beam is transmitted through an ultra-thin film of the sample. The column consists of an electron source, electrodes for accelerating electrons and electromagnets for focussing and deflecting electron and an electron detection system such as CCD. When the electron beam interacts with the sample, various phenomena such as secondary electron emission, back scattering of electrons, X-ray emission and transmission of electrons take place. The transmitted electrons are analysed in TEM. Angular distribution of scattering can be viewed in the form of diffraction patterns known as selected area diffraction patter (SAED). The d spacing between the lattice planes can be obtained from a SAED pattern using the formula

$$dr = \lambda L$$

where, L is the distance between the specimen and the photographic plate and r is the radius of the diffracted rings.

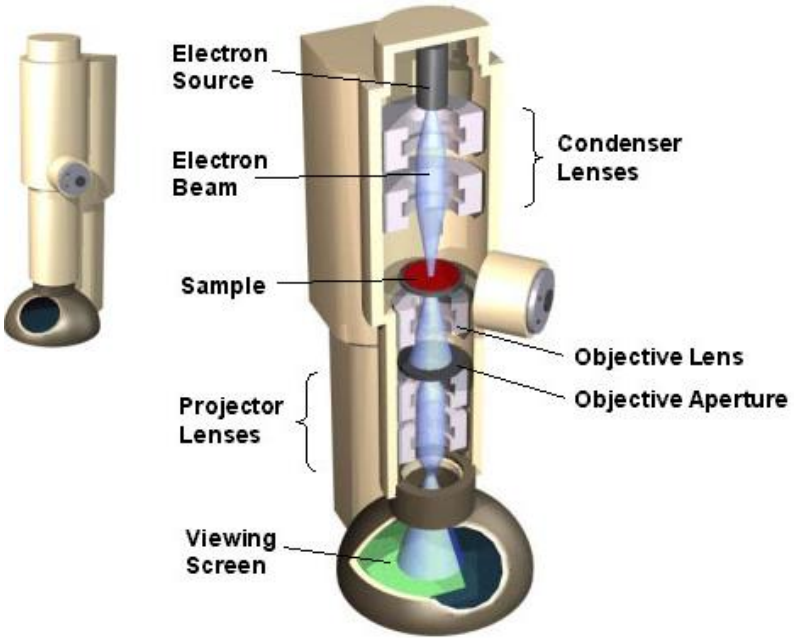

Figure 2.12 Schematic of representation of various parts and construction of a transmission electron microscope

(http://barrett-roup.mcgill.ca/tutorials/nanotechnology/nano02.htm)

2.2.7 X-ray Photoelectron Spectroscopy (XPS)

X-ray Photoelectron Spectroscopy, or XPS, also known as electron spectroscopy for chemical analysis (ESCA) is a surface technique used to get information on elemental composition, chemical state and empirical formula of a material.[25] The basic working principle of XPS is photoelectric effect in which electrons are emitted from the atom when light incident on it. The schematic of the working mechanism of XPS is shown in figure 2.13.

XPS spectra are obtained by measuring the kinetic energy and number of the emitted electrons upon irradiation by X-rays. The electrons emitted from 0-10 nm. When a photon is incident on a metal surface, electrons are emitted from the surface. The kinetic energy of the emitted electron (KE) will be equal to the difference between the energy of the incident photon (hν) and the energy required to remove the electron from the atom and it can be represented by

$$KE = h\nu - \varphi - E_b,$$

where, h is the Plank's constant ν is the incident photon frequency and E_b is the binding energy of the electron.

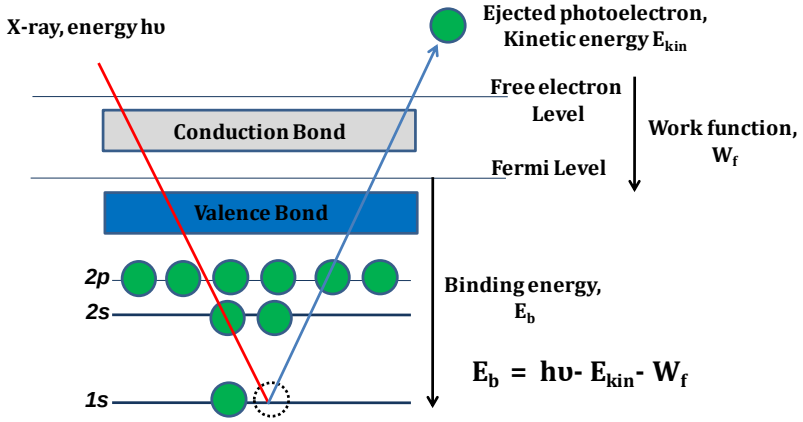

Figure 2.13 Schematic representation of working principle of XPS

As the energy of the incident X-ray beam and φ are known factors, the binding energy of the electron can be obtained after measuring the kinetic energy of the emitted electron. Figure 2.14 shows basic components and working of a XPS spectrometer.

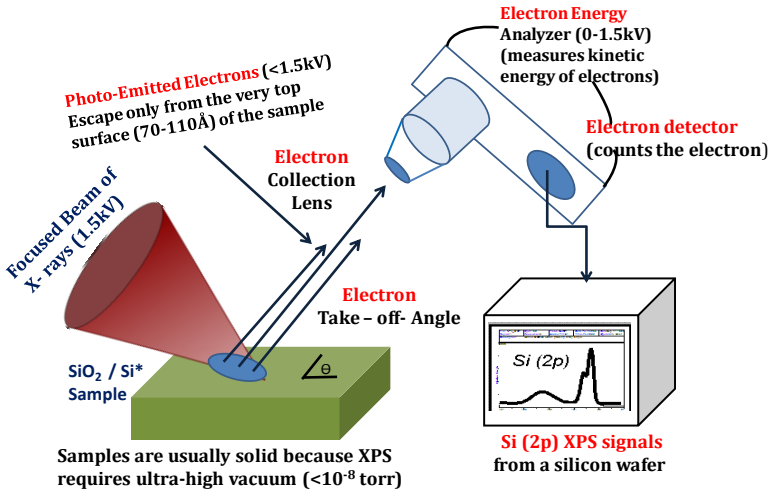

Figure 2.14 Schematic of construction and components of monochromatic X-ray photon electron spectrometer

It consists of an X-ray source, an ultrahigh vacuum chamber, sample introduction chamber, sample stage, electron collection lens, electron energy analyser, magnetic field shielding and an electron detector system. Usually Al and Mg are used as the source for X-ray to generate photoelectron from the sample. Monochromatic X-ray or

UV radiation falls on the sample and ejected electrons pass between a pair of electrically charged hemispherical plates which act as an energy filter, allowing electrons of only a particular kinetic energy to pass through, the pass energy - Epass. The resulting electron current, measured by an electron multiplier, indicates the number of electrons ejected from the surface with that kinetic energy. The number of photoelectrons with different kinetic energy is measured which corresponds to electron with different binding energy. A plot of binding energy on x-axis and intensity on y-axis is obtained after the measurement. The binding energy of the electron will vary with element and its electronic state.[26]

In the current work, the XPS measurements of different samples were carried out on a VG MicroTech ESCA 3000 instrument at the Centre for Materials Characterizations (CMC), National Chemical Laboratory, Pune. The core level binding energies (BE) were corrected with the carbon binding energy of 284.7eV.

2.2.8 BET Surface area Analysis

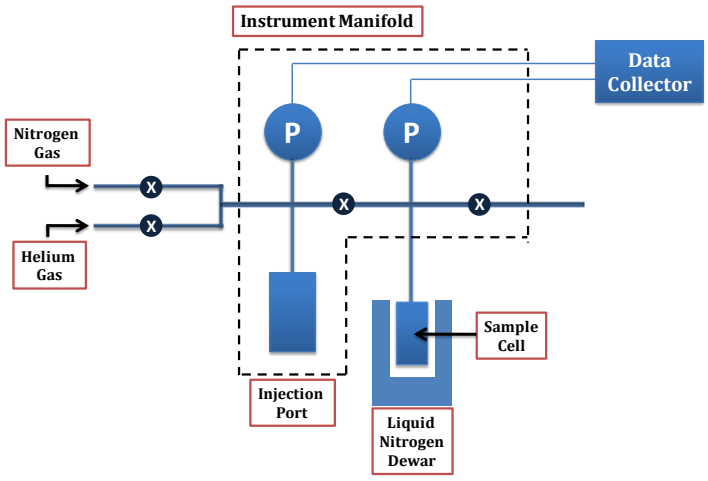

Figure 2.15 Schematic of BET apparatus

The specific surface area and pore size distribution of a material can be obtained from BET measurements. BET surface area measurement is based on the adsorption of gas molecules on the surface of the material.[27] Figure 2.15 shows the schematic representation of BET apparatus. Multilayer adsorption of non-corrosive gases like nitrogen, argon, carbon dioxide etc. is used as the adsorbate for the BET analysis. The first paper on BET was published by three scientists Stephen Brunauer, Paul Hugh Emmett, and Edward Teller in 1938.[28] The three main hypotheses of BET adsorption-

desorption measurements are (a) the adsorbate gas molecules adsorb physically adsorb on the solid material in infinite layers, (b) no physical interaction occurs between the layers of gas molecules, and (c) each layer follows Langmuir theory of adsorption. The BET model of gas adsorption on solid surface is shown in figure 2.16.

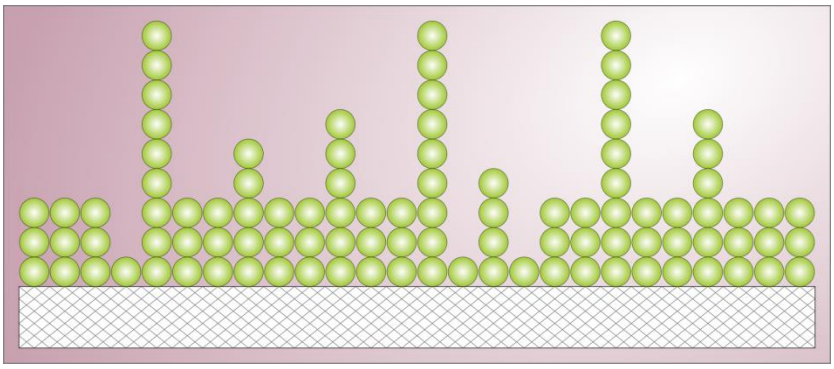

Figure 2.16 BET model of multilayer adsorption of gas molecules on the surface of solid material (https://en.wikipedia.org/wiki/BET_theory)

The BET equation can be expressed as

$$\frac{1}{v[\left(\frac{P_0}{P}\right)-1]} = \frac{c-1}{v_m c}\left(\frac{P}{P_0}\right) + \frac{1}{v_m c} \qquad (1)$$

Where, v is the volume adsorbed, P and P_0 are the equilibrium and saturation pressure of adsorbate at the adsorption temperature, v_m is the monolayer adsorbed gas quantity and c is the BET constant and can be expressed as

$$c = e^{\frac{E_1 - E_L}{RT}}$$

E_1 and E_L are the heats of adsorption for the first and next layers, respectively. An adsorption isotherm can be plotted from the equation (1) with $\frac{1}{v[\left(\frac{P_0}{P}\right)-1]}$ on y-axis and $\frac{P_0}{P}$ on the x-axis giving straight line. The plot is linear in the low pressure region usually P/P_0 from 0.05 to 0.35. The intercept and slope are used to calculate the monolayer adsorbed gas quantity v_m and constant c. The total and BET specific surface area are given by

$$S_{total} = \frac{v_m N s}{V} \text{ and } S_{BET} = \frac{S_{total}}{a}$$

Where v_m is the molar adsorbed gas volume, N is Avogadro number, s is the adsorption cross section of gas molecule, V is the molar volume of the gas molecule and a is the mass of the sample. The porous nature of the sample can be obtained from the type of adsorption-desorption isotherm as it is different for materials with different types of porosity. All the adsorption –desorption measurements were done at liquid nitrogen temperature (77K) using N_2 as the adsorbate molecule.

2.3 Electrochemical Measurements

Electrochemical measurements such as cyclic voltammogram, chronopotentiometry and electrochemical impedance spectroscopy were done for the performance evaluation of samples prepared for battery and supercapacitor electrodes. The electrochemical characterizations were performed using Autolab, Biologic potetntiostats and Arbin battery analyser. The supercapacitor measurements were done in a two electrode symmetric cell with active material on both the electrodes. The materials for battery electrodes were tested in the half cell configuration with the active material as the working electrode and lithium metal as both counter and reference electrodes.

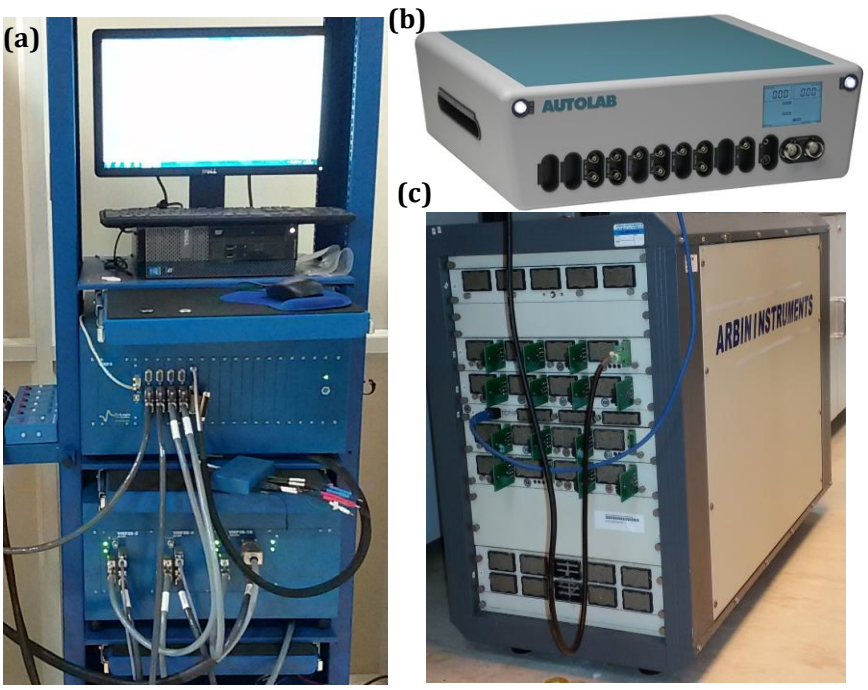

Figure 2.17 (a) Biologic and **(b)** Autolab Potentiostats and **(c)** Arbin Battery Tester

2.3.1 Cyclic voltammetry (CV)

Cyclic voltammetry is the most common technique used in electrochemistry to get qualitative information about electrochemical reactions. It is used to study the redox reactions, oxidation and reduction potential, reaction kinetics and reversibility of redox reactions in electrochemical systems.[29] Cyclic voltammetry is extensively used for characterizing the electrochemical energy storage and conversion systems such as batteries, supercapacitors, solar cells, fuel cells and water splitting.

The CV measurements are usually performed in a three electrode system. The three electrodes include reference electrode, counter electrode and working electrode.[30] The material for analysis is usually coated on a support with high electrical conductivity is used as working electrode, platinum or graphite is used as the counter electrode. Different reference electrodes are used based on the electrolyte used. Commonly used reference electrodes for experiments are saturated calomel electrode (SCE), silver chloride electrode (Ag/AgCl) and reversible hydrogen electrode. The cathodic and anodic peak positions for the same system will be different when different reference electrode is used.

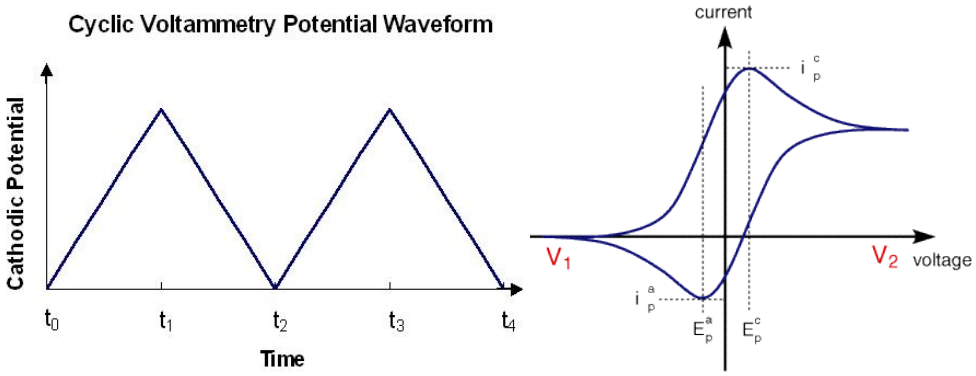

Figure 2.18 (a) Wave form of cyclic voltammetry **(b)** Typical cyclic voltammogram for the potential sweep from V_1 to V_2. i_p^c and i_p^a denotes cathodic and anodic peak current respectively and E_p^c and E_p^a are corresponding potential (https://en.wikipedia.org/wiki/Cyclic_voltammetry)

In the CV experiment the potential is varied from V_1 to V_2 between the working electrode and the reference electrode at a constant ramp in a time interval from t_1 to t_2. The rate in which the voltage varies is called scan rate (V/s). After the working electrode potential is reached the set potential (V_2), it is ramped in the reverse

direction to the initial potential (V_1) from t_2 to t_3. The waveform of a CV applied potential is shown in figure 2.18a. The current between the working electrode and counter electrode is measured with change in potential. A plot with applied potential (working electrode potential) on the X- axis and current on the Y-axis obtained as shown in figure 2.18b.

2.3.2 Galvanostatic Charge discharge

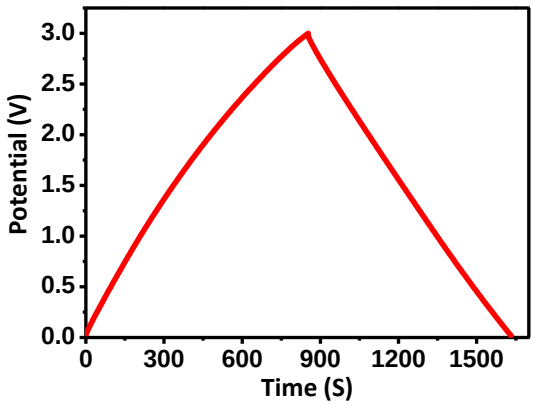

Figure 2.19 Typical charge discharge data of a double layer capacitor

Galvanostatic charge discharge is a technique most widely used to measure the charge storage capacity and cyclic stability of electrochemical energy storage device such as supercapacitors and batteries.[31] In the experiment constant current is applied between the working and counter electrode and variation of the potential with time is measured. Figure 2.19 shows the charge discharge data for a supercapacitor. The potential window for the charge discharge measurement is decided based on various factors such as the electrode material and electrolyte used. The specific capacitance, 'C' in Fg^{-1} for a supercapacitor can be calculated from the charge-discharge measurement using the formula[31]

$$C = \frac{2I}{m\frac{dv}{dt}}$$

Where, 'I' is the applied current, m is the loading of the active material on each electrode and $\frac{dv}{dt}$ is the slope of the discharge curve.

2.3.3 Electrochemical Impedance Spectroscopy (EIS)

Electrochemical impedance spectroscopy is a very sensitive and most powerful technique used to study the electrode-electrolyte interface.[32] It is widely used to obtain the double layer capacitance and series resistance in the case of supercapacitor.[33] It gives information about the sources of Ohmic losses (impedance or resistance) in a system.[34]

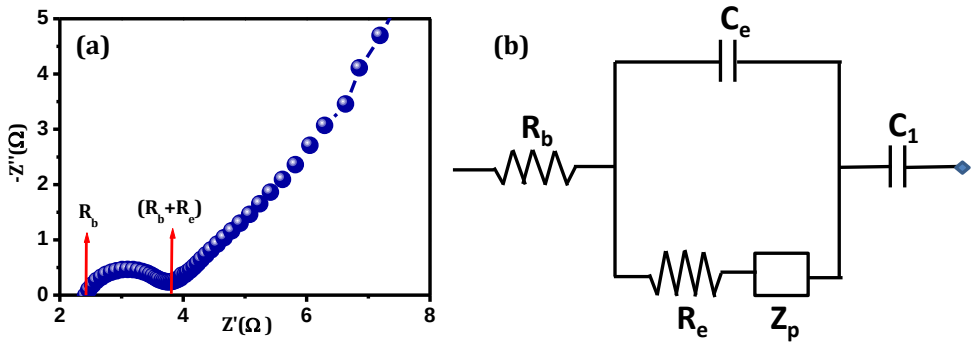

Figure 2.20 **(a)** Nyquist plot **(b)** Corresponding equivalent circuit for carbon based supercapacitor

In the impedance measurements the electrochemical system is perturbed by AC signal of small amplitude. The response of the system is measured for wide range of frequencies varying from 100nHz -1MHz. The variation of real and imaginary parts of the impedance and phase angle with frequency gives information about the reaction kinetics, diffusion of electrolyte ions. Graph obtained by plotting real impedance (Z') on X-axis and imaginary part (Z") on Y-axis is called Nyquist plot. Nyquist plot gives the series resistance, charge transfer resistance, various electrode-electrolyte interfaces and the components at the interfaces in an electrochemical system.[35] The Nyquist plot for a carbon based supercapacitor and equivalent circuit diagram are shown in the figure 2.20a and b respectively. The X- intercept (R_b) gives the series resistance of the system which includes the resistance of the electrode, current collector and electrolyte. The diameter of each semicircle (R_e) in the Nyquist plot gives the charge transfer resistance at the interfaces.

Another plot obtained from the impedance measurements is the Bode plot in which the change in the phase angle with frequency is plotted.[36] The Bode angle at different frequencies tells about the behaviour of the interface at that frequency. At very low frequencies the interface behaves like a capacitor due to the double layer formation.

For an ideal capacitor the Bode phase is 90°. In the case electrical double layer capacitors, better the capacitive property more the phase angle even at higher frequencies.

2.4 References

1. D. Kalpana, S. H. Cho, S. B. Lee, Y. S. Lee, R. Misra and N. G. Renganathan, *J. Power Sources*, 2009, **190**, 587-591.
2. M.-C. Liu, L.-B. Kong, C. Lu, X.-M. Li, Y.-C. Luo and L. Kang, *RSC. Advances.*, 2012, **2**, 1890-1896.
3. L. L. Zhang and X. S. Zhao, *Chem. Soc. Rev.*, 2009, **38**, 2520-2531.
4. J.-S. Lee, S.-I. Kim, J.-C. Yoon and J.-H. Jang, *ACS Nano*, 2013.
5. Y. S. Yun, S. Y. Cho, J. Shim, B. H. Kim, S.-J. Chang, S. J. Baek, Y. S. Huh, Y. Tak, Y. W. Park, S. Park and H.-J. Jin, *Adv. Mater.*, 2013, **25**, 1993-1998.
6. J. Romanos, M. Beckner, T. Rash, L. Firlej, B. Kuchta, P. Yu, G. Suppes, C. Wexler and P. Pfeifer, *Nanotechnology*, 2012, **23**, 015401.
7. J. A. Maciá-Agulló, B. C. Moore, D. Cazorla-Amorós and A. Linares-Solano, *Carbon*, 2004, **42**, 1367-1370.
8. R. Ryoo, S. H. Joo and S. Jun, *The Journal of Physical Chemistry B*, 1999, **103**, 7743-7746.
9. M. M. Titirici, A. Thomas, S.-H. Yu, J.-O. Müller and M. Antonietti, *Chem. Mater.*, 2007, **19**, 4205-4212.
10. M.-M. Titirici and M. Antonietti, *Chem. Soc. Rev.*, 2010, **39**, 103-116.
11. A. Funke and F. Ziegler, *Biofuels, Bioproducts and Biorefining*, 2010, **4**, 160-177.
12. J. Drenth, in *Encyclopedia of Molecular Biology*, John Wiley & Sons, Inc., 2002.
13. U. Holzwarth and N. Gibson, *Nat Nano*, 2011, **6**, 534-534.
14. L. R. B. Elton and D. F. Jackson, *Am J Phys*, 1966, **34**, 1036-1038.
15. W. H. Bragg and W. L. Bragg, *Proceedings of the Royal Society of London A: Mathematical, Physical and Engineering Sciences*, 1913, **88**, 428-438.
16. G. Keresztury, in *Handbook of Vibrational Spectroscopy*, John Wiley & Sons, Ltd, 2006.
17. G. S. Bumbrah and R. M. Sharma, *Egyptian Journal of Forensic Sciences*.

18. P. K. Chatterjee and C. M. Conrad, *Journal of Polymer Science Part A-1: Polymer Chemistry*, 1968, **6**, 3217-3233.
19. D. Bom, R. Andrews, D. Jacques, J. Anthony, B. Chen, M. S. Meier and J. P. Selegue, *Nano Lett.*, 2002, **2**, 615-619.
20. Y. Xu, W. Hong, H. Bai, C. Li and G. Shi, *Carbon*, 2009, **47**, 3538-3543.
21. X. Zhu, Y. Zhu, S. Murali, M. D. Stoller and R. S. Ruoff, *ACS Nano*, 2011, **5**, 3333-3338.
22. K. C. A. Smith and C. W. Oatley, *British Journal of Applied Physics*, 1955, **6**, 391.
23. A. V. Crewe, J. Wall and L. M. Welter, *J. Appl. Phys.*, 1968, **39**, 5861-5868.
24. J. S. Heslop-Harrison, in *Physical Methods in Plant Sciences*, eds. H.-F. Linskens and J. Jackson, Springer Berlin Heidelberg, 1990, pp. 244-277.
25. J. M. Hollander and W. L. Jolly, *Acc. Chem. Res.*, 1970, **3**, 193-200.
26. P. van der Heide, in *X-Ray Photoelectron Spectroscopy*, John Wiley & Sons, Inc., 2011, pp. 27-60.
27. K. S. W. Sing, *Adv. Colloid Interface Sci.*, 1998, **76–77**, 3-11.
28. S. Brunauer, P. H. Emmett and E. Teller, *J. Am. Chem. Soc.*, 1938, **60**, 309-319.
29. R. S. Nicholson, *Anal. Chem.*, 1965, **37**, 1351-1355.
30. G. A. Mabbott, *J. Chem. Educ.*, 1983, **60**, 697.
31. M. D. Stoller and R. S. Ruoff, *Energy Environ. Sci.*, 2010, **3**, 1294-1301.
32. U. Retter and H. Lohse, in *Electroanalytical Methods*, ed. F. Scholz, Springer Berlin Heidelberg, 2002, pp. 149-166.
33. P. L. Taberna, P. Simon and J. F. Fauvarque, *J. Electrochem. Soc.*, 2003, **150**, A292-A300.
34. Y. Zhu, S. Murali, M. D. Stoller, K. J. Ganesh, W. Cai, P. J. Ferreira, A. Pirkle, R. M. Wallace, K. A. Cychosz, M. Thommes, D. Su, E. A. Stach and R. S. Ruoff, *Science*, 2011, **332**, 1537-1541.
35. M. Toupin, D. Bélanger, I. R. Hill and D. Quinn, *J. Power Sources*, 2005, **140**, 203-210.
36. D. Chunsheng and P. Ning, *Nanotechnology*, 2006, **17**, 5314.

Chapter 3

3D micro-porous conducting carbon beehive by single step polymer carbonization for high performance supercapacitor and Li-ion hybrid capacitor: The magic of *in situ* porogen formation

Carbon material with interconnected hierarchical structure was synthesized by direct pyrolysis of poly(acrylamide-co-acrylic acid) potassium salt in inert atmosphere without any external activation agent. The presence of the alkali metal in the selected polymer precursor results in a high specific surface area of 1327 m^2g^{-1}. The presence of three different types of pores makes the material ideal for supercapacitor electrodes. The IMPC was tested as an electrode in aqueous and non-aqueous supercapacitors. The material also showed better performance as cathode material for Lithium-ion hybrid capacitor in comparison with commercial supercapacitor carbon.

3.1 Introduction

The increased demand for energy and rapid consumption of fossil fuels (causing serious pollution problems) have intensified the research and development efforts on new and efficient sustainable energy technologies[1,2]. Highly efficient energy conversion from sustainable resources and effective low cost and durable storage of electrical energy are two primary ways to achieve the goals of the modern world without compromising our environment.

Supercapacitors are considered to be one of the promising energy storage technologies because of their applicability in various new and novel device systems[3]. Based on the energy storage mechanism supercapacitors are classified into electrical double layer capacitors (EDLCs) and pseudo-capacitors[4]. EDLCs store charge by pure electrostatic interaction between electrode and the electrolyte ions whereas fast surface redox reactions are involved in pseudo-capacitors[5]. EDLCs possess higher power density and longer cyclic stability as compared to pseudo-capacitors and other electrochemical energy storage devices such as batteries[6]. However the lower energy density still limits the commercialization of EDLCs. Intense research is still being performed to improve the energy density without losing its high power density cyclic stability. Carbon based materials such as activated carbon, CNT and graphene have been tested for EDLC electrodes[7-9]. Even though graphene and CNTs have higher electrical conductivity, the maximum capacitance obtained from these materials is still behind that rendered by the activated carbon family because of the lower practical surface area and lack of porous structure which limit the active area for charge storage[10]. To improve upon these factors, synthesis of high surface area porous graphene has been pursued by KOH activation or by templated synthesis approaches which are essentially multistep methods[11] . Hence search is still on for novel methods to synthesize high surface area carbons with optimum porosity. Towards this end metal organic frame works[12, 13], metal carbides[14, 15], polymer precursors[16, 17], hard template mediated synthesis[18, 19] etc. have been used to obtain micro/mesoporous carbon structures. The main disadvantages of these methods are less yield and complexity and expense for scale-up due to the multiple steps involved. Direct pyrolysis of carbonaceous materials represents perhaps the most facile and promising method for the synthesis of porous carbon.

Until now there are a limited number of interesting reports on the synthesis of

high surface area porous carbon by direct pyrolysis without any external activation agent[20]. Polymers are one of the ideal precursors to get carbon by direct pyrolysis. Zhong et al[21] synthesized porous carbon from the co-polymer of polyacrylonitrile (PAN) and poly(n-butyl acrylate) (PBA). Surface area of 500 m^2g^{-1} was achieved without any activation for which the specific capacitance obtained was 160F g^{-1} in 1M H_2SO_4. Post-activation the surface area improved to 2520 m^2 g^{-1} and capacitance to 176 Fg^{-1}. Graphene aerogels and other three dimensional carbon nanostructures have attracted considerable attention as electrode materials for EDLCs because the wide pore size distribution which includes macropores, mesopores and micropores[9]. Until now there are very few reports on the synthesis of 3D carbon structure by direct pyrolysis. Recently Qie et al[16] has reported 3D carbon form polymer pyrolysis for supercapacitor electrodes. In this work we report a single step synthesis of interconnected microporous carbon having beehive morphology on by the pyrolysis of the copolymer poly(acrylamide-*co*-acrylic acid) potassium salt. We show that this interesting choice of the polymer precursor directly leads to conducting and porous carbon by its high temperature pyrolysis without any activation and also renders excellent charge storage properties.

Application of such supercapacitors are however limited because of their lower energy density. Conversely, LIBs exhibit much higher energy density as compared to supercapacitors but their lower power capability and limited cyclability prohibits their use in high power applications likely hybrid electric vehicles (HEV) and electric vehicles (EV)[22, 23]. In order to overcome these energy *vs.* power conflicts in a single device configuration, researchers are now working on the integration of both the storage concepts, namely the LIBs and supercapacitors, with the interesting hybrid device design named as the Li-ion hybrid electrochemical supercapacitors (Li-HEC)[24-31].

In Li-HEC assembly, Li-ion insertion type materials are utilized as anodes which undergo Faradaic reaction mechanism as in LIBs, thereby providing sufficient energy density to the system. On the other hand, charge carriers accumulated over the high surface area of carbonaceous materials, such as activated carbon (AC), lead to the formation of anion double layer obeying the non-Faradaic mechanism, which translates into higher power density of the system[24, 25]. As a result, Li-HEC possesses high energy density than EDLC and high power density than LIB[26]. As for EDLCs, utilization of aqueous electrolyte in Li-HEC is highly restricted due to the water

splitting issue (~1.23 V)[32]. Consequently, Amatucci *et al.*[24] first reported the electrochemical performance of Li-HEC comprising AC as cathode and spinel phase $Li_4Ti_5O_{12}$ as anode in the conventional non-aqueous electrolyte solution and could deliver an energy density of ~10 Wh kg^{-1}. Some reports are available for the utilization of various kinds of insertion type anodes for Li-HEC applications; for instance anatase TiO_2 [33], TiO_2-B [34, 35], $LiCrTiO_4$ [36, 37], $Li_4Ti_5O_{12}$ [26-31], $LiTi_2(PO_4)_3$ [38], TiP_2O_7 [39], β-FeOOH [40], α-MnO_2 [41] etc. Among them, spinel phase $Li_4Ti_5O_{12}$ is found to be quite promising based on the following facts: (i) very high columbic efficiency when cycled at high current rates (>96%) with close to the theoretical capacity of 175 mAh g^{-1} for reversible insertion of three moles of Li, (ii) thermodynamically flat cycling profile (~1.55 V *vs.* Li) associated with two-phase reaction, (iii) zero-strain insertion that provides no volume change during Li-insertion/extraction, (iv) no solid electrolyte interface layer formation, (v) inexpensive raw materials and easy preparation protocols, and (vi) eco-friendliness[27, 42]. While the work on inorganic systems (oxides and hydroxides) for Li-HEC has progressed, the research on the development of carbonaceous electrodes for this application needs to pick up pace.

Recently, Stoller *et al.*[43] reported the performance of KOH treated microwave exfoliated graphite oxide as cathode active material along with $Li_4Ti_5O_{12}$ anode and such Li-HEC delivered the energy density of 40.8 Wh kg^{-1}. Later, Aravindan *et al.*[44] demonstrated the utilization of trigol reduced graphene oxide as cathode active material along with $Li_4Ti_5O_{12}$ anode and achieved a maximum energy density of 45 Wh kg^{-1}. Unfortunately, the scalability, reproducibility and energy cost are rather complicated issues for such graphene based materials since, according to Vargas *et al.*[45], graphene quality varies from technique to technique and batch to batch, rendering entirely different electrochemical profile in different cases. Therefore, research focus is now being directed towards the development of high surface area porous carbons (such as IMPC) derived from either bio-waste or polymers [46-48]. The main advantage of utilizing such carbons is the realization of wide range of pore size distribution, which enables more active sites for the accumulation of charge carriers. As a result, high specific capacitance can be anticipated for such carbon based supercapacitors irrespective of the electrolyte medium[20]. In this work, we have evaluated the high surface area three dimensionally architectured porous carbon obtained by single step pyrolysis of a suitably chosen polymer system at high temperature for the Li-HEC application. This carbon shows a very good performance

for the case of EDLC application, as discussed below. [49] In this work, the IMPC material was tested in a single electrode configuration to evaluate the supercapacitive behaviour and the same was subsequently employed as a cathode active material in Li-HEC assembly along with spinel phase $Li_4Ti_5O_{12}$ anode.

3.2 Experimental Methods

3.2.1 Synthesis of the material

The polymer was purchased from Sigma Aldrich and used as it is. The interconnected microporous carbon (IMPC) was synthesized by single step pyrolysis of poly(acrylamide-*co*-acrylic acid) potassium salt ($[CHCO_2RCH]_m[CHCONH_2]_n$) where R = K or H. In our sample potassium content was 9%. Briefly, 10 g of the polymer was heated at 1000 ^oC in flowing Argon atmosphere with a heating rate of 10 ^oC/min in an alumina tube using a split tube furnace. The sample was allowed to cool to room temperature under natural cooling. The carbon powder was then dispersed in water and washed with diluted H_2SO_4 solution to remove the inorganic impurities. After filtration the product was dried at 90 °C. We also examined the effect of adding an activation agent (KOH) to the polymer (1:1 wt.%) before pyrolysis to explore the possibility of further enhancing the surface area and possibly the capacitance.

3.2.2 Structural Characterizations

Powder X-ray diffraction was performed using PAN Analytical powder X ray diffractometer with nickel-filtered Cu Kα radiation to confirm the graphitization of the product. The structure of the product was further discerned by Raman spectroscopy (LabRAM HR800 from JY Horiba). The structural and morphological characterizations were performed by FESEM with FEI Nova NanoSEM 450 and HRTEM (FEI, Tecnai F30, FEG with 300 kV). The surface elemental composition was determined by the X-ray photoelectron spectroscopy technique using VG scientific ESCA-3000 spectrometer using non-monochromatized Mg Kα radiation (1253.6 eV) at a pressure of about 1×10^{-9} Torr. The porous structure of the sample was confirmed by N_2 adsorption-desorption isotherm at 77K (Quadrasorb automatic volumetric instrument).

3.2.3 Electrochemical Measurements

3.2.3.1 Symmetric Superapacitor

Slurry of active material was prepared with 5% binder, 15% conducting carbon and 80% of active material in NMP (N-methylpyrolidone). The slurry was coated on conducting carbon substrate which acts as the current collector. The total material loading on each electrode was approximately 2 mg. The aqueous supercapacitor performance was evaluated in 1M H_2SO_4 solution in a symmetric two electrode system. CV and impedance measurements were done using Autolab Potentiostat with Nova 1.7 and the charge-discharge measurements were performed on Biologic Potentiostat. The non-aqueous supercapacitor measurements were done with a two electrode coin cell assembly. The supercapacitor was fabricated with an active material loading of 5 mg for each electrode. The weight of the total cell was 2.02 g. The diameter (thickness) of the material coating was 16 mm (0.1 mm). The total outside coin cell dimension was: diameter 20 mm and thickness 1.6 mm. Electrochemical measurements such as cyclic voltammogram, charge-discharge and impedance spectroscopy were performed in 1M $LiPF_6$ in ethylene carbonate/di-methyl carbonate in the potential rang 0-3V.

3.2.3.2 Li - ion Hybrid Electrochemical Capacitor

All the electrochemical studies were performed in standard CR 2016 coin-cell configuration at ambient temperature conditions. The composite electrode was formulated with accurately weighed 10 mg of active material (IMPC or $Li_4Ti_5O_{12}$), 1.5 mg of conductive additive (Super P) and teflonized acetylene black (TAB-2) using ethanol. The composite film was pressed over 200 mm^2 area stainless steel mesh (Goodfellow, UK). Half-cell assembly (single electrode configuration) measurement was performed using the composite electrode and lithium, in which lithium acts as both the counter and the reference electrode. The working and reference electrodes were separated by microporous glass fibre separator (Whatman, Cat. No. 1825-047, UK) and filled with 1 M $LiPF_6$ in ethylene carbonate (EC)/dimethyl carbonate (DMC) (Selectipure LP30, Merck KGaA, Germany) electrolyte solution. Galvanostatic cycling profile measurements were performed using Arbin battery tester at various current densities.

All the electrochemical studies for Li-HEC were performed in standard CR 2016

coin-cell configuration at ambient temperature conditions. The composite electrode was formulated with accurately weighed 10 mg of active material (IMPC or $Li_4Ti_5O_{12}$), 1.5 mg of conductive additive (Super P) and teflonized acetylene black (TAB-2) using ethanol. The composite film was pressed over 200 mm^2 area stainless steel mesh (Goodfellow, UK). Half-cell assembly (single electrode configuration) measurement was performed using the composite electrode and lithium, in which lithium acts as both the counter and the reference electrode. The working and reference electrodes were separated by microporous glass fibre separator (Whatman, Cat. No. 1825-047, UK) and filled with 1 M $LiPF_6$ in ethylene carbonate (EC)/dimethyl carbonate (DMC) (Selectipure LP30, Merck KGaA, Germany) electrolyte solution. Galvanostatic cycling profile measurements were performed using Arbin battery tester at various current densities.

3.3 Results and discussion

3.3.1 Synthesis and Characterization

Figure 3.1 shows the schematic representation of the synthesis of interconnected microporous carbon sheets from the poly(acrylamide-*co*-acrylic acid) potassium salt and the possible mechanism. The selected polymer is a linear chain copolymer of acrylamide and acrylic acid as shown in Figure 3.1. It has been already reported that organic salts with metal cations may results in the formation of high surface area carbon[17, 50]. The advantage of having the alkali metal cation is that it can be washed out easily from the carbon matrix. Here both the acryl amide and acrylic acid acid components act as the source of carbon.

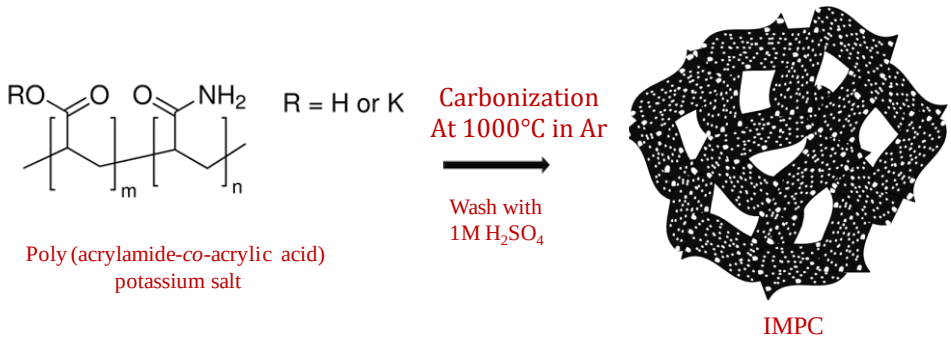

Figure 3.1 Schematic diagram representing creation of pores in the carbon sheets

High temperature pyrolysis of polymer in inert atmosphere results into carbonization. At our maximum pyrolysis temperature of 1000 ^oC full graphitization cannot occur,

but tiny nanoscale graphitic units form which assemble in topological disorder. Such carbon is referred to as turbostratic carbon[51]. The presence of potassium in the polymer results in the formation of K_2CO_3 during carbonization by reacting with the carbon, which creates pores in the carbon frame work.

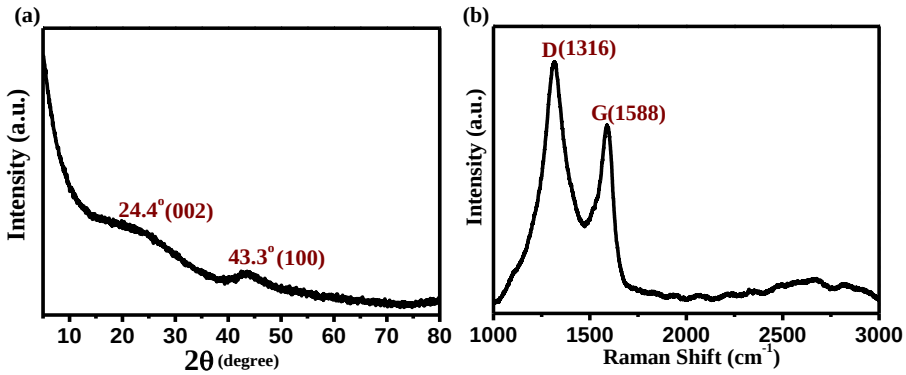

Figure 3.2 (a) Powder XRD pattern and **(b)** Raman spectra of IMPC

The inorganic product formed during this reaction gets removed easily after washing. Figure 3.2a shows the powder XRD pattern of IMPC. The two peaks positioned near to 24.4° and 43.3° confirm the graphitisation in the carbon. The broad peak positioned around 24.4° corresponds to (002) plane of turbostratic carbon[52]. The low intensity and broadening indicates that IMPC consists of thin carbon sheets[53]. The large intensity in the low angle region is due to the high pore density in the carbon sheets[53]. The Raman spectrum presented in the Figure 3.2b shows the characteristic representative of disordered carbon[54]. The peak positioned around 1588 cm^{-1} corresponds to the G band attributed to E_{2g} phonon vibrations of sp^2 carbon atoms[55]. The peak present at 1315 cm^{-1} corresponds to the D (or defect) band[26], which is absent in the Raman spectrum of pure graphite. The position, intensity (relative to the G-band) and broadening of the D band depend on the nature of impurities (dopants) and functional groups present, and the type of disorder[56]. The broad peak corresponding to the D band in our case and I_D/I_G intensity ratio greater than 1 imply structurally disordered carbon, as expected for the case of carbon obtained by pyrolysis at relatively low temperature as 1000 °C.

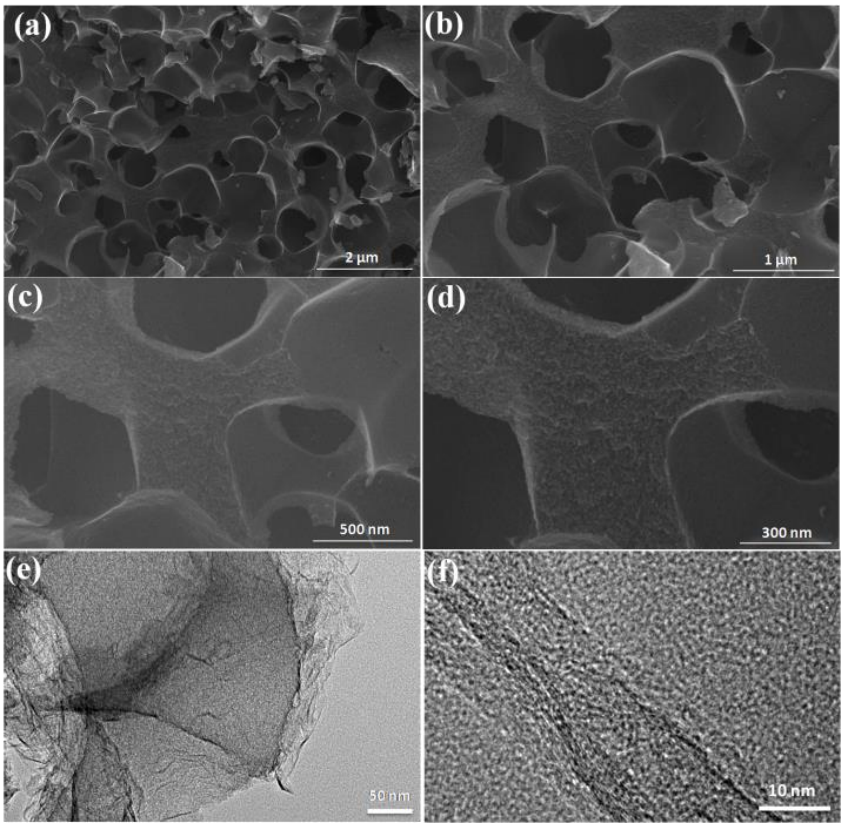

Figure 3.3 (a), (b), (c) and **(d)** FESEM images, and **(e)** and **(f)** HRTEM images of IMPC

The FESEM images shown in figure 3.3 (a-d) clearly indicate that IMPC is composed of 3D macro-pore network of interconnected micro-porous carbon sheets, a beehive type configuration. The macro-pores are developed as a result of the interconnection between the carbon sheets which is clear in Figure 3.3b and c. These macro-pores help in the diffusion process of electrolyte ions into the inner mico-pores even at higher charging rates. Figure 3.3d shows that the interconnected carbon sheets also contain micropores. The TEM image of Figure 3.3e further confirms that that the carbon sheets have high density of micropores. Graphitization in the carbon sheets was also confirmed from the HRTEM image shown in Figure 3.3f. The distorted lattice fringes are due to the incomplete graphitization as a result of the defects created by pores. The XPS of C1s and O1s spectra in Figure 3.4 clearly indicate the presence and chemical character of carbon and oxygen in IMPC. The percentage of different elements in the sample is calculated after fitting the spectra corresponding to each element. The XPS data indicate that the material contains mainly carbon with a small amount of oxygen. In fact 89% of carbon and 10% of oxygen were the values obtained from the calculation. The three peaks fitted in C1s spectrum (Figure 3.4a)

correspond to C=C (284.6 eV), C-O (286.5 eV) and C=O (289.4 eV). There are two peaks in the O1s spectrum (Figure 3.4b) positioned at 531.6 and 533.5 which correspond to C=O and O-C=O, respectively.

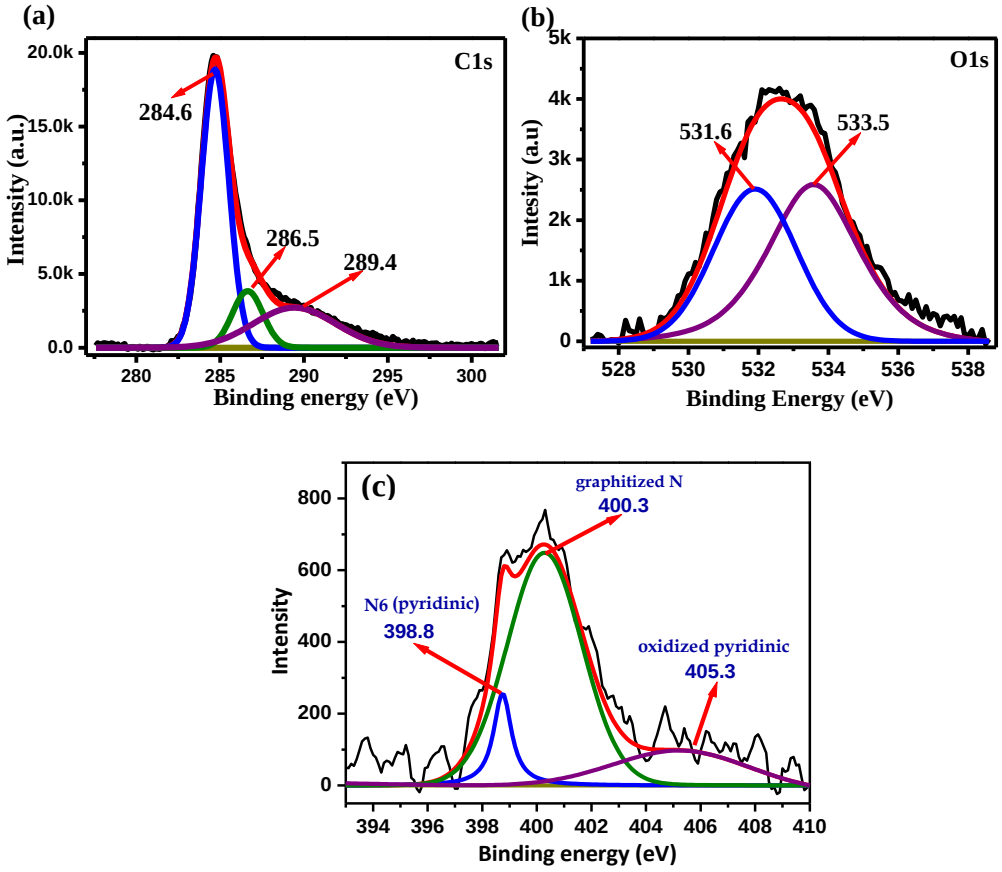

Figure 3.4 (a) C1s and **(b)** O1s and (c) N1s XPS spectra of IMPC after fitting

Sufficient amount of oxygen on the material helps for the wettability of the electrode which is important for the double layer formation. A small amount (1.9%) of nitrogen was also seen to be present in the sample which can come from the amide group in the polymer precursor. The N1s XPS contribution in the sample is presented in the figure 4c. The porous structure of IMPC was analyzed in details by N_2 gas adsorption-desorption isotherm which is shown in Figure 3.5 The type I isotherm (Figure 3.5a) indicates that the material contains mainly micropores[57]. The saturation in the isotherm at the higher pressure can be due to the large density of micropores in the material[58]. The BET specific surface area obtained from the N_2 adsorption data is 1327 m^2g^{-1} which indicates that the material is suitable as an electrode material for electrical double layer capacitors. Figure 3.5b shows the pore size distribution obtained from the N_2 adsorption- desorption. Pore density is more in the region of

less than 2nm. Most of the pores are having a pore diameter ranges form 1-2nm. It is already observed that micropores with poresize either in the range of electrolyte ions or twice the size of electrolyte ions are suitable for the electrical double layer formation[59].

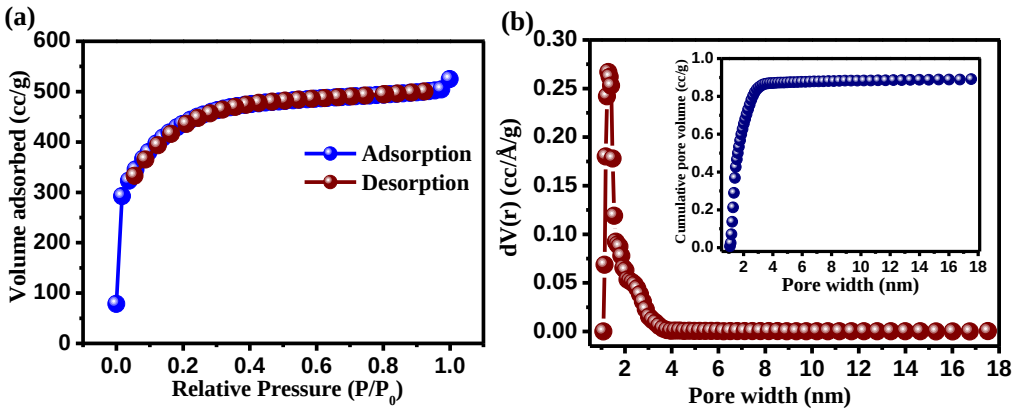

Figure 3.5 (a) N_2 adsorption-desorption isotherm and **(b)** the pore size distribution and cumulative pore volume (inset) calculated from DFT method.

A small fraction of mesopores with pore diameter ranges from 2–3 nm was also observed. From the FESEM images and the N_2 adsorption data, it is confirmed that IMPC contains small fraction of macropores and mesopores and a large micropore density. The macropores due to the interconnected sheet network and mesopores help for the fast diffusion of electrolyte ions in to the micropores for both aqueous and non-aqueous systems.

In the inset is given the pore volume distribution curve. It is clear that 80% of the pore volume is contributed by the micropores (< 2nm). From the N_2 isotherm and pore size distribution it is confirmed that the IMPC contains mostly micropores with a small amount of mesopores and macropores.

There have been some other examples of polymer pyrolysis where high surface area carbon materials have been obtained. A Comparison of some such cases is given in the Table 3.1.

Polymer Precursor	BET Specific Surface area (m^2g^{-1})	
	Without Activation	**After activation**
Poly (4-sodium styrene sulfonate-co-maleic acid) sodium salt[20]	1720	
Copolymer of polyacrylonitrile (PAN), and poly(n-butyl acrylate) (PBA)[21]	500	2570
Polypyrole[60]	-	3432
Poly(acrylic acid-co-maleic acid) sodium salt[61]	188	
Poly(o -phenylenediamine)[62]	-	591
Sulfonated Poly(styrene-co-methacrylic acid) (SPS-COOH) Sphere[63]	508	
Polypyrole[16]	-	2870
Poly(acrylamide-*co*-acrylic acid) potassium salt	1327	2366

Table 3.1 Specific surface area of carbons obtained by the pyrolysis of polymer

3.3.2 Electrochemical Measurements

3.3.2.1 Electrochemical measurements in 1M H_2SO_4

The synthesized porous carbon material was tested for both aqueous and organic supercapacitors since the energy is limited in the aqueous systems due to its lower potential window. All the aqueous measurements were done in a two electrode symmetric cell with 1M H_2SO_4 solution as electrolyte. Figure 3.6a shows the cyclic voltammogram (CV) in the aqueous electrolyte for different scan rates in the potential window 0-1V. The rectangular nature of the CV shows the double layer formation at the electrode-electrolyte interface and no redox reaction is seen to be involved. The rectangular nature at the higher scan rates is due to the presence of micropores. The solvated cation (H_3O^+) and anion (SO_4^{2-}) in H_2SO_4 solution have ion sizes 0.42 nm and 0.53 nm respectively[64, 65]. These ions can easily diffuse through the micropores with size >1 nm. Hence the material shows higher capacitance in aqueous system

even at increased charge discharge rates.

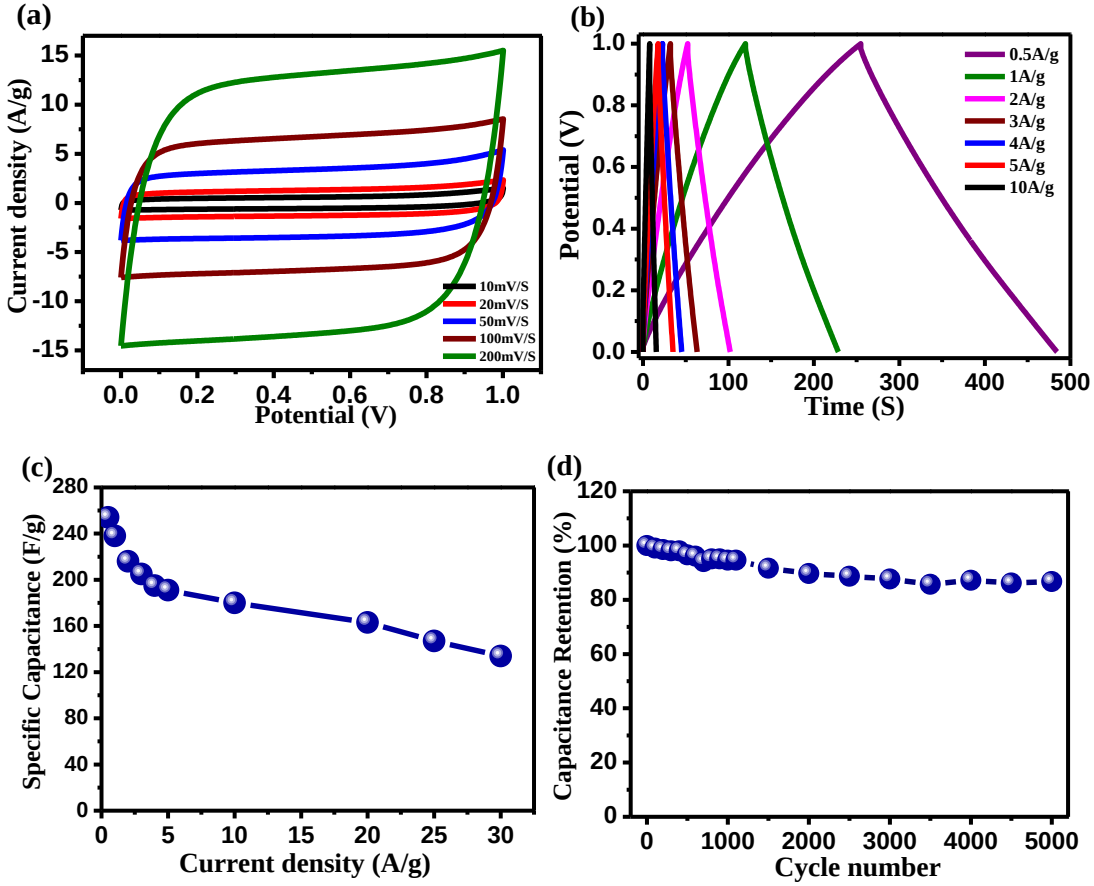

Figure 3.6 (a) Cyclic voltammogram of IMPC in 1M H_2SO_4 at different scan rates from 10 mV/s to 200 mV/s **(b)** constant current charge discharge curve and **(c)** specific capacitance calculated form charge discharge for different current densities and **(d)** cyclic stability in 1M H_2SO_4 solution.

Small distortion from rectangular nature for higher scan rate can be due to less mesopore density and the series resistance. The galvanostatic charge discharge measurements were performed for different current densities to evaluate the specific capacitance. Figure 3.6b shows the galvanostatic charge-discharge curves in the aqueous electrolyte for different charging currents. The current densities were calculated on the basis of active material loading on each electrode. The triangular nature again confirms the charge storage at the electrode- electrolyte interface by electrical double layer formation[10]. The gravimetric specific capacitance in three electrode system based on the active material loading is calculated from the charge discharge measurements for different current densities using the formula given in Eq(1)

$$C_{sp} = \frac{2I}{m\frac{dV}{dt}} \qquad \text{Eq (1)}^{66, 67}$$

Where, '$\mathbf{C_{sp}}$' is the specific capacitance in three electrode system based active material loading, '**I**' is the constant discharging current, '**dV/dt**' is the discharge slope and '**m**' is the total loading of active material on single electcrode. The observed specific capacitance for current densities from 0.5 Ag^{-1} to 30 Ag^{-1} is given in the Figure 3.6c. The material showed a maximum specific capacitance of 254 Fg^{-1} at discharge current of 0.5 Ag^{-1}. It retained a capacitance of 140 Fg^{-1} at higher a current density of 30 Ag^{-1}. It shows that 60% capacitance is retained even though the discharge rate is increased by 60 times. The cyclic stability test was done at a constant discharge current rate of 2 Ag^{-1}. 90% of initial capacitance was retained after 5,000 charge-discharge cycles as shown in Figure 3.6d. In the aqueous system the maximum potential window is limited by 1V which in fact limits the energy density of the device. In order to increase the energy the capacitance was tested in organic electrolyte also.

3.3.2.2 Electrochemical Measurements in 1M $LiPF_6$ in EC: DMC

The cyclic voltammograms for different scan rates in 1M $LiPF_6$ (organic electrolyte) in EC:DMC are given in the Figure 3.7a. The rectangular nature once again confirms charge storage by electrical double layer formation at the electrode electrolyte inteface. At higher scan rates the the rectangular nature of CV is seen to be distorted. This is due to the less density of mesopores in the material and the higher electrolyte resistance compared to aqueous system. The specific capacitance is calculated from the constant current charge-discharge mesurements for different current densities with the same method followed for aqueous system. Figure 3.7b represents the charge discharge measurements for different charging currents. The specific capacitance calculated from the charge discharge measurements for different charging rates from 0.25 Ag^{-1} to 10 Ag^{-1} is given in the Figure 3.7c. A highest specific capacitance of 138F g^{-1} is achieved at 0.25 Ag^{-1} maintaining 100 Fg^{-1}at 10 Ag^{-1} at room temperature. The specific capacitance calculated from the charge discharge measurements for different charging rates form 0.25 Ag^{-1} to 10 Ag^{-1} is given in the Figure 3.7c A highest specific capacitance of 138 Fg^{-1} is achieved at 0.25 Ag^{-1} maintaining 100 Fg^{-1} at 10 Ag^{-1} at room temperature. 72% of capacitnace was retained when the charging current is increased by 40 times. It shows 87%

capacitance retention after 3000 cycles as shown in figure 3.7d.

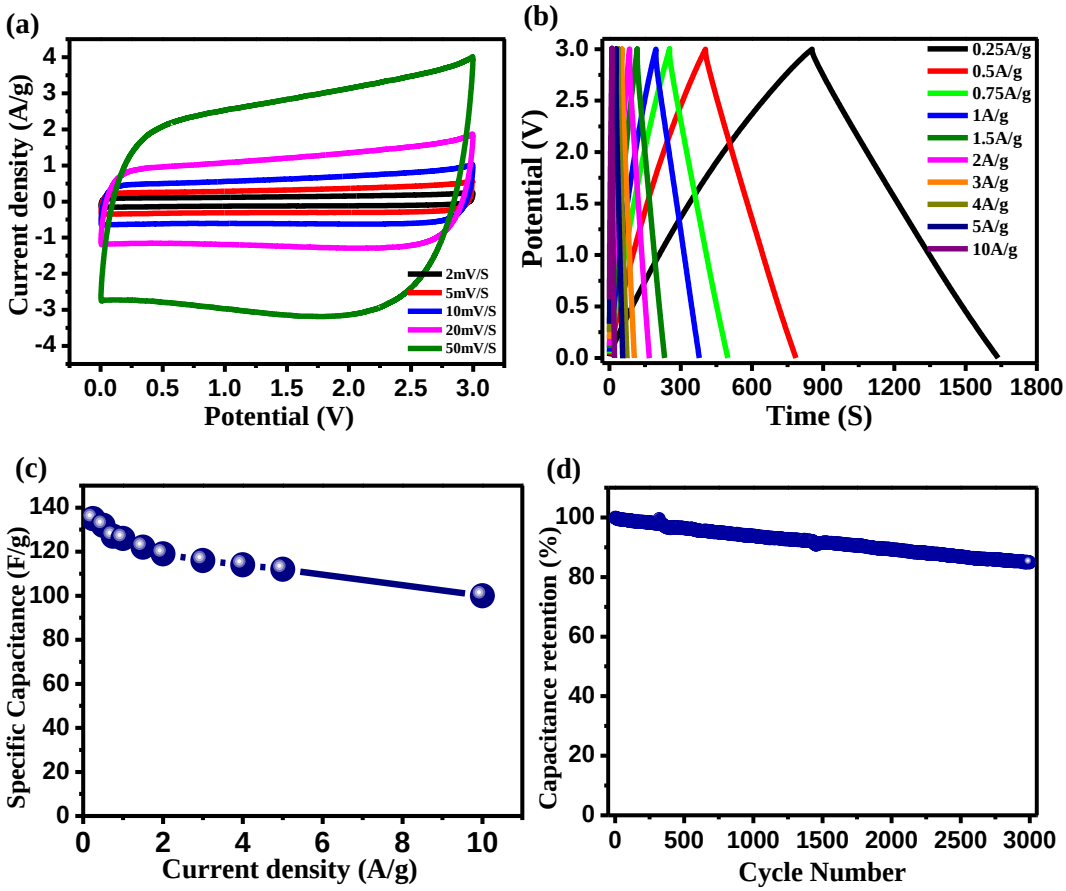

Figure 3.7 (a) Cyclic voltammogram of IMPC in 1M $LiPF_6$ in EC:DMC in different scan rates from 2 mV/S to 50 mV/S **(b)** constant current charge discharge curve, **(c)** specific capacitance calculated form charge discharge for different current densities, and **(d)** cyclic stability in 1M $LiPF_6$ in EC:DMC

The ion size of the anion (PF_6^-) and cation in $LiPF_6$ in EC:DMC is approximately 0.51nm[68, 69] and 0.7nm respectively. It has been already observed that the capacitive contribution is maximum when the pore size distribution is close to the size of the solvated ions or twice of that. [59] In our case both the cation and anion sizes are within 2 nm. IMPC also shows maximum pore density in the range of 1.1.nm to 1.5 nm which is the cause of its superior performance as an electrode material for electrical double layer capacitor. The frequency response of the capacitance for both aqueous and non-aqueous systems was also studied using the electrochemical impedance spectroscopy respectively.

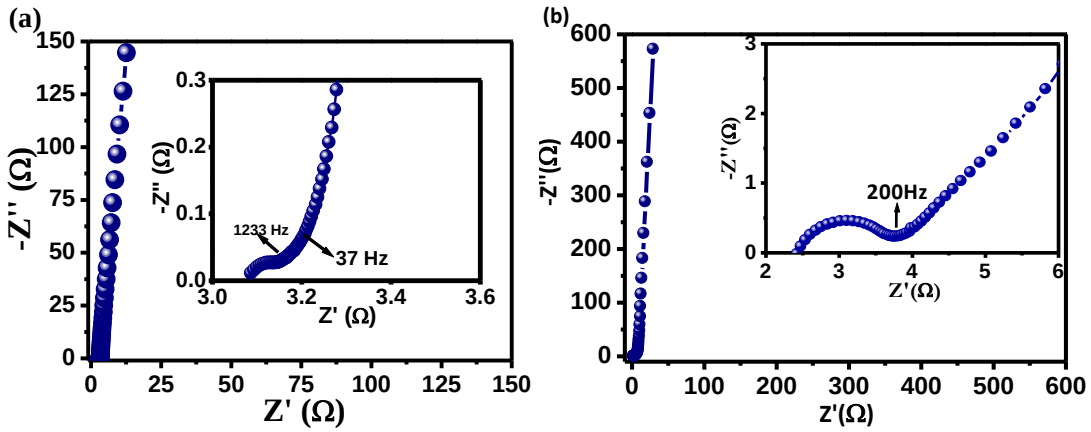

Figure 3.8 Nyquist plot for IMPC **(a)** in 1M H_2SO_4 and **(b)** in 1M $LiPF_6$ in EC:DMC. Inset shows the same in the higher frequency region.

The impedance measurements were performed in the frequency range 10 mHz-10 kHz in aqueous system and 1 mHz-100 kHz in non-aqueous medium with a signal amplitude of 10 mV. Figure 3.8a and b show the Nyquist plots for the aqueous and non-aqueous systems. The vertical nature of the Nyquist plots clearly indicates the capacitive behaviour of the material. The Nyquist plot expanded in the high frequency region is given in the inset. The x-intercept of the Nyquist plot in Figure 3.8a gives the Ohmic resistance of the circuit which is a combination of the resistance of the electrolyte, internal resistance of the active material and the substrate, and the contact resistance at the active material / current collector interface[3]. This is 3.08 Ω for the aqueous system and 2.4 Ω for the non-aqueous system. The small semicircle in the high frequency region is due to the electrical double layer formation at the electrode electrolyte interface. The equivalent series resistance is the sum of the Ohmic resistance and the charge transfer resistance. This is observed to be 3.18 Ω for the aqueous and 3.8 Ω for the non-aqueous system. The frequency, called as the onset frequency (Nyquist plot starts to go vertical) indicates the highest frequency upto which the electrodes have a capacitive behaviour[66, 70]. The inset shows that the onset frequency here is 37 Hz for aqueous and is 5 Hz for the non-aqueous system. This is comparable to the other reports on activated carbon or micro/mesoporous carbon. This happens because of difference in the cation and anion size for aqueous and organic electrolytes. Electrode material shows more capacitive nature at the lower frequency because at lower frequencies more electrolyte ions get access to maximum pore in the carbon material whereas at higher frequencies only pores at the surface of the electrode electrolyte interface get access to the electrolyte ions.

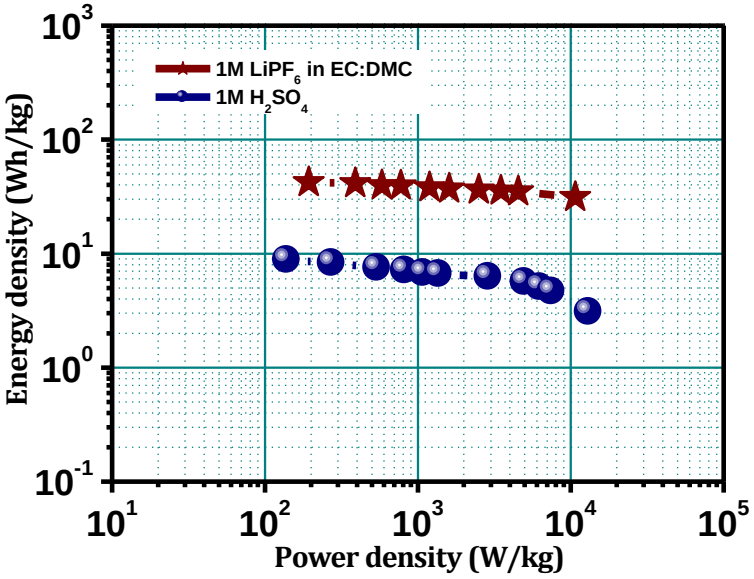

Figure 3.9 Ragone plot compares the energy density and power density of IMPC in both aqueous and non-aqueous electrolytes.

The Ragone plot shown in the figure 3.9 evaluates the performance of material in terms of its energy density and power density for both aqueous and non-aqueous supercapacitors. Energy density and power density were calculated using the formula in Eq (2) and (3)

$$E_s = \frac{C_{sp}}{8*3.6} V_{max}^2 \qquad \text{Eq (2)}^{67} \quad \text{and}$$

$$P_s = \frac{E_s}{t} \qquad \text{Eq (3)}^{67}$$

Where 'E_s' is the specific energy density, 'V_{max}' is the maximum voltage, 'P_s' is the power density and't' is total discharge time in hours from the maximum potential to zero. The material has a capability to deliver energy density of 3.1Wh kg^{-1} with a power density of 13600 W kg^{-1} where as the power density decreases to 138W kg^{-1} when the energy density is increased to 8.8Wh kg^{-1} in the aqueous medium. It is clear that the performance of the material is better in the non-aqueous case both in terms of energy density and power density. The maximum power density obtained is 11000W kg^{-1} with energy density of 32Wh kg^{-1}. The gravimetric and volumetric energy density and power density for the total device in the case of the non-aqueous system were also calculated. The Ragone plots comparing the corresponding values for the total cell and the active material are given in the figure 3.10a and b respectively.

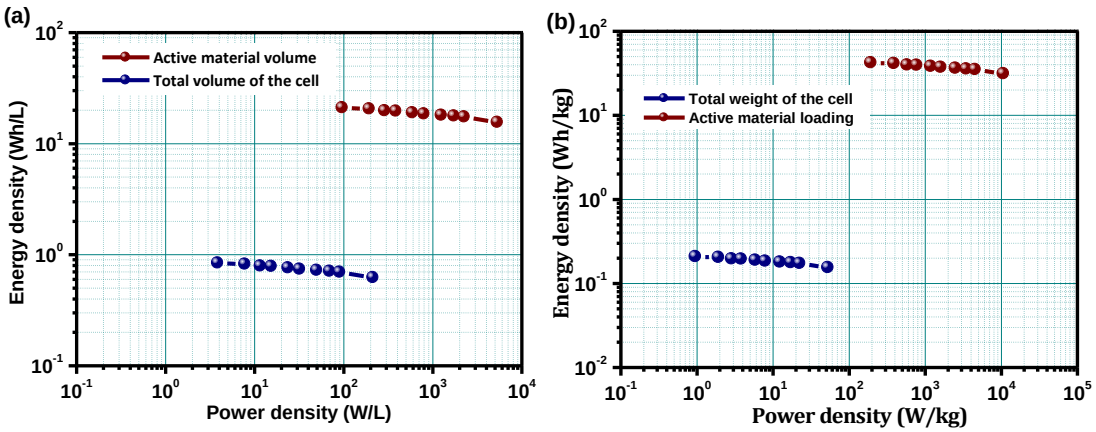

Figure 3.10 Ragone plot of (a) volumetric energy density and power density based on active material volume and the cell volume; and (b) gravimetric energy density and power density based on total active material loading and total weight of the cell

The Ragone plot given in the Figure 3.11a compares the energy density and power density of IMPC electrode based on active material loading in a two electrode system with the other carbon materials synthesised from polymer pyrolysis[20, 21, 62, 63, 71]. It is clear that IMPC performs much better both in terms its energy density and power density in the aqueous as well as non-aqueous systems. The power density in 1M H_2SO_4 is significantly higher than other polymer derived carbons. Zhu et al[62] have reported highest energy density of 11Wh kg^{-1} in the aqueous system as compared to other polymer derived carbons including IMPC. However, the power density at this high energy density and the highest power density obtained are considerably less compared to our sample IMPC. The evaluation of IMPC in terms of its energy density and power density with other carbon based materials in the non-aqueous (organic electrolyte as well as ionic liquids) system is presented in the Figure 3.11b[67, 72-74]. The carbon materials include CNT, hydrothermal carbons, AC, graphene etc. In the non-aqueous electrolyte also, IMPC shows either higher or comparable performance with other reports. Lu et al[73] have reported energy density higher than IMPC with maximum potential window 4V in ionic liquid. The power density obtained is comparable to that of IMPC. The well defined morphology of IMPC which includes macropores as well as micropores results in its observed excellent performance as a supercapacitor electrode.

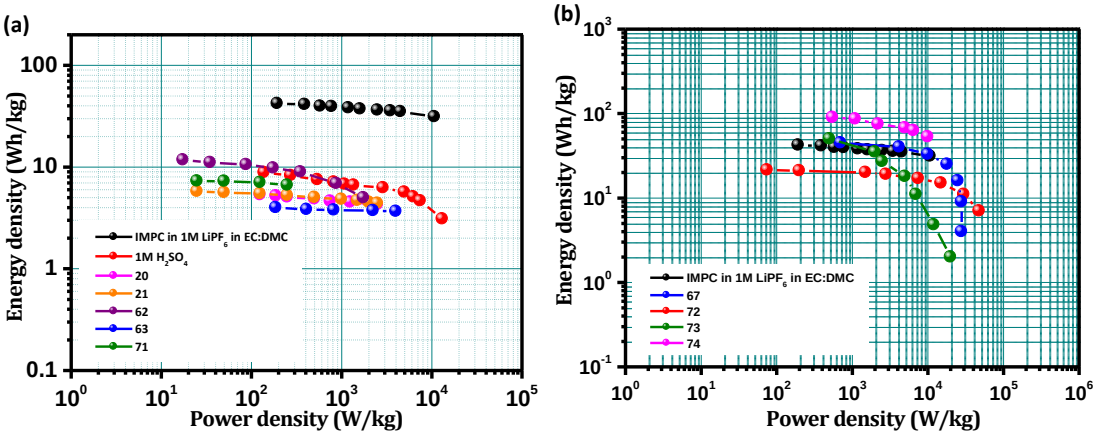

Figure 3.11 Ragone plots comparing the energy density and power density of IMPC **(a)** with other polymer derived carbons and **(b)** in the non aqueous system with other reports on the same for different carbon structures.

As stated earlier, we also examined the effect of adding an activation agent (KOH) to the polymer (1:1wt.%) before pyrolysis to explore the possibility of further enhancing the surface area and possibly the capacitance. The carbon sample thus obtained is named as IMPC-A.

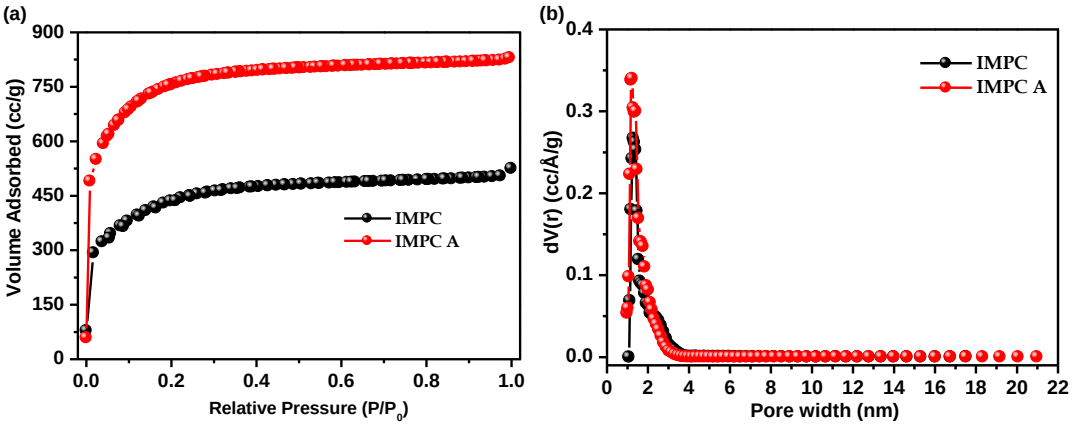

Figure 3.12 (a) Isotherms and (b) pore size distribution curves of IMPC and IMPC Activated (IMPC A)

The BET specific surface area obtained from N_2 gas adsorption desorption studies on this sample was 2366 m^2g^{-1} which is significantly higher than that (1327 m^2g^{-1}) for IMPC (i.e. carbon obtained without KOH addition). The N_2 adsorption desorption isotherms and pore size distributions for IMPC and IMPC-A are shown in the figure 3.12. From the pore size distribution curve it is clear that the density of micropores is enhanced after activation, but there are no other discernible modifications. The electrochemical performance of IMPC-A in 1M H_2SO_4 was studied using

galvanostatic charge discharge measurement at various current densities. The galvanostatic charge-discharge and variation of capacitance with current density are shown in figure 3.13.

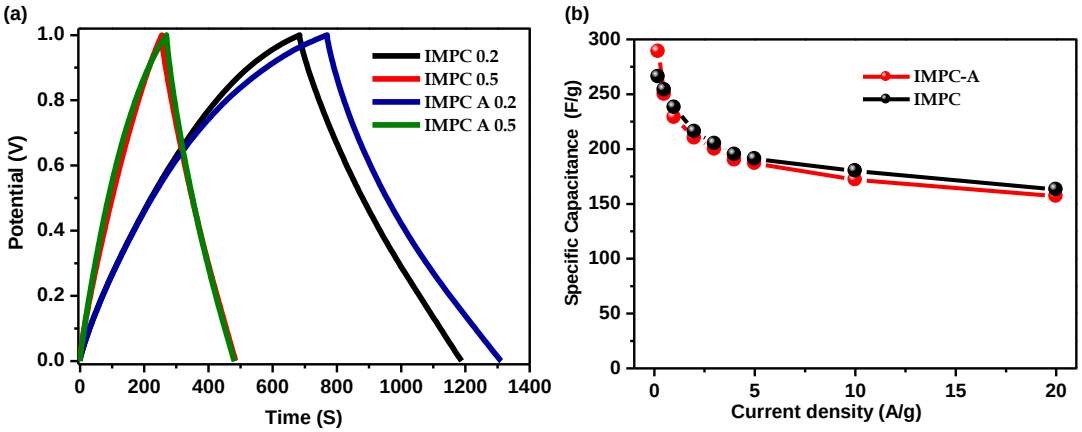

Figure 3.13 (a) Galvanostatic charge discharge at low current densities and **(b)** Specific capacitance calculated form charge discharge of IMPC and IMPC Activated (IMPC-A).

IMPC-A showed an enhancement in the specific capacitance at lower discharge rate whereas it did not show increase in specific capacitance at higher current densities. This may be due to the fact that IMPC-A has higher micropore density than that of IMPC whereas the ratio of mesopores to micropores is higher for IMPC. Thus at low charging rates more inner pores will be accessible for the solvated electrolyte ions, yielding higher capacitance. But at higher current densities, due to less mesopore density and large diffusion length, the accessible surface area for electrolyte ions is less as compared to the case of lower current density. Increase in the resistance due to increased defects and oxygen content after activation is also a hindrance to the capacitance enhancement. The XPS spectra of IMPC-A is shown in the figure 3.14 and the percentage of elements obtained from XPS is listed in table 3.2. It is clear that the oxygen content has increased after activation.

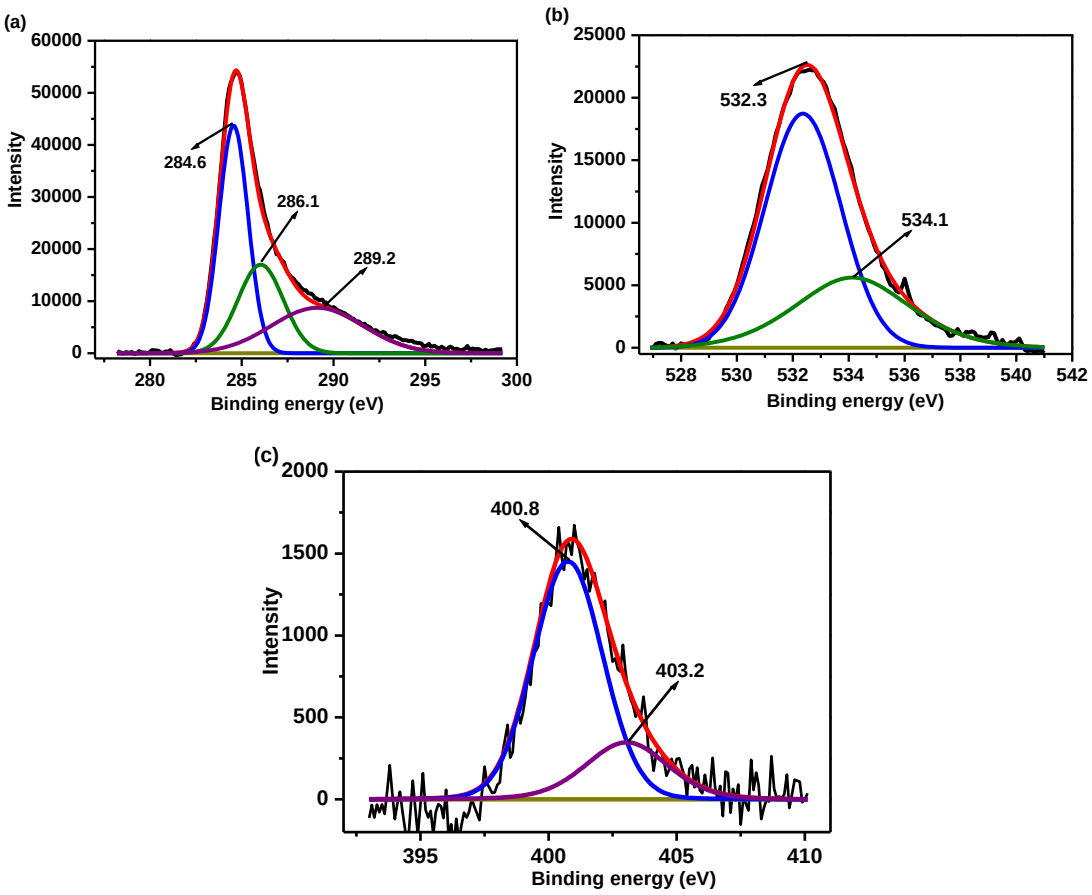

Figure 3.14 (a) C1s, **(b)** O1s and **(c)** N1s XPS spectra of IMPC-A

	C %	N %	O %	Surface area (m^{2g-1})
IMPC	89.2	1.9	9.9	1327
IMPC-A	83.3	1.6	15.1	2366

Table 3.2 Amount of different elements and specific surface area of IMPC and IMPC-A

Briefly, it was noted that there is a significant enhancement in the surface area with increase in the micropore density. The capacitance was also seen to increase but primarily at lower discharge rates.

3.3.2.3 Li-ion Hybrid Electrochemical Capacitor (Li-HEC)

A good performance of both, the anode ($Li_4Ti_5O_{12}$) and the cathode (IMPC), in a single electrode configuration is essential to balance the mass loading between the electrodes in Li-HEC assembly. In order to ensure this, Li-insertion properties of commercially available spinel phase $Li_4Ti_5O_{12}$ were evaluated in a single electrode

configuration between 1-3 V *vs.* Li at a current density of 100 mAg^{-1}. The galvanostatic charge discharge and cyclic stability data of $Li_4Ti_5O_{12}$ in the half cell configuration are shown in Figure 15a and 15b respectively.

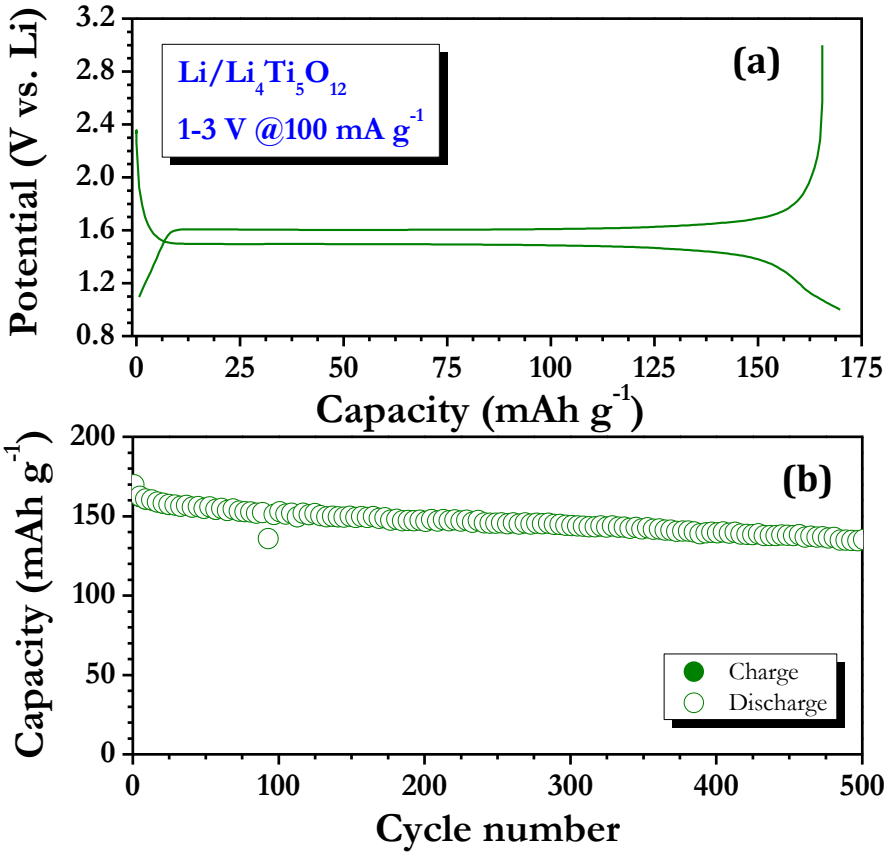

Figure 3.15 (a) Galvanostatic charge-discharge curves of $Li/Li_4Ti_5O_{12}$ (Aldrich, USA) half-cells cycled between 1-3 V at constant current density of 100 mAg^{-1}, and **(b)** Plot of discharge capacity *vs.* cycle number. The data points were collected after every 4 cycles.

Similar to the insertion type anode, the IMPC cathode was also tested in a single electrode configuration between 3-4.6 V *vs.* Li at a current density of 100mA g^{-1} and the corresponding results are presented in figure 3.16. For comparison, commercially available AC (hereafter abbreviated as CAC with a BET surface area 817 m^2g^{-1}, Norit, Netherlands) was also tested under similar conditions and plotted along with IMPC. The upper cut-off potential is fixed by considering the decomposition potential of conventional carbonate based electrolytes (~4.6 V *vs.* Li)[75].

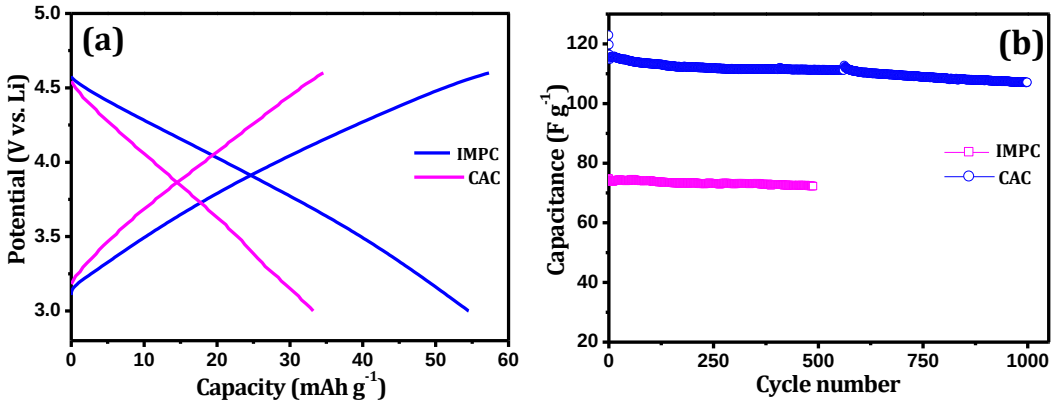

Figure 3.16 (a) Typical galvanostatic charge-discharge curves of high surface area porous carbon (IMPC) in single electrode configuration (half-cell) along with commercially available activated carbon (CAC) tested between 3-4.6 V *vs.* Li, in which metallic lithium acts as both counter and reference electrode, **(b)** Plot of specific discharge capacitance *vs.* cycle number. The data points were collected after every 10 cycles

Figure 3.16a represents the typical charge-discharge curves for IMPC and CAC. The linear variation of voltage with respect to time (capacity) clearly suggests the formation of electric double layer across the electrode/electrolyte interface *i.e.* anion double layer formation (PF_6^-)[24]. The test cells delivered the initial discharge capacity of ~54 and ~33 $mAhg^{-1}$ for IMPC and CAC, respectively. This clearly showed IMPC exhibits > 1.5 times higher reversibility than CAC which is mainly due to the presence of interconnected network carbon with the presence of micropores[20]. The interconnected network provides for facile electron transfer during the accumulation of charge carriers over the micropores. As a result enhanced reversibility is noted for IMPC. The observed capacity is converted into specific capacitance according to the following relation:

$$C\,(F\,g^{-1}) = \frac{i\,(A)\times t\,(s)}{3600\times m\,(g)} = X\,(mAh\ \ g^{-1})\times\frac{3600}{dV(mV)}$$

where, *i* is applied current, *t* is discharge time, *m* weight of the active material, X is observed capacity in mAh g^{-1} and *dV* is the testing window of the aforementioned cell in a single electrode configuration (mV, 1600 mV). However, the mentioned relation is valid only for the linear variation of voltage *vs.* time[24]. Accordingly, specific discharge capacitance of ~123 Fg^{-1} was observed for IMPC as compared to ~75 Fg^{-1} for the CAC case. A small drop in the capacitance is noted in the initial cycles and

thereafter IMPC showed very stable cycling behavior which is retained at ~92% after 1000 cycles (calculated from 3rd cycle onwards) and is shown in figure 3.16b. The IMPC is noted to deliver excellent performance in single electrode configuration, hence similar kind of profiles are anticipated in Li-HEC assembly. Based on the single electrode performance of both electrodes under the same current density (100 mAg^{-1}), the mass loading between anode to cathode ratio was adjusted to 1:3.15 (4 mg: 12.6 mg).

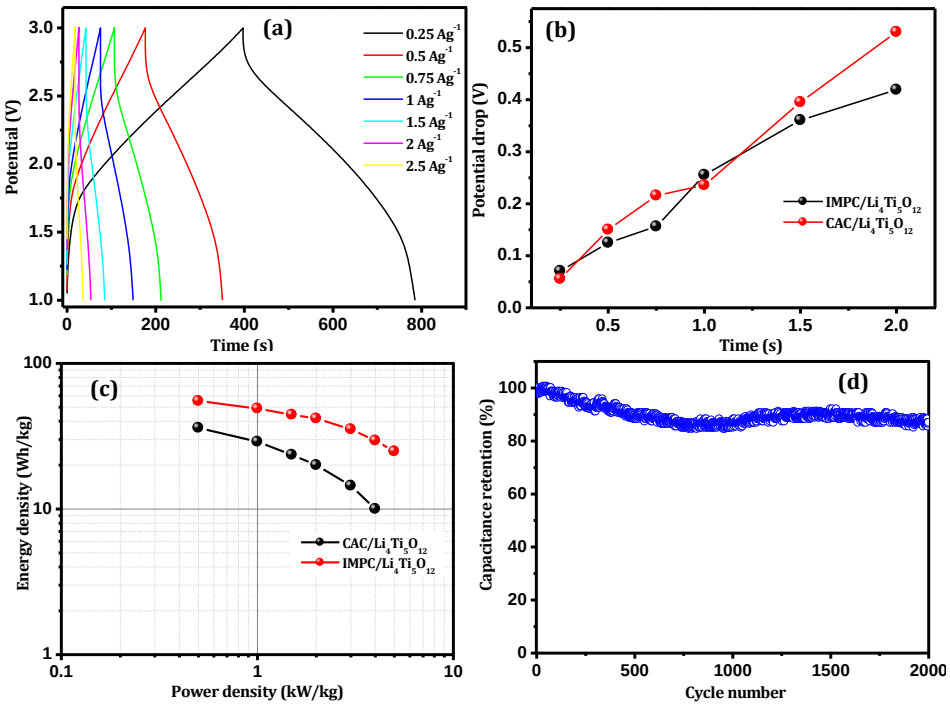

Figure 3.17 (a) Galvanostatic charge-discharge curves of Li-HEC (IMPC/$Li_4Ti_5O_{12}$) at various applied current densities, **(b)** Ohmic drop of Li-HEC configurations, **(c)** Ragone plot two different Li-HEC assembly, and **(d)** cycling profiles of IMPC/$Li_4Ti_5O_{12}$ Li-HEC. The data points were collected after every 25 cycles.

Electrochemical profiles of Li-HEC were studied between 1-3 V at various current densities and the corresponding results are presented in figure 3.17. Here, the applied current is calculated based on the total mass loading of the electrodes (16.6 mg), for example 16.6mA applied to Li-HEC at current density of 1 Ag^{-1}.

Figure 3.17a shows the typical charge-discharge profiles of IMPC/$Li_4Ti_5O_{12}$ Li-HEC. The reaction mechanism of Li-HEC is described as follows. During the charge process the Li-ions present in the electrolyte intercalate into the spinel lattice ($Li_4Ti_5O_{12}$) faradaically, whereas in order to maintain the charge neutrality in the

electrolyte solution anions simultaneously undergo double layer formation (anion double layer) with IMPC (non-Faradaic reaction)[24, 25, 34]. The aforesaid reaction is reversed during the subsequent discharge process. The salient features of the discharge curve in Li-HEC comprises of three important regions like Ohmic drop (IR drop), monotonous curve region and sudden drop. The Ohmic drop is mainly associated with the resistance offered by active material and the monotonous region belongs to Li-extraction from the spinel lattice and simultaneous de-sorption of PF_6^- anions from IMPC electrode[34]. As expected, increasing the current density leads to a decrease in discharge time, which is mainly due to the partial involvement of electro-active material[76]. In other words, surface of the active material only participates in the electrochemical reaction *i.e.* there is no sufficient time for Li-intercalation into the spinel lattice[37].

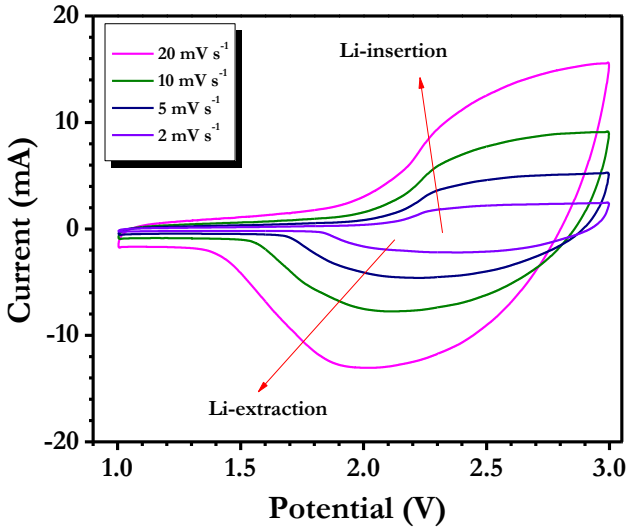

Figure 3.18 Typical CV traces of Li-HEC composed of IMPC as cathode and spinel $Li_4Ti_5O_{12}$ as anode

Cyclic voltammetry (CV) was also performed to validate the reaction mechanism and the data are illustrated in figure 3.18. It is evident from the CV profiles that above/below 1.5 V a drastic increase/decrease in current response is noted which indicates that the Li-insertion/extraction in to/from spinel lattice. Similarly, a prominent current response is noted during both anodic and cathodic scans which indicate the formation of electric double layer across the carbonaceous cathode and electrolyte interface. The observed CV traces are consistent with the previous report on coconut shell derived AC reported by Jain *et al.*[77]

The IR drop of IMPC/$Li_4Ti_5O_{12}$ Li-HEC system was derived from the galvanostatic

cycling profile and compared with CAC/$Li_4Ti_5O_{12}$ Li-HEC and the comparison is given in figure 3.17b. It is obvious to notice that, no difference was noted between both systems at low current rates; whereas IMPC/$Li_4Ti_5O_{12}$ Li-HEC offered very low resistance at high currents as compared to CAC/$Li_4Ti_5O_{12}$ Li-HEC (Figure 3.19b).

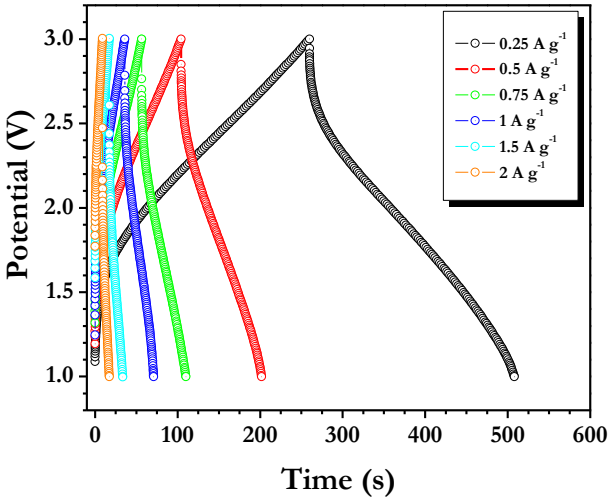

Figure 3.19 Galvanostatic charge-discharge profiles of commercially available activated carbon (CAC)/ $Li_4Ti_5O_{12}$ Li-HEC tested between 1-3 V at various current densities.

The lower resistance of IMPC based system is mainly attributed to the interconnected yet ion-accessible network of 3D architecture, which translates into a facile electron transfer to external circuit during high current operation. As a result, high power capability is expected for IMPC/$Li_4Ti_5O_{12}$ Li-HEC. The specific energy (E_{SP}) and power densities (P_{SP}) are calculated using the following relation, $P_{SP} = (E \cdot i / M)$ and $E_{SP} = (P_{SP} \cdot t)$, where $E = (E_{max} + E_{min})/2$, E_{max} and E_{min} are the potential at beginning and end of discharge curves during galvanostatic measurements, respectively. M is the total mass of both the electrodes (16.6 mg)[34, 37-39, 44].

The IMPC based Li-HEC delivered the energy density of ~55 Wh kg^{-1} which is much higher (~1.5 times) than that by the CAC based system (~36 Wh kg^{-1}) (Figure 3.17c). IMPC/$Li_4Ti_5O_{12}$ Li-HEC delivered an exceptional performance even at high currents. For example, energy density of ~29 and ~10Wh kg^{-1} was noted for IMPC and CAC based Li-HEC, respectively.

Cyclability is an important pre-requisite for practical Li-HEC configuration and hence the cycling profiles of IMPC/$Li_4Ti_5O_{12}$ Li-HEC were carried out at a current density of 2 Ag^{-1} and shown in figure 3.17d. The IMPC/$Li_4Ti_5O_{12}$ Li-HEC rendered ~87% of initial value after 2000 cycles. The small fading mainly originated from the intrinsic

nature of the commercially available insertion type anode, $Li_4Ti_5O_{12}$ (Figure 3.15b). However, such fading issue can be alleviated by adopting carbon coating over $Li_4Ti_5O_{12}$ particulates or making carbon composites [26-29, 31].

It is further important to point out that the IMPC not only outperformed the CAC based system but also the rest of the systems investigated with various insertion type anodes (figure 3.20) and the graphene based systems reported by Stoller *et al.*[43] (40.8 Wh kg^{-1}) and some of us (45 Wh kg^{-1}) earlier as well [44].

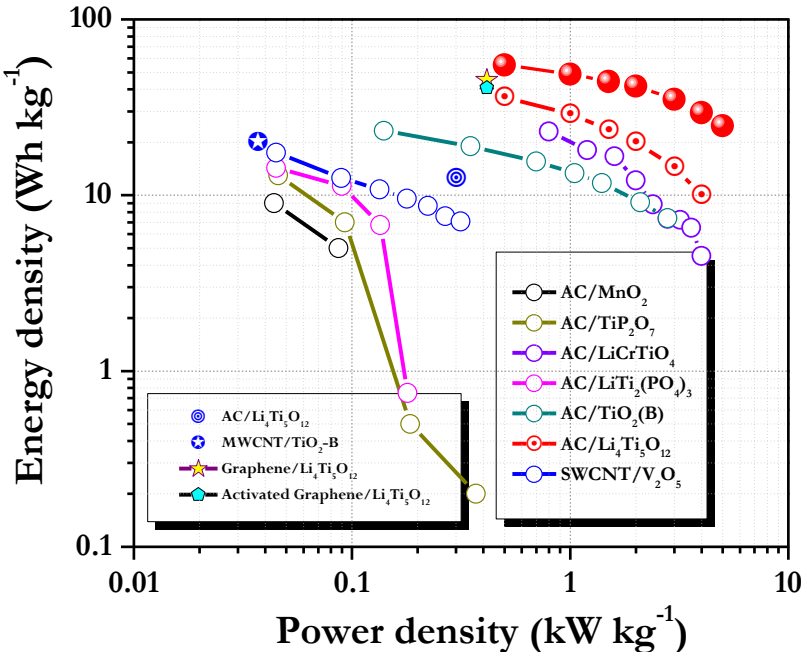

Figure 3.20 Ragone plot indicates the performance of various insertion type anode materials tested for Li-HEC applications in non-aqueous medium. Spheres indicates the present work (IMPC/$Li_4Ti_5O_{12}$ Li-HEC)

Finally, It is worth mentioning that the observed energy densities are much higher than the values required to drive HEV (~7.5-8.3 Whkg^{-1}), but still further enhancements are required to drive PHEV (~57-97 Whkg^{-1}) and EV (min. 150 Wh kg^{-1})[23]. Further studies are in progress to improve the cycleability and enhancing the energy density as well.

3. 4 Conclusion

3D interconnected microporous sheet-like carbon was synthesised by carbonization of a selected polymer Poly(acrylamide-*co*-acrylic acid) potassium salt by a single step pyrolysis without any activation. The synthesized material (named IMPC) showed a

BET specific surface area of 1327 m^2g^{-1}. The material performance was evaluated for the supercapacitor electrode for both the aqueous and non-aqueous electrolytes. It showed remarkable performance in both the aqueous and non-aqueous systems. It showed a capacitance of 255 Fg^{-1} current density of 0.5 Ag^{-1} and retained 140 Fg^{-1} at the highest current density of 30 Ag^{-1} in 1M H_2SO_4. In the non-aqueous system 30% capacitance was retained when the current was increased from 0.25 Ag^{-1} (138 Fg^{-1}) to 10 Ag^{-1} (100 Fg^{-1}). This indicates that IMPC is able to deliver higher energy while maintaining its high power density which is clear from the Ragone plot. Electrochemical impedance spectroscopy was also performed to evaluate the capacitive nature of the material in both aqueous and non aqueous system.

A high energy density Li-ion hybrid electrochemical capacitor (Li-HEC) was also fabricated using IMPC as cathode and commercial $Li_4Ti_5O_{12}$ as anode. The Li-HEC delivered maximum energy density of ~55 $Whkg^{-1}$ which is ~1.5 higher than that achievable by commercial activated carbon based configuration. Apart from the high energy density, porous carbon based Li-HEC was also capable of delivering high power density.

3.5 References

1. X. Chen, C. Li, M. Gratzel, R. Kostecki and S. S. Mao, *Chem. Soc. Rev.*, 2012, **41**, 7909-7937.
2. A. S. Arico, P. Bruce, B. Scrosati, J. M. Tarascon and W. Van Schalkwijk, *Nature Mater.*, 2005, **4**, 366-377.
3. J. Zhang and X. S. Zhao, *Chemsuschem*, 2012, **5**, 818-841.
4. M. D. Stoller and R. S. Ruoff, *Energy Environ. Sci.*, 2010, **3**, 1294-1301.
5. P. Simon and Y. Gogotsi, *Nature Mater.*, 2008, **7**, 845-854.
6. J. R. Miller and P. Simon, *Science*, 2008, **321**, 651-652.
7. Y. Zhai, Y. Dou, D. Zhao, P. F. Fulvio, R. T. Mayes and S. Dai, *Adv. Mater.*, 2011, **23**, 4828-4850.
8. M. D. Stoller, S. Park, Y. Zhu, J. An and R. S. Ruoff, *Nano Lett.*, 2008, **8**, 3498-3502.
9. H. Jiang, P. S. Lee and C. Li, *Energy Environ. Sci.*, 2013, **6**, 41-53.
10. L. L. Zhang and X. S. Zhao, *Chem. Soc. Rev.*, 2009, **38**, 2520-2531.
11. D. Mhamane, A. Suryawanshi, S. M. Unni, C. Rode, S. Kurungot and S. Ogale, *Small*, 2013, n/a-n/a.

12. B. Liu, H. Shioyama, T. Akita and Q. Xu, *J. Am. Chem. Soc.*, 2008, **130**, 5390-5391.
13. J. Hu, H. Wang, Q. Gao and H. Guo, *Carbon*, 2010, **48**, 3599-3606.
14. Y. Gogotsi, R. K. Dash, G. Yushin, T. Yildirim, G. Laudisio and J. E. Fischer, *J. Am. Chem. Soc.*, 2005, **127**, 16006-16007.
15. D.-D. Zhou, Y.-J. Du, Y.-F. Song, Y.-G. Wang, C.-X. Wang and Y.-Y. Xia, *J Mater Chem A*, 2013, **1**, 1192-1200.
16. L. Qie, W. Chen, H. Xu, X. Xiong, Y. Jiang, F. Zou, X. Hu, Y. Xin, Z. Zhang and Y. Huang, *Energy Environ. Sci.*, 2013, **6**, 2497-2504.
17. D. Hines, A. Bagreev and T. J. Bandosz, *Langmuir*, 2004, **20**, 3388-3397.
18. J. Lee, S. Han and T. Hyeon, *J. Mater. Chem.*, 2004, **14**, 478-486.
19. S. Han, K. Sohn and T. Hyeon, *Chem. Mater.*, 2000, **12**, 3337-3341.
20. P. Yadav, A. Banerjee, S. Unni, J. Jog, S. Kurungot and S. Ogale, *Chemsuschem*, 2012, **5**, 2159-2164.
21. M. Zhong, E. K. Kim, J. P. McGann, S.-E. Chun, J. F. Whitacre, M. Jaroniec, K. Matyjaszewski and T. Kowalewski, *J. Am. Chem. Soc.*, 2012, **134**, 14846-14857.
22. V. Aravindan, J. Gnanaraj, Y.-S. Lee and S. Madhavi, *Journal of Materials Chemistry A*, 2013, **1**, 3518-3539.
23. E. J. Cairns and P. Albertus, *Annual Review of Chemical and Biomolecular Engineering*, 2010, **1**, 299-320.
24. G. G. Amatucci, F. Badway, A. Du Pasquier and T. Zheng, *Journal of The Electrochemical Society*, 2001, **148**, A930-A939.
25. I. Plitz, A. DuPasquier, F. Badway, J. Gural, N. Pereira, A. Gmitter and G. G. Amatucci, *Applied Physics A: Materials Science & Processing*, 2006, **82**, 615-626.
26. K. Naoi and Y. Nagano, in *Supercapacitors*, Wiley-VCH Verlag GmbH & Co. KGaA, 2013, pp. 239-256.
27. K. Naoi, S. Ishimoto, Y. Isobe and S. Aoyagi, *Journal of Power Sources*, 2010, **195**, 6250-6254.
28. K. Naoi, *Fuel Cells*, 2010, **10**, 825-833.
29. K. Naoi, S. Ishimoto, J.-i. Miyamoto and W. Naoi, *Energy & Environmental Science*, 2012, **5**, 9363-9373.
30. K. Naoi and P. Simon, *Electrochemical Society Interface*, 2008, **17**, 34-37.

31. K. Naoi, W. Naoi, S. Aoyagi, J.-i. Miyamoto and T. Kamino, *Accounts of Chemical Research*, 2013, **46**, 1075-1083.
32. T. Brousse, D. Bélanger and D. Guay, in *Supercapacitors*, Wiley-VCH Verlag GmbH & Co. KGaA, 2013, pp. 257-288.
33. H. Kim, M.-Y. Cho, M.-H. Kim, K.-Y. Park, H. Gwon, Y. Lee, K. C. Roh and K. Kang, *Advanced Energy Materials*, 2013, **3**, 1500-1506.
34. V. Aravindan, N. Shubha, W. C. Ling and S. Madhavi, *Journal of Materials Chemistry A*, 2013, **1**, 6145-6151.
35. Q. Wang, Z. Wen and J. Li, *Advanced Functional Materials*, 2006, **16**, 2141-2146.
36. C. V. Rao and B. Rambabu, *Solid State Ionics*, 2010, **181**, 839-843.
37. V. Aravindan, W. Chuiling and S. Madhavi, *Journal of Materials Chemistry*, 2012, **22**, 16026-16031.
38. V. Aravindan, W. Chuiling, M. V. Reddy, G. V. S. Rao, B. V. R. Chowdari and S. Madhavi, *Physical Chemistry Chemical Physics*, 2012, **14**, 5808-5814.
39. V. Aravindan, M. V. Reddy, S. Madhavi, S. G. Mhaisalkar, G. V. Subba Rao and B. V. R. Chowdari, *Journal of Power Sources*, 2011, **196**, 8850-8854.
40. L. Cheng, H. Q. Li and Y. Y. Xia, *Journal of Solid State Electrochemistry*, 2006, **10**, 405-410.
41. V. Aravindan, M. V. Reddy, S. Madhavi, G. V. S. Rao and B. V. R. Chowdari, *Nanoscience and Nanotechnology Letters*, 2012, **4**, 724-728.
42. Z. Yang, D. Choi, S. Kerisit, K. M. Rosso, D. Wang, J. Zhang, G. Graff and J. Liu, *Journal of Power Sources*, 2009, **192**, 588-598.
43. M. D. Stoller, S. Murali, N. Quarles, Y. Zhu, J. R. Potts, X. Zhu, H.-W. Ha and R. S. Ruoff, *Physical Chemistry Chemical Physics*, 2012, **14**, 3388-3391.
44. V. Aravindan, D. Mhamane, W. C. Ling, S. Ogale and S. Madhavi, *ChemSusChem*, 2013, **6**, 2240-2244.
45. O. A. Vargas C, A. Caballero and J. Morales, *Nanoscale*, 2012, **4**, 2083-2092.
46. D. Upare, S. Yoon and C. Lee, *Korean Journal of Chemical Engineering*, 2011, **28**, 731-743.
47. C. Vix-Guterl, E. Frackowiak, K. Jurewicz, M. Friebe, J. Parmentier and F. Béguin, *Carbon*, 2005, **43**, 1293-1302.
48. L. Wei and G. Yushin, *Nano Energy*, 2012, **1**, 552-565.

49. D. Puthusseri, V. Aravindan, S. Madhavi and S. Ogale, *Energy & Environmental Science*, 2014, **7**, 728-735.
50. K. Putyera, T. J. Bandosz, J. Jagieo and J. A. Schwarz, *Carbon*, 1996, **34**, 1559-1567.
51. S.-S. Tzeng and J.-H. Pan, *Mater. Chem. Phys.*, 2002, **74**, 214-221.
52. Y. Wang, F. Su, C. D. Wood, J. Y. Lee and X. S. Zhao, *Industrial & Engineering Chemistry Research*, 2008, **47**, 2294-2300.
53. Y. Zhu, S. Murali, M. D. Stoller, K. J. Ganesh, W. Cai, P. J. Ferreira, A. Pirkle, R. M. Wallace, K. A. Cychosz, M. Thommes, D. Su, E. A. Stach and R. S. Ruoff, *Science*, 2011, **332**, 1537-1541.
54. A. Kajdos, A. Kvit, F. Jones, J. Jagiello and G. Yushin, *J. Am. Chem. Soc.*, 2010, **132**, 3252-3253.
55. A. C. Ferrari and D. M. Basko, *Nature Nanotechnology*, 2013, **8**, 235-246.
56. Y. Korenblit, M. Rose, E. Kockrick, L. Borchardt, A. Kvit, S. Kaskel and G. Yushin, *ACS Nano*, 2010, **4**, 1337-1344.
57. W. Chaikittisilp, M. Hu, H. Wang, H.-S. Huang, T. Fujita, K. C. W. Wu, L.-C. Chen, Y. Yamauchi and K. Ariga, *Chem. Commun.*, 2012, **48**, 7259-7261.
58. Y. S. Yun, S. Y. Cho, J. Shim, B. H. Kim, S.-J. Chang, S. J. Baek, Y. S. Huh, Y. Tak, Y. W. Park, S. Park and H.-J. Jin, *Adv. Mater.*, 2013, **25**, 1993-1998.
59. J. Chmiola, G. Yushin, Y. Gogotsi, C. Portet, P. Simon and P. L. Taberna, *Science*, 2006, **313**, 1760-1763.
60. L. Wei, M. Sevilla, A. B. Fuertes, R. Mokaya and G. Yushin, *Adv. Funct. Mater.*, 2012, **22**, 827-834.
61. P. Yadav, S. Warule, J. Jog and S. Ogale, *Solid State Commun.*, 2012, **152**, 2092-2095.
62. H. Zhu, X. L. Wang, X. X. Liu and X. R. Yang, *Adv. Mater.*, 2012, **24**, 6524-6529.
63. J.-S. Lee, S.-I. Kim, J.-C. Yoon and J.-H. Jang, *ACS Nano*, 2013.
64. M. Endo, T. Maeda, T. Takeda, Y. J. Kim, K. Koshiba, H. Hara and M. S. Dresselhaus, *J. Electrochem. Soc.*, 2001, **148**, A910-A914.
65. L. Eliad, G. Salitra, A. Soffer and D. Aurbach, *The Journal of Physical Chemistry B*, 2001, **105**, 6880-6887.
66. P. L. Taberna, P. Simon and J. F. Fauvarque, *J. Electrochem. Soc.*, 2003, **150**, A292-A300.

67. H. Wang, Z. Xu, A. Kohandehghan, Z. Li, K. Cui, X. Tan, T. J. Stephenson, C. K. King'ondu, C. M. B. Holt, B. C. Olsen, J. K. Tak, D. Harfield, A. O. Anyia and D. Mitlin, *ACS Nano*, 2013, **7**, 5131-5141.

68. G. Feng, R. Qiao, J. Huang, S. Dai, B. G. Sumpter and V. Meunier, *Phys. Chem. Chem. Phys.*, 2011, **13**, 1152-1161.

69. A. Berthod, J. J. Kozak, J. L. Anderson, J. Ding and D. W. Armstrong, *Theor. Chem. Acc.*, 2007, **117**, 127-135.

70. C. S. Du and N. Pan, *Nanotechnology*, 2006, **17**, 5314-5318.

71. X. Yang, D. Wu, X. Chen and R. Fu, *J.Phys.Chem.C*, 2010, **114**, 8581-8586.

72. Z. Xu, Z. Li, C. M. B. Holt, X. Tan, H. Wang, B. S. Amirkhiz, T. Stephenson and D. Mitlin, *The Journal of Physical Chemistry Letters*, 2012, **3**, 2928-2933.

73. W. Lu, R. Hartman, L. Qu and L. Dai, *The Journal of Physical Chemistry Letters*, 2011, **2**, 655-660.

74. C. Liu, Z. Yu, D. Neff, A. Zhamu and B. Z. Jang, *Nano Lett.*, 2010, **10**, 4863-4868.

75. V. Aravindan, J. Gnanaraj, S. Madhavi and H.-K. Liu, *Chemistry – A European Journal*, 2011, **17**, 14326-14346.

76. K. Zaghib, J. B. Goodenough, A. Mauger and C. Julien, *Journal of Power Sources*, 2009, **194**, 1021-1023.

77. A. Jain, V. Aravindan, S. Jayaraman, P. S. Kumar, R. Balasubramanian, S. Ramakrishna, S. Madhavi and M. Srinivasan, *Scientific reports*, 2013, **3**.

Chapter 4

From waste paper basket to solid state and Li-HEC ultracapacitor electrodes: A value added journey for shredded office paper

Hydrothermal processing followed by controlled pyrolysis of waste (used) white office paper (a globally collectable shredded paper waste) was performed to obtain high surface area carbon with hierarchical pore size distribution. Such waste paper derived carbon (WPC) shows remarkable performance in all solid-state supercapacitor fabricated with ionic liquid-polymer gel electrolyte. The Li-ion electrochemical capacitor constructed using WPC as cathode also shows an excellent energy storage capacity of 61 $Whkg^{-1}$.

4.1 Introduction

Development of renewable, clean, green and sustainable energy systems has gained significant attention during the past decade due to the growing realization of the serious hazards of conventional polluting fuels for environment and health. Since energy conversion and utilization are not necessarily concurrent events, efficient and durable energy storage deserves as important a consideration as the energy conversion from renewable sources.[1-3] The energy density and the power density of any charge storage system represent the key qualifiers for its potential usability in a specific application domain.

Electrical double layer capacitors (EDLCs) are considered to be one of the most promising energy storage technologies for the future because of their specific advantages of higher power capability and long cyclic stability over other storage devices.[4] Different forms of carbon based materials have been used as the electrode materials for EDLCs[5]. These include high surface area activated carbon and different carbon nanostructures such as carbon nanotubes, carbon nano fibers, graphene etc[6, 7] amongst the various carbon forms employed, the highest capacitance has been obtained for porous activated carbons.[8, 9] Different precursors and methods have been employed to synthesize such high surface area porous carbons. These include carbonization of carbonaceous materials in the presence of activation agents in inert atmosphere, direct carbonization of polymer salts without adding external activation agent(s), use of hard templates to create pores in carbon etc.[10-12] Porous networks such as metal organic frameworks (MOFs) have also been explored as precursor to get porous carbon.[13] Moreover, natural products have been explored as a cost effective alternatives to develop ultracapacitor or supercapacitor electrodes.[14]

Li-ion hybrid capacitors (Li-HEC), known as the third generation capacitors, are also considered to be promising devices for electrical energy storage, as they lie between the Li-ion battery and supercapacitor quality factors on the Ragone plot which has energy density and power density as its axes.[15, 16] The charge storage mechanism in Li-HEC involves both the double layer formation and Li interaction. In such a system, high surface area carbon is used for the EDLC electrode (cathode) and $Li_4Ti_5O_{12}$ as the Li intercalation electrode (anode).

In addition to the quality of materials, engineering of the device architecture is also very important for practical applications. Leakage of the electrolyte and related safety issue is recognized as the major disadvantage of liquid electrolyte based supercapacitors.[17] Replacing the liquid electrolyte with a solid or gel system without degrading the performance is a promising option to overcome this hurdle. Towards this end both aqueous and ionic liquid based gel electrolytes have been explored with different electrode materials. Carbon based materials are the preferred electrode materials for ionic liquid based devices because of their higher potential stability in such media, as there is no reaction involved while charging and discharging. Different forms of carbons have been explored in such designs.

Here we demonstrate the synthesis of functional carbon synthesized from the waste office paper (shredded printed paper), a large amount of global collectable waste, as the source of the functional carbon material for supercapacitor and Li-HEC applications. As shown, the peculiar interconnected morphology realized in our synthesized material shows a significant enhancement in charge storage performance as compared to commercial activated carbon. There is one previous study on making carbon using waste newspaper, however their surface area was quite low (416 m^2g^{-1}) as compared to that obtained in our case (2341 m^2g^{-1}), as discussed later.[18] Correspondingly, at a scan rate of 25 mVs^{-1} they have reported a specific capacitance of 95 Fg^{-1} in aqueous electrolyte (charge-discharge data not reported), whereas we have obtained 216 Fg^{-1} even at a higher scan rate of 50 mVs^{-1}. From a charge discharge study we have obtained 286 Fg^{-1} at 0.5 Ag^{-1}, as shown below. It is important to mention that in our work we have also examined our material in ionic liquid gel electrolyte (solid state supercapacitor) and for Li-hybrid electrochemical capacitor application and impressive results are obtained. In another study, card board box waste has been used to make carbon. A specific capacitance of 203 Fg^{-1} is reported in aqueous electrolyte at a discharge rate of 5 $mAcm^{-2}$(no loading information is provided).[19]

4.2 Experimental Section

4.2.1 Synthesis of Waste Paper derived carbon (WPC): The waste office papers (standard A4 size white papers with some printed matter thereupon) were used as the

precursor for the synthesis of the hierarchically porous carbon material. The material was synthesized by a two step process involving hydrothermal treatment followed by high temperature pyrolysis. The papers were used without any pre-processing. Briefly, two used printed papers with nominal text content cut into small pieces and these pieces along with 100ml of 1M H_2SO_4 were transferred to a teflon-lined steel autoclave and kept at 180°C for 24 hrs. After allowing the system to cool down to room temperature naturally, the hydrothermal product was washed with D.I water and dried at 100°C for 12h. The dried product was mixed with KOH in the 1:2 mass ratios prior to pyrolysis. The mixture was carbonized in an alumina tube furnace at the temperature 800°C for 4 h under continuous Argon flow. The furnace was allowed to cool to room temperature naturally. The product obtained after activation was washed with 2M HCl to remove the inorganic impurities. After washing with D.I water the product was dried under vacuum at 90°C.

4.2.2 Material Characterization:PAN Analytical powder X-ray diffractometer with nickel-filtered Cu K_α radiation was used to perform the powder X-ray diffraction analysis. Raman spectroscopy was performed using the LabRAM HR800 from JY Horiba system. The SEM images were taken using FEI Nova Nano FESEM. The system FEI, Tecnai F30, FEG with 300 kV was used for HRTEM imaging and analysis. N_2 gas adsorption-desorption measurements were performed using Quadrasorb automatic volumetric instrument at 77K.

4.2.3 Preparation of EMIM BF_4-PVD FHFP Gel electrolyte: DMF and the ionic liquid (1-Ethyl-3-methylimidazolium tetrafluoroborate) were distilled prior to use to remove the moisture therein. P(VDF-HFP) was used as-received. The $EMIMBF_4$-P(VDF-HFP) gel was prepared as follows. 600 mg P(VDF-HFP) was dissolved in 6g DMF. After the P(VDF-HFP) completely dissolved, 1.8 mg $EMIMBF_4$ was added to the solution and kept at 140°C until it formed a uniform mixture. DMF was evaporated to get a uniform viscous gel of $EMIMBF_4$ and P(VDF-HFP).

4.2.4 Preparation of electrode and the solid state supercapacitor:80% of active material, 15% conducting carbon (Super P) and 5% binder (Kynar) were mixed in NMP to get a uniform slurry. The slurry was then coated onto a conducting carbon paper and kept for drying at 100°C for 24 h. PVA-H_2SO_4 gel electrolyte was used to fabricate the aqueous solid state supercapacitor. The gel electrolyte was spread onto

the dried electrodes uniformly and kept for drying. After drying, the two electrodes were sandwiched with a ionic conducting separator in between. In order to prepare the non-aqueous solid state supercapacitor, the dried electrodes were transferred to Argon filled glove box. The ionic liquid gel was spread onto two electrodes to get a uniform coating of electrolyte. Both the electrodes were then kept for drying on a hot plate to evaporate the DMF further. The two electrodes were then sandwiched with a separator in between.

4.2.5 Measurement of solid state supercapacitor: All the measurements were done at room temperature. Cyclic voltammogram, Galvanostatic charge discharge and electrochemical impedance spectroscopy measurements were performed on Biologic electrochemical work station using the software EC Lab. The gravimetric specific capacitance for a single electrode was calculated from the galvanostatic charge discharge using the formula,

$$C = \frac{2I}{m(dV/dt)} \quad (1)$$

where I is the discharge current, m is the active material loading on each electrode and dV/dt is the discharge slop. The material specific energy density (E_s) and power density (P_s) were calculated according to

$$E_s = \frac{CV^2}{8*3.6} \quad (2)$$

and

$$P_s = \frac{E_s}{t} \quad (3)$$

where V is the discharge voltage, and t is the total discharge time.

4**.2.6 Preparation and measurements of Li ion hybrid capacitor:**The electrode was prepared with 4 mg of active material (WPC or $Li_4Ti_5O_{12}$), 0.75 mg of conductive additive (Super P) and teflonized acetylene black (TAB-2) using ethanol. The film was pressed over 200 mm^2 area stainless steel mesh (Goodfellow, UK). Half-cell assembly (single electrode configuration) measurement was performed using the composite electrode and lithium, in which lithium acts as both the counter and the reference electrode. The working and reference electrodes were separated by microporous glass fiber separator (Whatman, Cat. No. 1825-047, UK) and filled with 1 M $LiPF_6$ in ethylene carbonate (EC)/diethyl carbonate (DEC) (Selectipure LP30,

Merck KGaA, Germany) electrolyte solution. For the fabrication of the Li-HEC, insertion type spinel $Li_4Ti_5O_{12}$ anode was procured from Sigma-Aldrich. Galvanostatic cycling profile measurements were performed using Arbin battery tester at various current densities.

The capacity can be converted into specific capacitance using the equation (4) [16]

$$C(Fg^{-1}) = \frac{i(A)\times t(S)}{3600 \times m(g)} = mAhg^{-1} \times \frac{3600}{dV\ (mV)} \qquad (4)$$

where, *i* is the applied current, *t* is the discharge time, *m* is the weight of the active material and *dV* is the testing potential window of the single electrode configuration (mV, 1600 mV). The energy density and power density of the Li-ion hybrid capacitor are calculated using Equation 2 and 3 respectively.

$$P_{sp} = \frac{E\times I}{M} \qquad (5)$$

And

$$E_{sp} = P_{sp} \times t \qquad (6)$$

where, E_{sp} and P_{sp} are the gravimetric energy and power density, *E* is the average potential, *M* is the total active material loading on both electrodes, and *t* is the discharge time.

4.3 Results and Discussions

4.3.1 Synthesis and Characterizations of Waste Paper derived Carbon (WPC)

Scheme 4.1 describes the simple protocol used for the synthesis of carbon from used white paper which icludes hydrothermal treatment followed by carbonization in the inert atmosphere. The hydrothermal carbonization not only helps in introducing the aromatic rings but also to remove other impurities present in the precursor.[20] This high pressure treatment also results in partial carbonization (C=C) of the precursor. A blackish brown product was obtained after the hydrothermal treatment. Further carbonization was done to increase the degree of graphitization and hence the conductivity of the material. KOH was employed to introduce the right porosity in the material.

Scheme4.1 Schematic representing the synthesis protocol for carbon from waste paper (WPC).

Figure 4.1 shows the XRD and Raman spectra of WPC. The broad peak in the XRD pattern (figure 4.1a) positioned around 22.3° is close to the (002) plane of graphite, albeit with a significant shift towards lower 2θ, which indicates partial graphitization, as expected for pyrolysis at a low temperature of 1000°C. Such interesting carbon material has small nanoscale graphitic units which are assembled in a topologically disordered manner and it is termed as turbostratic carbon.

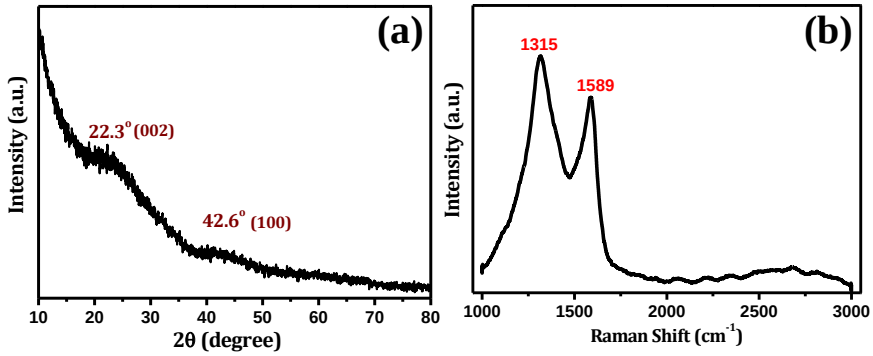

Figure 4.1. (a) Powder X-ray diffraction (XRD) pattern and (b) Raman spectrum of WPC

Turbostratic carbon is amorphous carbon with graphitization in short range order which is also known as disordered graphite.[21, 22] The increase in the intensity at low diffraction angle is due to the large pore density in the carbon which is observed after KOH activation.[23]Raman spectroscopy further confirms the partial graphitization of carbon.[24] The broad peak appearing around 1589 cm^{-1} corresponds to the G band which arises due to the in-plane vibration of sp^2carbons.[25] The peak corresponding to the D band, positioned around 1315 cm^{-1} (which is absent in pure graphite), arises due to the defects and disorder present in carbon.

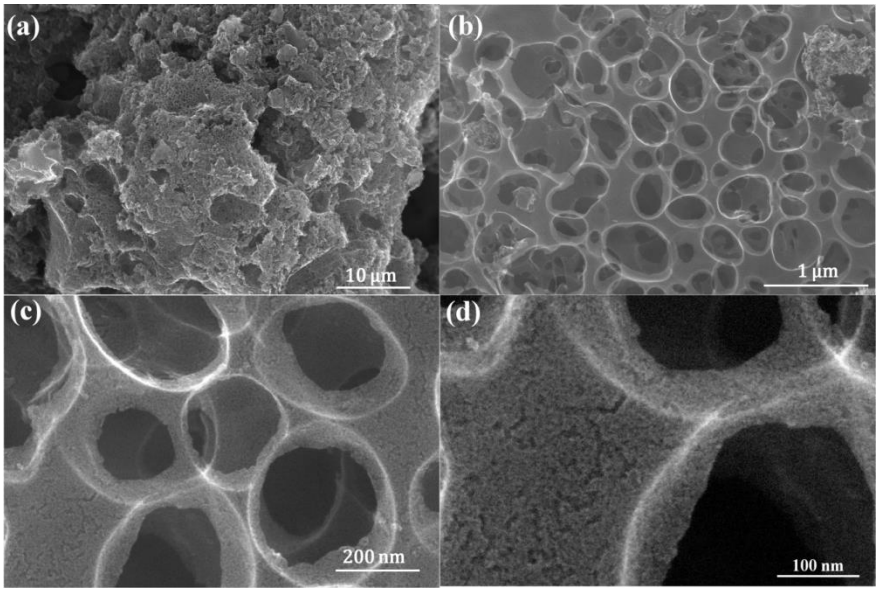

Figure 4.2 (a-d) FESEM images of WPC at different magnifications

The FESEM images given in figure 4.2 (a-d) show interconnected porous structure of WPC. These also clearly reveal hierarchical porosity with the presence of different (micro, meso and macro) types of pores in the material. Such hierarchical pore size distribution clearly helps with its applicability as an electrode for supercapacitors.

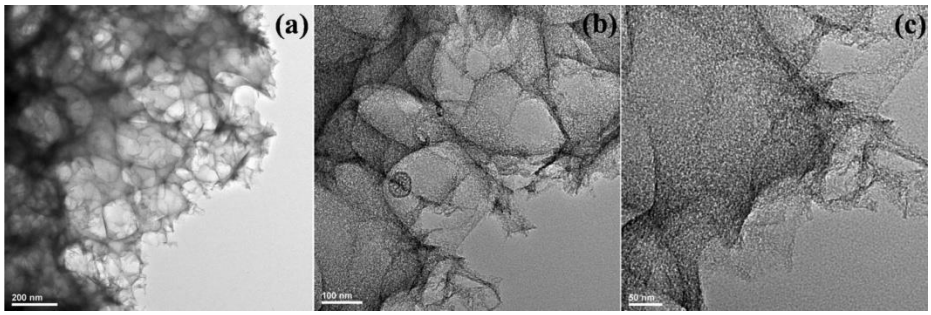

Figure 4.3 (a-c) TEM images of WPC at different magnifications

The TEM images shown in the figure 4.3 (a-c) also demonstrate the three dimensionally interconnected porous morphology with different types of pores including micropores as well as macropores. This type of 3D porous interconnected morphology is particularly useful for solid state supercapacitors because it offers channels for the fast diffusion electrolyte into the inner layers of electrode, which enhances the active surface area accessible for charge storage.[26]

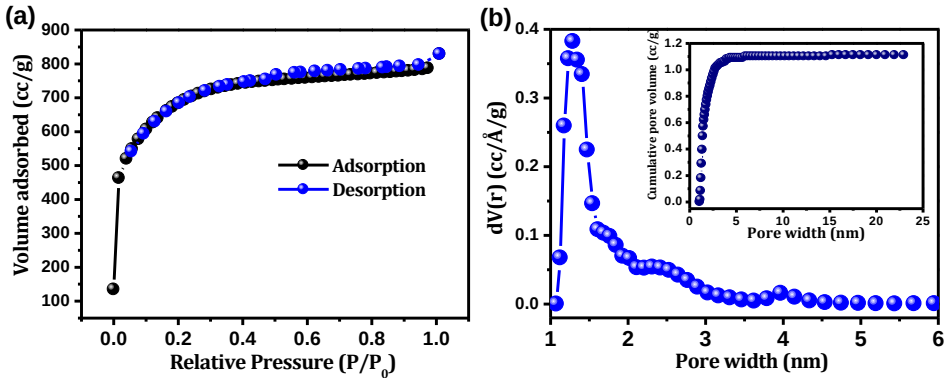

Figure 4.4 (a) N_2 adsorption-desorption isotherm of WPC, **(b)** Pore size distribution of WPC calculated from the adsorption isotherm using DFT. In the inset shows the cumulative pore volume obtained from N_2 adsorption isotherm.

In order to further understand the pore size details, N_2 gas adsorption-desorption measurements were performed. The single point BET specific surface area obtained was high, namely 2341 m^2g^{-1}. The N_2 adsorption-desorption isotherms shown in the figure 4.4a indicates that different types of pores are present in the material. The hysteresis present in the adsorption and desorption indicates that it is a type IV isotherm which arises due to the presence of mesopores therein.[27] The pore size distribution obtained from the N_2 adsorption-desorption measurements by DFT method is shown in figure 4b. It exhibits that both micropores and mesopores are present in the material. The total pore volume obtained in this case 1.1 cm^3g^{-1}. The pore density was maximum for the pore size around 1.2 nm.

The pore volume data shown in the inset of the figure 4.4b clearly indicates that the major contribution to the pore volume comes from the micropores. Indeed, 70% of the pore volume is only due to the micropores present, the rest being from the mesopore contribution. The size of the mesopores is in the range from 2-3 nm, which is also very important for a supercapacitor device.[28]

4.3.2 Electrochemical Measurements

4.3.2.1 Solid State Supercapacitor

The charge storage capacity of our carbon material was initially tested in 1M H_2SO_4 solution. The measurement details are given in the supporting information figure 4.5 (a-c). The maximum specific capacitance obtained from the charge

dischargemeasurement was 286 Fg^{-1}at 0.5 Ag^{-1} (figure 4.5e). In order to understand the charge storage capacity of WPC in the solid state architecture, PVA-H_2SO_4 gel was used as the electrolyte. The electrochemical measurement details are provided in the supplementary information figure 4.5 (e-f).

The cyclic voltammograms for WPC in 1M H_2SO_4 and PVA-H_2SO_4 gel electrolytes at different scan rates are shown in the Figure 5a and b. The observed nature of the CV curves in both the systems clearly indicates that the charge storage occurs through the double layer

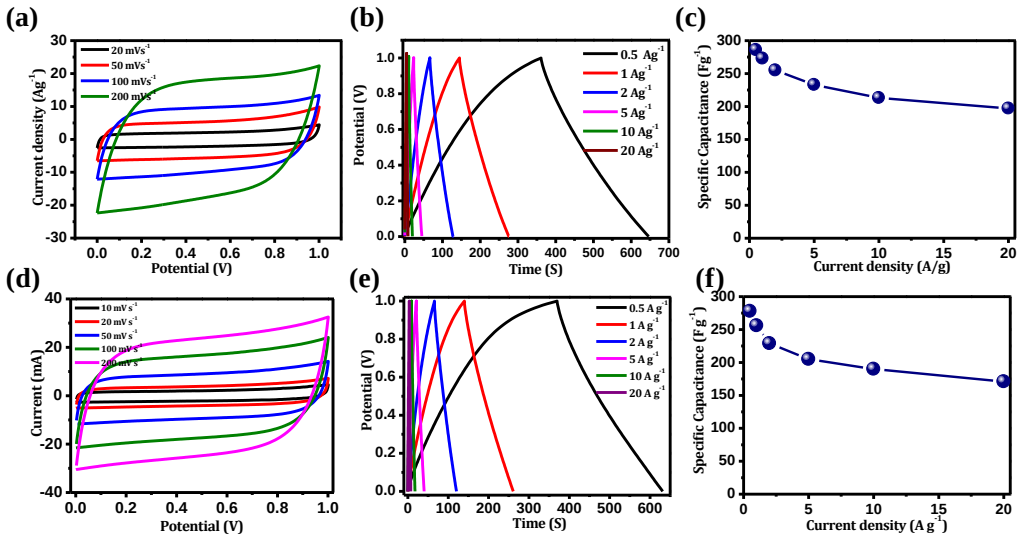

Figure 4.5 (a and d) Cyclic voltammogram, **(b and e)** charge discharge and **(c and f)** of the WPC with 1M H_2SO_4 solution and PVA-H_2SO_4 gel as electrolytes respectively.

in both cases. The specific capacitance obtained for both cases are approximately the same at the same discharge current density (see figure 4.5e and f). This proves that the interconnected porous structure of the carbon material here helps in the diffusion of electrolyte ions even in the gel form and hence the material is able to deliver equal performance for solid as well as liquid electrolytes. The charge storage capacity of the electrode generally decreases as we go from liquid based supercapacitors to solid state supercapacitors. However, interestingly there is no much decrease in the capacitance in our case. This is due to the interconnected porous structure of the material and the presence of three different types of pores. The micropores act as the active sites for the double layer formation, whereas the mesopores and macropores act as the channels for the penetration of the gel electrolyte into the inner layers of the

electrode material. In the case of WPC, the pore density is maximum in the pore size range of 1-3 nm. Since this pore size matches fairly well with the size of the solvated ions a high specific capacitance is expected, as observed.

As the operating potential and hence the energy density is lower in aqueous systems due to its limited potential window, ionic liquids with higher potential stability have been used as the electrolyte to achieve higher energy density. Therefore, our material was also tested for its performance in non-aqueous solid state supercapacitor. The non-aqueous solid state supercapacitor was fabricated with ionic liquid based gel electrolyte $EMIMBF_4$. All the electrochemical characterizations such as the cyclic voltammogram, galvanostatic charge discharge and electrochemical impedance spectroscopy were performed.

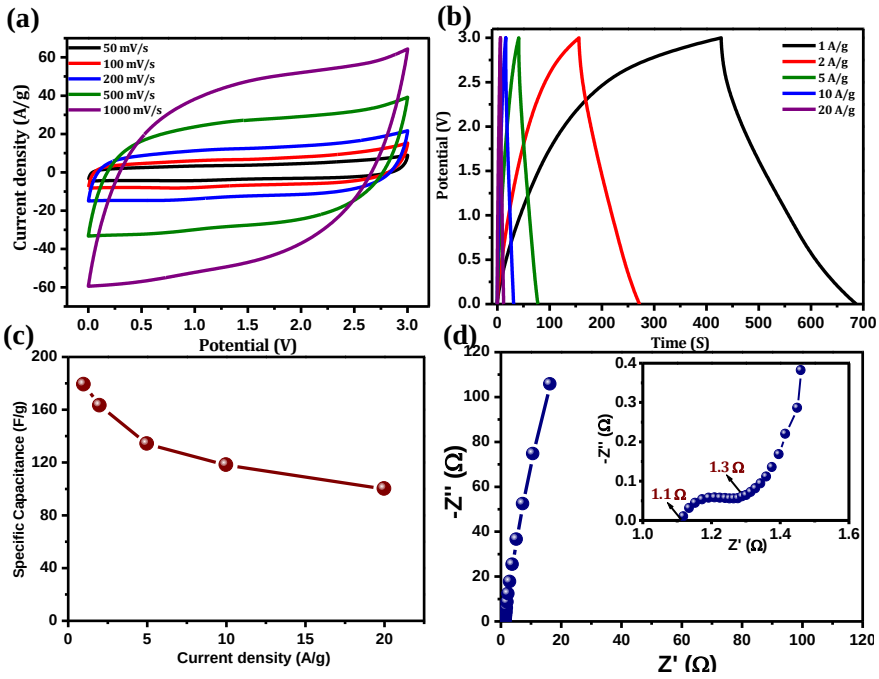

Figure 4.6 (a) Cyclic voltammograms of the solid state supercapacitor at different scan rates in the potential window 0-3V, **(b)** Galvanostatic charge-discharge at different discharge current densities, **(c)** Gravimetric specific capacitance obtained for WPC in the ionic liquid solid state supercapacitor for different discharge rates, and **(d)** Nyquist plot of the device.

The cyclic voltammograms recorded for the solid device at different scan rates in the potential window 0-3V are shown in the figure 4.6a. The cyclic voltammograms at different scan rates clearly show double layer formation characteristics corresponding

to the adsorption of electrolyte ions on the electrode electrolyte interface. The sequential increase in the charging and discharging currents with increase in the scan rate confirms the excellent capacitance retention which was also confirmed from the galvanostatic charge discharge measurements by varying the charge discharge rates. The corresponding results are shown in figure 4.6b. The specific capacitance obtained for WPC from the charge discharge measurements is given in figure 4.6c. The highest specific capacitance obtained is 179 Fg^{-1} at 1 Ag^{-1} with capacitance retention of 60% even when the discharge rate was increased to a high value of 20 Ag^{-1}. This is comparable with other ionic liquid gel based solid state supercapacitors (see Table 4.1) and is far superior in performance to other waste derived carbons.

Electrochemical impedance spectroscopy is another important tool to evaluate any electrochemical charge storage device. The Nyquist plot shown in figure 4.6d has the impedance curve going nearly parallel to –Z'' axis which is close to the case of an ideal capacitor. The x-intercept of the Nyquist plot gives the total series resistance, which plays a very important role at higher charge-discharge rates. This depends on the intrinsic resistance of the current collector, electrode material and the electrolyte. The total series resistance observed in this case was ~1.1Ω. The inset of figure 4.5d shows the high frequency part of the Nyquist plot. A total ESR of 1.3Ω was obtained for the device which includes the total series resistance as well as the charge transfer resistance. This is superior to other non-aqueous solid state supercapacitors fabricated with waste derived carbon. The open macroporous structure along with micro and mesopores make WPC an ideal candidate as an active material for solid state supercapacitor.

4.3.2.2 Li-ion Hybrid Electrochemical Capacitors (Li-HEC)

As stated earlier, high surface area carbons are also employed as cathode material for the new generation capacitors called Li-ion hybrid capacitor.[29,30] WPC, which showed excellent performance in solid state supercapacitor, was therefore also tested as a cathode material for Li-HEC.

Both the cathode and anode materials were tested independently to understand the mass loading required for cathode and anode to achieve the charge balance on both the electrodes. Commercial $Li_4Ti_5O_{12}$ (LTO) and WPC were used as the anode and

cathode materials, respectively. Single cell performance of LTO was measured in the potential window 1-3 V vs Li. The half cell measurement details for LTO are already discussed in the chapter 3 (figure 3.15). The charge-discharge cycle in the potential window 1-3V at 100 mAg^{-1} and cyclic stability of LTO in the half cell configuration are given in figure 3.15a and 3.15b respctively.

The carbon material was also tested as the cathode material in half cell configuration between 3-4.6 V vs Li. The galvanostatic charge discharge and cyclic stability data of WPC in the single electrode configuration are presented in figures 4.7a and 4.7b, respectively. The linear nature of the charge-discharge data confirms that the charge storage is due to the double layer formation at the electrode-electrolyte interface.

The reversible gravimetric specific capacity obtained for WPC in the single electrode configuration is 70 $mAhg^{-1}$. The specific capacitance obtained for the carbon material in the single electrode configuration for the hybrid system is 160 Fg^{-1}. This value is much higher as compared to that reported for commercial activated carbon and comparable with other porous carbons. 90% capacitance retention was obtained after 600 charge discharge cycles as shown in figure 4.7b. Based on the individual performance of WPC and LTO, the weight ratio required to get charge balance between cathode and anode was obtained to be 2.4:1. The Li-ion hybrid capacitor was then fabricated with this mass ratio between WPC (7 mg) and LTO (3 mg), respectively. Figures 4.7c and d show the electrochemical characterizations of Li-ion hybrid capacitor. Figure 4.7c shows the charge-discharge measurement in the potential window 1-3 V. The non-linear nature of charging and discharging is due to different types of charge storage mechanisms at the two electrodes. While charging, the Li^+ ions in the electrolyte intercalate into $Li_4Ti_5O_{12}$ and as a consequence, the PF_6^- ions get adsorbed on the surface of carbon in order to have charge balance in the electrolyte. Thus, at one electrode it is intercalation while at the other it is surface adsorption. Figure 4.7d shows the cyclic stability of the Li-ion hybrid capacitor. 85% of capacitance retention was observed even after 5000 charge-discharge cycles. The decrease in the capacitance can be due to the reaction between the electrolyte and the Li insertion electrode.

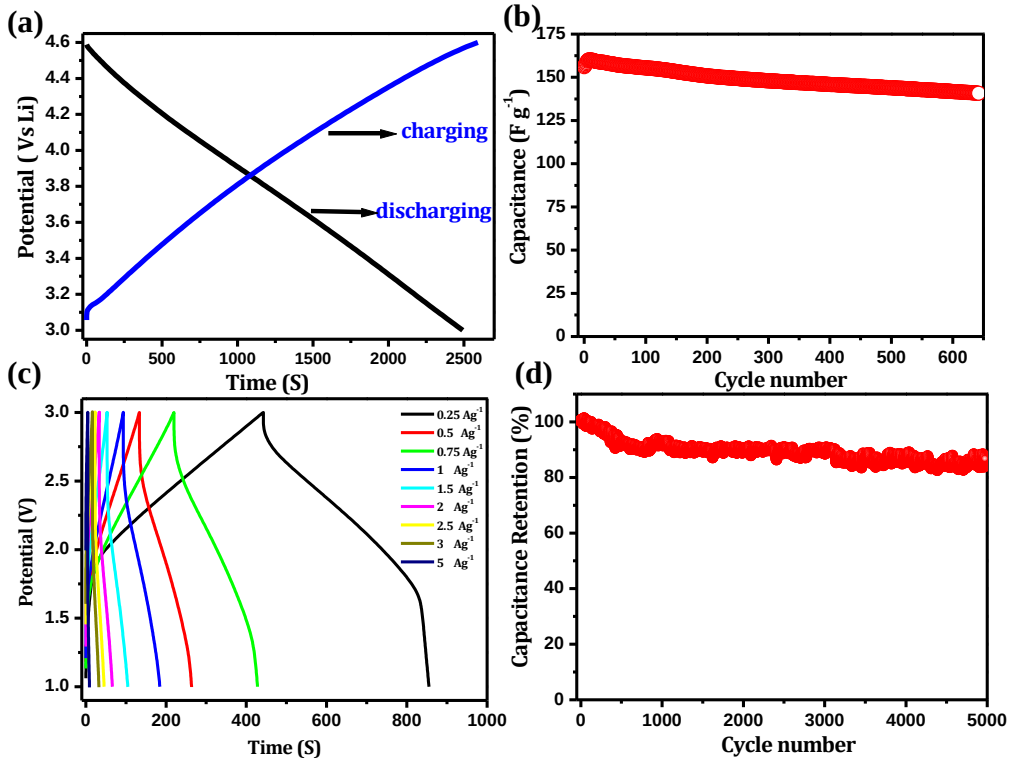

Figure 4.7 (a) Galvanostatic charge discharge of WPC in the half cell configuration vs Li in the potential range 3-4.6 V at a current density 100 mAg^{-1}, **(b)** Cyclic stability in the half cell configuration, **(c)** Galvanostatic charge-discharge of Li-HEC with WPC as cathode and LTO as anode for different current densities, and **(d)** cyclic stability of Li-HEC.

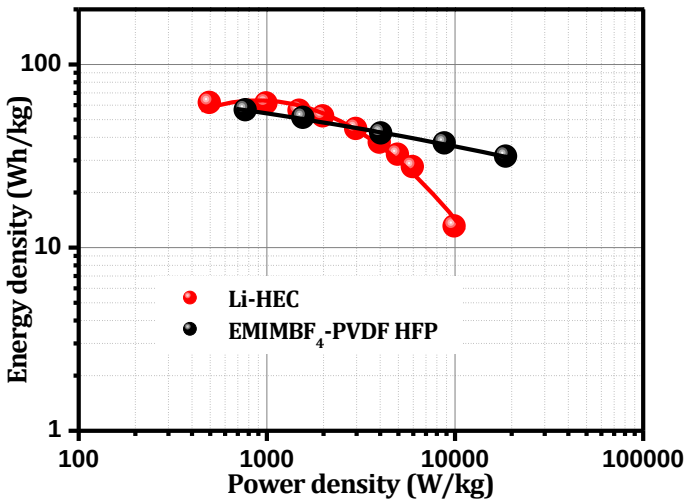

Figure 4.8 Ragone plot comparing the energy density and power density obtained for WPC in solid state supercapacitor and Li-HEC.

The Ragone plot shown in figure 4.8 compares the material specific energy density and power density of the supercapacitors developed using WPC in two different configurations.

The energy density achieved for the hybrid capacitor and ionic liquid based solid state supercapacitor is much higher as compared to that obtained for aqueous based system because of the higher potential window. The maximum energy density and power density achieved for Li-HEC are 62 $Whkg^{-1}$ and 13000 Wkg^{-1} and those for the ionic liquid based solid state supercapacitor are 58 $Whkg^{-1}$ and 19000 Wkg^{-1}, respectively. For the non-aqueous based systems, the energy density and power density are approximately the same at lower discharge rates. The energy density as well as the power density were lower in the Li-ion hybrid capacitor in comparison with the ionic liquid solid state supercapacitor because of the higher resistance observed in the case of Li-HEC. The major resistance contribution in Li-HEC is from the intrinsic resistance of LTO, whereas for the ionic liquid based solid state supercapacitor the series resistance is less because carbon is the active material on both electrodes. The high surface area carbon derived from the waste paper (WPC) is thus observed to exhibit an excellent performance as an electrode material for electrical double layer capacitor as well as hybrid capacitor.

Table 4.1 compares the charge storage performance of WPC and other carbon materials in ionic liquid, in solid as well as in liquid electrolyte configurations. Clearly, the porous carbon derived from waste paper (WPC) shows superior performance as electrode for EDLC in ionic liquid-gel as compared to other activated carbon forms obtained from waste sources. Wang et al. developed porous carbon from hemp fibres and used it as an electrode for ionic liquid based supercapacitors.[33] Among the capacitor measurements done at different temperatures, the highest value of the specific capacitance obtained was nearly 150 Fg^{-1} over the temperature range 60°C-100°C which is much higher than that at the room temperature. At 20°C the highest value of energy density achieved was ~46 $Whkg^{-1}$.

However, the energy density was noted to have dropped down to 4 $Whkg^{-1}$ when the power density was increased to 28000 Wkg^{-1}. Other reports based on graphene or graphene composite with activated carbon derived from conducting polymers

(containing dopants) show charge storage properties slightly superior to WPC, however the precursors and processes are clearly far more expensive.

Electrode Material	Configuration	Specific Capacitance (Fg^{-1})	Current density (Ag^{-1})	Highest Energy and corresponding power density	Highest power and corresponding energy density	Ref
Graphene–carbon composite	Solid state-GO doped IL gel	190	1	76 $Whkg^{-1}$ 900 Wkg^{-1}	57 Wh kg^{-1} 7000W kg^{-1}	31
CNT on nanocellulose paper	Flexible solid. IL gel electrolyte	50	1	15.5 $Whkg^{-1}$ 1.5kWkg^{-1}	30000W kg^{-1} 6 Wh kg^{-1}	32
Commercial AC	Solid state GO doped IL gel	135	1	55 Wh kg^{-1} 800 W kg^{-1}	6500W kg^{-1} 33 Wh kg^{-1}	33
Graphene-AC composite	$EMIMBF_4$	213	1	90 Wh kg^{-1}		34
Carbon from Hemp	BMIM-TFSI at 20°C	150	1	46 Wh kg^{-1}, 750 W kg^{-1}	28000W kg^{-1}, 4 Wh kg^{-1}	35
Carbon from waste paper	Solid state IL-polymer gel	179	1	56 $Whkg^{-1}$, 800W kg^{-1}	19000 Wkg^{-1}, 31 Wh kg^{-1}	This work

Table 4.1 Comparison of the energy storage properties of carbon synthesized from waste office paper in ionic liquid electrolyte with other carbon based systems.

In another report, Zhang et al. developed a supercapacitor with a specific capacitance and energy density of 213 Fg^{-1} and 90 $Whkg^{-1}$, respectively, at a discharge current density of 1 Ag^{-1}. [32] In this case also the supercapacitor was fabricated with porous graphene as the electrode material and $EMIMBF_4$ as the electrolyte. Herein we could achieve a specific capacitance of 179 Fg^{-1} and energy density of 56 $Whkg^{-1}$ with the corresponding power density of 800 Wkg^{-1} at a discharge rate of 1 Ag^{-1} for the solid state supercapacitor developed using carbon from waste office paper. Importantly, at a higher discharge rate of 20 Ag^{-1}, the energy density was retained at 31 $Whkg^{-1}$ and power density was noted to increase significantly to 19000 Wkg^{-1}.

The specific capacitance obtained for WPC (164 Fg^{-1}) in the hybrid capacitor design is clearly superior to other porous carbons. Only the activated graphene based system shows a capacitance which is slightly higher than that obtained for WPC. However,

the energy density obtained for such activated graphene-LTO hybrid capacitor is lower than that for WPC.

Cathode Material	**Anode Material**	**Specific Capacitance (Fg^{-1})**	**Current density (Ag^{-1})**	**Highest Energy and corresponding power density**	**Highest power and corresponding energy density**	**Ref**
Coconut shell derived activated carbon	LTO	140	0.1	69 $Whkg^{-1}$& 500 Wkg^{-1}	4000W kg^{-1} 20 Wh kg^{-1}	[29]
Activated Graphene	LTO	206		40.8		[36]
Graphene	LTO	160	0.25	45 Wh kg^{-1} 400 W/kg	3500W kg^{-1} 30 Wh kg^{-1}	[37]
MOF -C	LTO	149	0.15	65 Wh kg^{-1}, 500 W/kg	10000W kg^{-1} 9 Wh kg^{-1}	[38]
Porous 3D graphene	G-LTO	-	-	95 Wh kg^{-1} , 54 W kg^{-1}	3000W kg^{-1}, 32 Wh kg^{-1}	[39]
Carbon from waste paper	LTO	164	0.1	61 Wh kg^{-1} 500 W kg^{-1}	10 000W kg^{-1} 13 Wh kg^{-1}	This work

Table 4.2 Comparison of WPC as cathode in Li-HEC with other carbon systems

A comparison between our carbon sample (WPC) and other carbon materials as cathode material for Li-HEC is given in table 4.2.

Energy density of 95 Wh kg^{-1} was achieved for Li-HEC in a report by Leng at al.[39] where 3D porous graphene and its composite with LTO were used as the cathode and anode, respectively. It is important to note however that the highest power density obtained was 3000 W kg^{-1} which is substantially less as compared to that obtained for WPC (10000 W kg^{-1}).

4.4 Conclusion

High surface area porous carbon with three dimensionally interconnected hierarchically porous morphology was synthesized from waste office (shredded) paper by a two step process which includes hydrothermal treatment followed by high temperature pyrolysis. A very high BET specific surface area of ~ 2341 m^2g^{-1} was obtained for this carbon. The presence of micropores as well as mesopores makes the material an ideal candidate for EDLC electrode. The electrode made of this carbon

showed excellent performance in ionic liquid solid state supercapacitor as well as Li-ion hybrid capacitor. The interconnected macroporous structure facilitated the penetration of gel-electrolyte into the inner layers and helped realize a nearly equal performance for both solid and liquid based devices. Maximum energy density and power density of 58 Wh kg^{-1} and 19000W kg^{-1} were achieved for the solid state supercapacitor in the two electrode configuration at room temperature. The Li-ion hybrid capacitor also yielded a maximum energy density and power density of 62 Wh kg^{-1} and 13000W kg^{-1}, respectively.

4.5 References

1. A. S. Arico, P. Bruce, B. Scrosati, J. M. Tarascon and W. Van Schalkwijk, *Nature Mater.*, 2005, **4**, 366-377.
2. X. Chen, C. Li, M. Gratzel, R. Kostecki and S. S. Mao, *Chem. Soc. Rev.*, 2012, **41**, 7909-7937.
3. M. Winter and R. J. Brodd, *Chem. Rev.*, 2004, **104**, 4245-4270.
4. J. R. Miller and P. Simon, *Science*, 2008, **321**, 651-652.
5. L. L. Zhang and X. S. Zhao, *Chem. Soc. Rev.*, 2009, **38**, 2520-2531.
6. L. Dai, D. W. Chang, J.-B. Baek and W. Lu, *Small*, 2012, **8**, 1130-1166.
7. Y. Zhai, Y. Dou, D. Zhao, P. F. Fulvio, R. T. Mayes and S. Dai, *Adv. Mater.*, 2011, **23**, 4828-4850.
8. K. Karthikeyan, S. Amaresh, S. N. Lee, X. Sun, V. Aravindan, Y.-G. Lee and Y. S. Lee, *Chemsuschem*, 2014, **7**, 1435-1442.
9. H. Zhu, X. L. Wang, X. X. Liu and X. R. Yang, *Adv. Mater.*, 2012, **24**, 6524-6529.
10. L. Qie, W. Chen, H. Xu, X. Xiong, Y. Jiang, F. Zou, X. Hu, Y. Xin, Z. Zhang and Y. Huang, *Energy Environ. Sci.*, 2013, **6**, 2497-2504.
11. D. Puthusseri, V. Aravindan, S. Madhavi and S. Ogale, *Energy Environ. Sci.*, 2014, **7**, 728-735.
12. R. Silva, D. Voiry, M. Chhowalla and T. Asefa, *J. Am. Chem. Soc.*, 2013, **135**, 7823-7826.
13. H.-L. Jiang, B. Liu, Y.-Q. Lan, K. Kuratani, T. Akita, H. Shioyama, F. Zong and Q. Xu, *J. Am. Chem. Soc.*, 2011, **133**, 11854-11857.

14. J. Ding, H. Wang, Z. Li, A. Kohandehghan, K. Cui, Z. Xu, B. Zahiri, X. Tan, E. M. Lotfabad, B. C. Olsen and D. Mitlin, *ACS Nano*, 2013, **7**, 11004-11015.
15. K. Naoi, W. Naoi, S. Aoyagi, J.-i. Miyamoto and T. Kamino, *Acc. Chem. Res.*, 2012, **46**, 1075-1083.
16. G. G. Amatucci, F. Badway, A. Du Pasquier and T. Zheng, *J. Electrochem. Soc.*, 2001, **148**, A930-A939.
17. X. Lu, M. Yu, G. Wang, Y. Tong and Y. Li, *Energy Environ. Sci.*, 2014.
18. D. Kalpana, S. H. Cho, S. B. Lee, Y. S. Lee, R. Misra and N. G. Renganathan, *J. Power Sources*, 2009, **190**, 587-591.
19. M.-C. Liu, L.-B. Kong, C. Lu, X.-M. Li, Y.-C. Luo and L. Kang, *RSC. Advances.*, 2012, **2**, 1890-1896.
20. B. Hu, K. Wang, L. H. Wu, S. H. Yu, M. Antonietti and M. M. Titirici, *Adv. Mater.*, 2010, **22**, 813-828.
21. Z. Q. Li, C. J. Lu, Z. P. Xia, Y. Zhou and Z. Luo, *Carbon*, 2007, **45**, 1686-1695.
22. A. M. Rao, A. Jorio, M. A. Pimenta, M. S. S. Dantas, R. Saito, G. Dresselhaus and M. S. Dresselhaus, *Phys. Rev. Lett.*, 2000, **84**, 1820-1823.
23. Y. Zhu, S. Murali, M. D. Stoller, K. J. Ganesh, W. Cai, P. J. Ferreira, A. Pirkle, R. M. Wallace, K. A. Cychosz, M. Thommes, D. Su, E. A. Stach and R. S. Ruoff, *Science*, 2011, **332**, 1537-1541.
24. A. Kajdos, A. Kvit, F. Jones, J. Jagiello and G. Yushin, *J. Am. Chem. Soc.*, 2010, **132**, 3252-3253.
25. A. C. Ferrari and D. M. Basko, *Nature Nanotechnology*, 2013, **8**, 235-246.
26. H. Jiang, P. S. Lee and C. Li, *Energy Environ. Sci.*, 2013, **6**, 41-53.
27. J.-S. Lee, S.-I. Kim, J.-C. Yoon and J.-H. Jang, *ACS Nano*, 2013.
28. P. Simon and Y. Gogotsi, *Nature Mater.*, 2008, **7**, 845-854.
29. A. Jain, V. Aravindan, S. Jayaraman, P. S. Kumar, R. Balasubramanian, S. Ramakrishna, S. Madhavi and M. P. Srinivasan, *Sci Rep-Uk*, 2013, **3**.
30. D. Puthusseri, V. Aravindan, S. Madhavi and S. Ogale, *Electrochim. Acta*, 2014, **130**, 766-770.
31. X. Yang, L. Zhang, F. Zhang, T. Zhang, Y. Huang and Y. Chen, *Carbon*, 2014, **72**, 381-386.

32. Y. J. Kang, S. J. Chun, S. S. Lee, B. Y. Kim, J. H. Kim, H. Chung, S. Y. Lee and W. Kim, *ACS Nano*, 2012, **6**, 6400-6406.

33. X. Yang, F. Zhang, L. Zhang, T. F. Zhang, Y. Huang and Y. S. Chen, *Adv. Funct. Mater.*, 2013, **23**, 3353-3360.

34. F. Zhang, Y. Lu, X. Yang, L. Zhang, T. Zhang, K. Leng, Y. Wu, Y. Huang, Y. Ma and Y. Chen, *Small*, 2014, n/a-n/a.

35. H. Wang, Z. W. Xu, A. Kohandehghan, Z. Li, K. Cui, X. H. Tan, T. J. Stephenson, C. K. King'ondu, C. M. B. Holt, B. C. Olsen, J. K. Tak, D. Harfield, A. O. Anyia and D. Mitlin, *ACS Nano*, 2013, **7**, 5131-5141.

36. M. D. Stoller, S. Murali, N. Quarles, Y. W. Zhu, J. R. Potts, X. J. Zhu, H. W. Ha and R. S. Ruoff, *Phys. Chem. Chem. Phys.*, 2012, **14**, 3388-3391.

37. V. Aravindan, D. Mhamane, W. C. Ling, S. Ogale and S. Madhavi, *Chemsuschem*, 2013, **6**, 2240-2244.

38. A. Banerjee, K. K. Upadhyay, D. Puthusseri, V. Aravindan, S. Madhavi and S. Ogale, *Nanoscale*, 2014, **6**, 4387-4394.

39. K. Leng, F. Zhang, L. Zhang, T. F. Zhang, Y. P. Wu, Y. H. Lu, Y. Huang and Y. S. Chen, *Nano Res*, 2013, **6**, 581-592.

Chapter 5

Co_3O_4 nanoparticle loaded 3D interconnected porous graphene for Li-ion battery anode

Co_3O_4/porous graphene (PG) nanocomposite synthesized by simple solvothermal route is used as anode material in Li-ion battery. The ratio of graphene to Co_3O_4 is optimized to get its best possible performance. Among the different compositions investigated, the composite PG-600 (with 50% PG) shows a discharge capacity of 700 mAh g^{-1} at a current density of 500mA g^{-1} and maintains 90% retention after 80 cycles. The increased surface area and electrical conductivity of the composite result into an enhancement in the capacity, cycling stability and rate capability as compared to native Co_3O_4 phase.

5.1 Introduction

Rechargeable Li-ion batteries (LIB) are considered as one of most promising energy storage technology in this era for current energy requirements as well as future demands.[1, 2] However, the low power capability restricts its application where high power is needed like zero emission transportation applications. This is mainly because of the limited capacity of the conventional graphitic anodes (~372 mAh g^{-1}) and their poor high current performance.[2] Hence, the current research direction is focussed on the development of a high capacity alternate anode material for LIB applications. Along this line, Poizot *et al*[3] first reported the possibility of using nano-sized transition metal oxides (TMO) as high capacity anodes. Unlike graphitic anodes (intercalation), metal oxides react with Li-ions and subsequently reduce metallic form (M^o) which translates into high capacity for such anodes according to the following "conversion" or "displacement" mechanism, $M_xO_y + 2yLi^+ + 2ye^- \leftrightarrow xM^o + yLi_2O$. So far, numerous binary and ternary metal oxides have been exploited as high performance anode materials for LIB applications.[4] Among them, Co_3O_4 is found to be attractive in terms of its high theoretical capacity (~890mAhg^{-1}) and high power capability.[5, 6]

One of the major issues for TMO is the capacity fading, because of the large volume expansion/contraction of the active material during conversion reaction.[7] Apart from this issue, relatively lower electrical conductivity of TMO in comparison with graphite anodes forbids realization of the desired power capability in Li-ion power packs. Surface modification of TMO with carbon certainly overcomes the power capability issue, but the cycling stability remains a problem after certain number of cycles. Another alternate approach is to disperse the active materials into conducting matrix (preferably carbonaceous materials) which provides many advantages like better rate capability and cyclic stability *via* sustenance of the volume variation and enhancement of the electrical conductivity.[8, 9] So far, various carbon nanostructures such as carbon nanotubes, graphene, carbon fibre etc., have been explored as the conducting matrix.[10, 11] Utilization of porous carbonaceous materials as matrix element for the dispersion of active material is one of the efficient ways to achieve high power capability with good cyclic stability.

Researchers have introduced porous graphene as the conducting matrix for the preparation of high power anode material, which can offer high specific surface area as compared to its normal forms.[12] Along this line, we report the synthesis and optimization of Co_3O_4 into high surface area 3D porous graphene interconnected matrix and evaluation of its application in Li-ion battery as an anode. An extensive study has been carried out for the optimization of the Co_3O_4-3D porous graphene composites and the same is described in detail.

5.2 Experimental Techniques

Starting materials, poly(styrene sulfonic acid-co-maleic acid) sodium salt and cobalt acetylacetonate were purchased from Sigma-Aldrich and used as such without any further purification.

5.2.1 Synthesis of 3D porous graphene (3D PG)

The high surface area 3D porous graphene was synthesised by using the methods reported elsewhere.[13] Briefly, poly (styrene sulfonic acid-co-maleic acid) sodium salt was carbonized at 1000^{o}C in inert atmosphere for 4h at a heating rate of 10^{o}C min^{-1}. The resulting product was washed with dil. HCl to remove the inorganic impurities, if any. Then, the final product, porous graphene was dried in vacuum oven, before conducting the physico-chemical characterization.

5.2.2 Synthesis of Co_3O_4- 3D Porous Graphene (3D PG -Co_3O_4) composites

Co_3O_4 nanoparticles were synthesised by simple solution processing method followed by annealing. In the typical procedure, 0.6 g of cobalt acetylacetonate was dispersed in a mixture of 10 ml. of iso-propanol and 1ml acetic acid. This mixture was kept at 90^{o}C for 10 h. After drying the powder was annealed at 300^{o}C for 3 h in air to get the crystalline Co_3O_4 nanoparticles. The composite with 3D porous graphene was synthesised by dispersing the graphene in iso-propanol prior to the addition of cobalt acetylacetonate. The composites with different amounts of graphene was synthesised by varying the graphene concentration and keeping other parameters such as cobalt acetylacetonate and

solvent constant. The samples were named as 3D PG-X where X is the amount of porous graphene added in milligrams.

5.2.3 Structural Characterizations

Powder X-ray diffraction was performed using PAN Analytical powder X-ray diffractometer with nickel-filtered Cu K_α radiation. Raman spectrum was recorded to validate the presence of carbonaceous materials in the composite using LabRAM HR800 from JY Horiba. The structural and morphological characterizations were performed by Field emission scanning electron microscopy (FE-SEM, FEI Nova NanoSEM 450) and high resolution transmission electron microscopy (HR-TEM, FEI, Tecnai F30, FEG with 300 kV). Thermo-gravimetric analysis (TGA) was also performed to quantify the amount of carbonaceous materials in each composite.

5.2.4 Electrochemical measurements

Electrochemical measurements were carried out by using two electrode CR 2016 coin cell configurations in ambient temperature conditions. Working electrodes of Co_3O_4 and its composites with porous graphene were prepared by making slurry of active material (70% (wt.%)) with conducting carbon (Super-P) (15%) and binder (teflonized acetylene black, TAB-2) (15%) using ethanol as solvent and pressed over 200 mm^2 stainless steel mesh (Goodfellow, UK). Electrodes were dried at 60 °C under vacuum for 4 h before conducting cell assembly. Metallic Li was used as counter and reference electrode in all the cases. Microporous fiber paper (Whatman Cat. No. 1825-047, UK) was used as a separator to split the working and counter/reference electrodes. 1M $LiPF_6$ in ethylene carbonate (EC)/di-methyl carbonate (DMC) (1:1 wt.%, Selectipur LP 30, Merck KGaA, Germany) was used as electrolyte solution. Cyclic voltammetry and A.C. impedance measurements were performed using Solartron, 1470E and SI 1255B Impedance/gain-phase analyser coupled with a potentiostat. Galvanostatic cycling performances were recorded at constant current mode between 0.005-3 V *vs.* Li at various current densities using Arbin 2000 battery tester.

5.3 Results and Discussion

Figure 5.1 shows the schematic representation of the synthesis procedure used for the preparation of 3D PG-Co_3O_4 nanocomposites. Organic moieties present in the precursor are removed after heat treatment at 300 °C in air atmosphere.

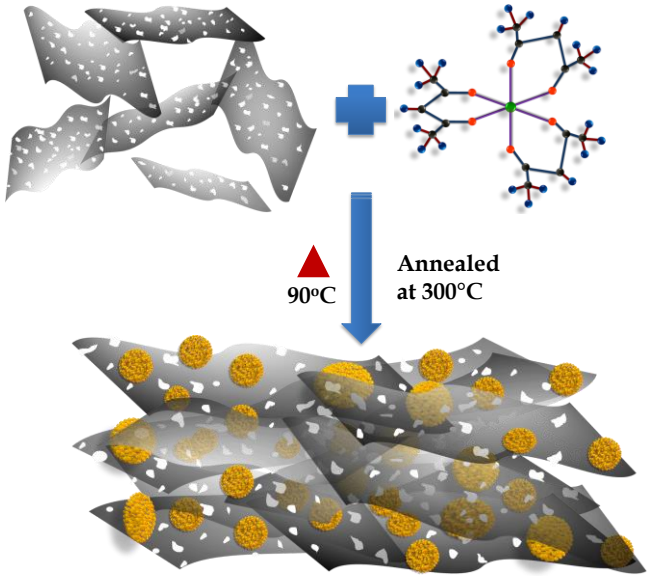

Figure 5.1 Schematic representation of synthesis of 3D PG -Co_3O_4 composite

As a result, the Co_3O_4 particles are firmly anchored onto the porous graphene sheets. In addition, the heat treatment also helps to form crystalline particles. Powder X-ray diffraction was performed to confirm the crystal structure of Co_3O_4 and its composites with various amounts of porous graphene with graphene content varying from 20 mg to 1 g and is shown in figure 5.2.

Presence of the specific reflections in XRD pattern indicates that the Co_3O_4 nanoparticles have face centred cubic crystal structure (PCPDFWIN-PDF#781970). In the composites, an additional peak near 26° is also noted which corresponds to the graphitic nature of the porous graphene derived from the polymer.[13] It is observed that the intensity of the peak increases with increase in the carbonaceous material loading in the composite.

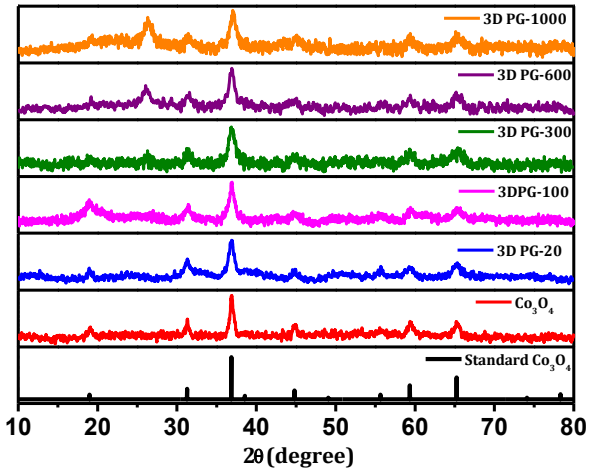

Figure 5.2 Powder X ray diffraction pattern of standard Co_3O_4 (PCDPF), Co_3O_4 and the composites with 3D-porous graphene with different amount of graphene content

Raman spectrum is one of the important tools to study the nature of the carbonaceous material present in the composite.[14] Therefore, the 3D-PG, Co_3O_4 and the composites were further characterized by Raman spectroscopy to confirm the formation of an appropriate composite and the corresponding data are shown in figure 5.3.

Presence of prominent peaks at ~1326, ~1574 and ~2646 cm^{-1} observed for the nanocomposites as well as for pristine 3D PG corresponds to the characteristic bands of graphene.[15] The peak near to ~1326 cm^{-1} corresponds to the D band which arises due to defects and is commonly observed in micro/mesoporous and amorphous carbon and the one at ~1574 cm^{-1} corresponds to sp^2 bonded carbon which is the characteristic peak of graphite.[16] The peak positioned at ~2646 cm^{-1} corresponds to the 2D band which is absent in graphite and amorphous carbon and is characteristic peak for graphene. The intensity of the 2D peak depends on the number of graphene layers.[14, 17] The Raman result thus clearly suggests that the prepared 3D-PG is few layer graphene with porosity in it. Similarly, the lower energy bands positioned at ~191, ~474, ~510 and ~675 cm^{-1} are associated with E_g, $F^{12}{}_m$, $F^{22}{}_g$ and A_{1g} vibration modes of Co_3O_4.[18] The characteristic peaks of graphene are absent in the composites 3D PG-20 and 3D PG-100. This is probably due to the relatively lower carbonaceous content present in the composite. Rest of the composites, 3D PG-300, 3D PG-600 and 3D PG-1000 showed the characteristic

peaks of both graphene and Co_3O_4, which clearly reveal the crystalline metal oxide nanoparticles embedded in the graphene matrix, which subsequently translates into improved electrochemical profiles.

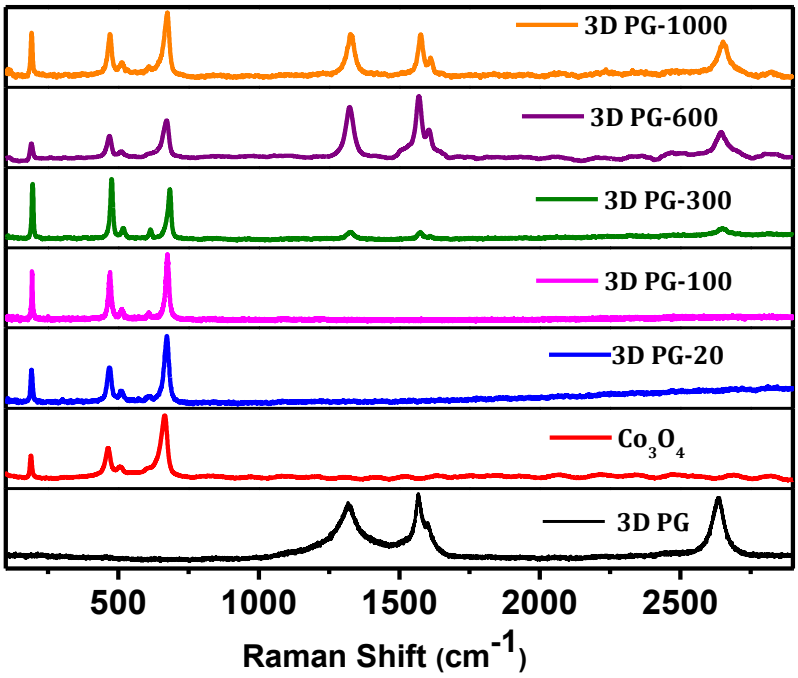

Figure 5.3 Raman spectra of 3D PG, Co_3O_4 and the composites by varying the graphene percentage.

It is important to quantify the exact amount of carbonaceous materials present in the various nanocomposites before the electrochemical measurements. Hence, thermo-gravimetric analysis (TGA) was performed for all the composites in the air atmosphere with heating rate of 10 °C min^{-1} and the data are given in figure 5.4. For comparison purpose, pure Co_3O_4 and 3D-PG samples were also subjected for TGA analysis under similar testing conditions. An increase in weight loss was observed with increase in graphene content from 20 mg to 1 g. A substantial weight loss is observed for the composites 3D PG-300, 3D PG-600 and 3D PG-1000 beyond 450 °C as compared to pure Co_3O_4, 3D PG-20 and 3D PG-100. This weight loss is seen between 450 to 600 °C which corresponds to the oxidation of carbon ($C + O_2 \rightarrow CO_2$), consistent with the pure 3D-PG.[19, 20]

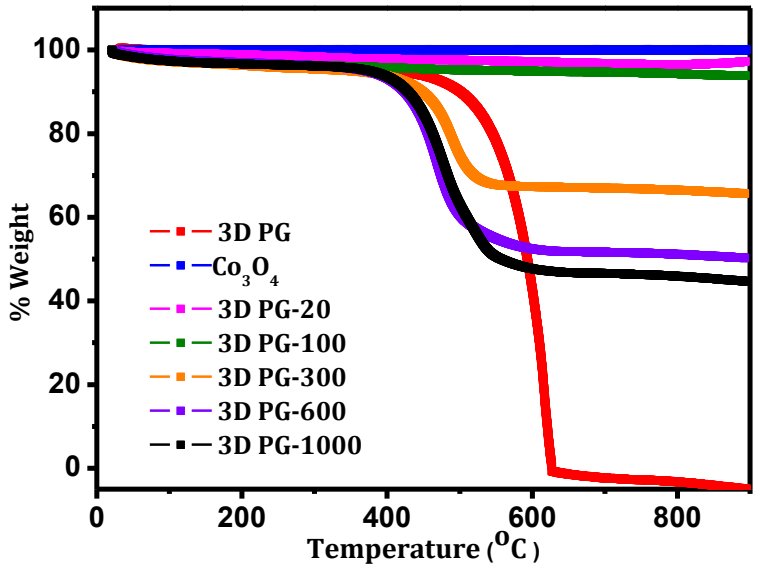

Figure 5.4 Thermo gravimetric analysis of Co_3O_4 and its composites with 3D porous graphene which provides the amount of carbon content in different composites

At this point, it was very difficult to pick the right composition for the extensive physico-chemical and electrochemical characterizations. Therefore, preliminary electrochemical studies were performed for all the Co_3O_4 nanocomposites, as discussed below.

The preliminary measurements were done in a half-cell configuration for all the composites in the voltage range 0.005-3 V *vs.* Li at current density of 100mAg^{-1}. Figure 5.5a shows the electrochemical cycling profiles of various 3D-PG-Co_3O_4 nanocomposites carried out in ambient temperature conditions. It is clearly observed that the 3D-PG-Co_3O_4 nanocomposites with higher amount of carbon loading delivered favourable battery performance. More importantly, Co_3O_4 nanocomposites with 300, 600 and 1000 mg 3D porous graphene loadings are found to be very promising in terms of high reversible capacity and cycling stability. For example, the test cells delivered the discharge capacity of ~823, ~740 and ~746 mAh g^{-1} in the second cycle for 3D PG-300, 3D PG-600 and 3D PG-1000, respectively.

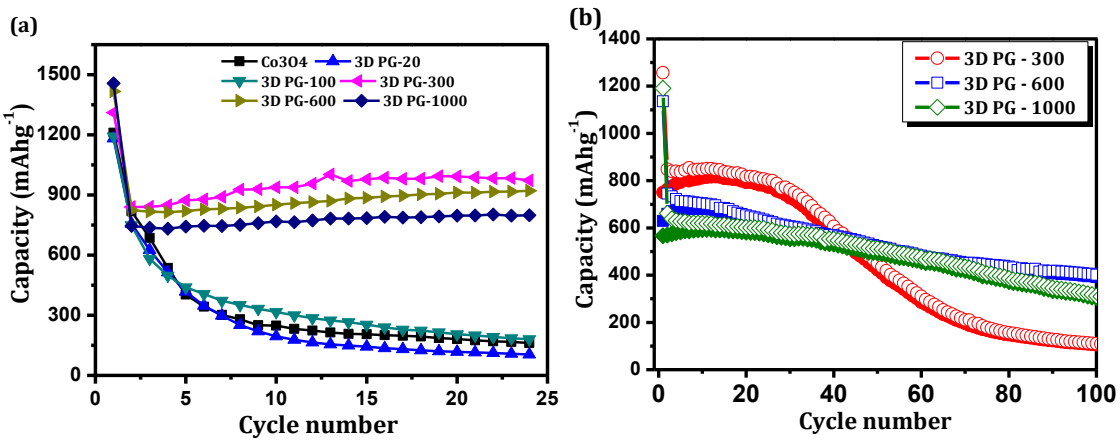

Figure 5.5 Reversible discharge cyclic stability of Co_3O_4 and different composites at discharge current densities (**a)** 100 mA g^{-1} and **(b)** 500 mAg^{-1}

Although, rest of the compositions exhibit higher reversible capacity in the first cycle, they failed to retain the capacity upon cycling. This is mainly because of the insufficient carbon loading which cannot sustain the volume variation during the charge-discharge process.[10, 21, 22] Hence, only the mentioned three composites were tested at higher discharge current rates (500 mA g^{-1}) for the extended cycling and the data are shown in figure 5.5b. It is interesting to note that, increasing the 3D PG content results in a decrease in the capacity profiles upon cycling. This is mainly because presence of too much carbonaceous material dilutes the active material loading. On the other hand, the enhanced cycling stability is noted when the carbon content is high. The half-cell retains ~14, ~62 and ~54% of initial reversible capacity after 100 cycles for 3D PG-300, 3D PG-600 and 3D PG-1000 composites, respectively. We strongly believe the enhanced cycling profile of 3D PG-600 is mainly attributed by the appropriate optimization of the graphene concentration in the Co_3O_4 nanocomposite. Detailed electrochemical characterizations were also performed for this particular composite to validate the reaction mechanism and its compatibility under high current conditions.

Cyclic voltammetry (CV) studies were performed to understand the reaction mechanism involved in the best performed composite (3D PG-600) and is shown in figure 5.6a. Typical CV traces of 3D PG-600 composites in half-cell configurations are recorded

between 0.005-3 V *vs.* Li at a slow scan rate of 0.1 mVs^{-1}. In the first cathodic sweep, the cell shows two prominent reduction peaks positioned at ~0.55 and ~0.78 V *vs.* Li.

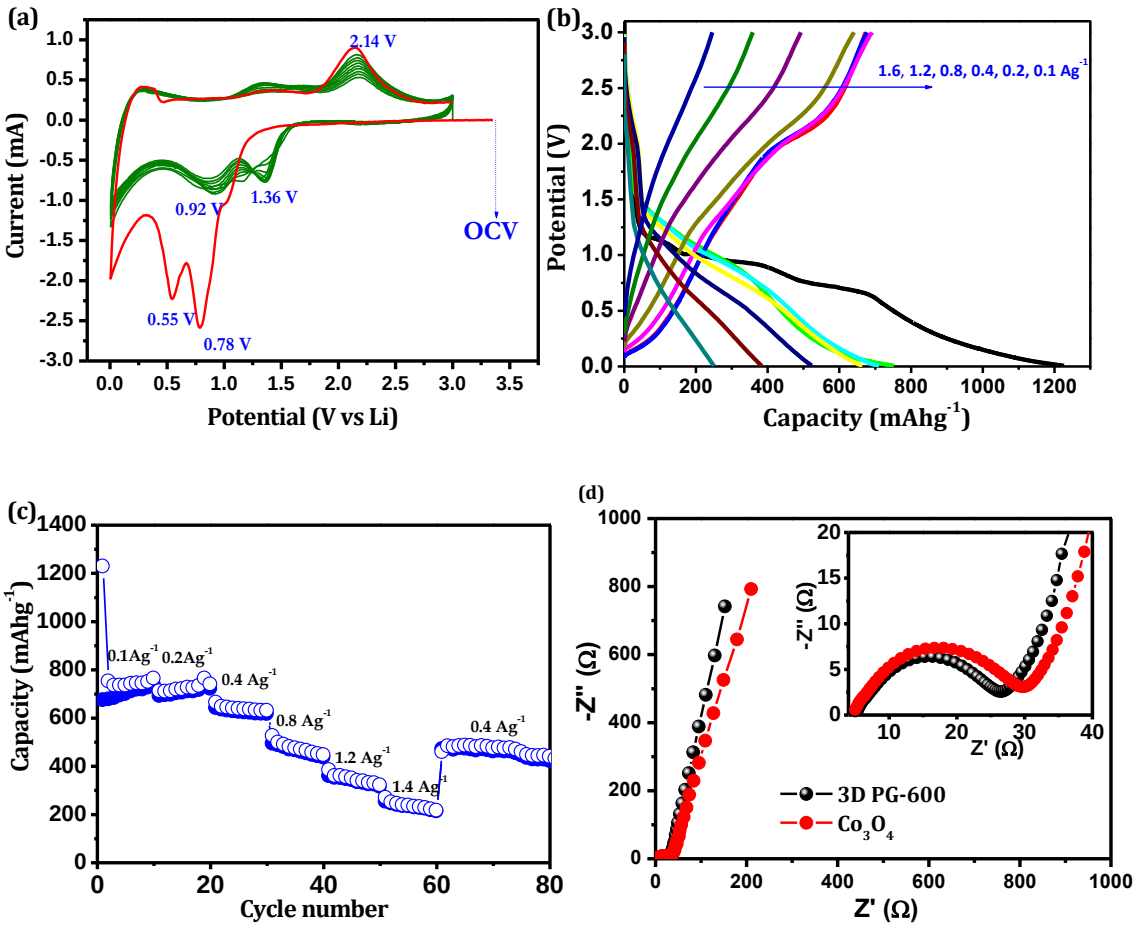

Figure 5.6 (a) Cyclic voltammogram of the best performing composite 3D mV s^{-1}, **(b)** Charge-discharge cycles for 3D PG-600 at different current densities ranges from 0.1-1.6 A g^{-1}, **(c)** Charging and discharging capacities corresponding to various discharge current densities and **(d)** Electrochemical impedance spectroscopy of 3D PG-600 and Co_3O_4.

These peak positions correspond to the irreversible electrolyte decomposition and subsequent solid electrolyte interface (SEI) layer formation.[23, 24] The peak at ~2.14 V *vs.* Li during anodic scan is associated with the partial oxidation of metallic Co^0 to Co^{3+}. Second cycle onwards, the test cell exhibited two prominent cathodic peaks at ~1.36 and ~0.92 V *vs.* Li corresponding to the reduction Co^{3+} to Co^{2+} and Co^{2+} to Co^0, respectively.[25, 26] Apparently, a drastic reduction in the area under the curve is noted

between the first and subsequent cycles which confirms the irreversibility in the first cycle. The overall reaction mechanism involved in the charge-discharge process is described as $Co_3O_4 + 8Li \leftrightarrow 3Co^0 + 4Li_2O$. [27] Decrease in the current density for both anodic and cathodic scans is noted with increasing cycle number which indicates the capacity fading during cycling. Galvanostatic charge-discharge curves and the corresponding discharge and charge capacities observed for 3D PG-600 in the half-cell configuration at different current densities are shown in the Figure 5.6b and c. At low current rate (100 mA g^{-1}), a definite irreversible capacity loss is noted in the first cycle which corresponds to the electrolyte decomposition and subsequent SEI formation.[28] The observed irreversible capacity loss in the galvanostatic cycling is concurrent with the decrease in area under the curve observed in the cyclic voltammogram. The discharge and charge capacities obtained from the galvanostatic measurements for different cycles are given in the figure 5.6c. Initial reversible capacity of ~800 mAh g^{-1} is noted at low current rate of 100 mAg^{-1}, which is close to the theoretical capacity of Co_3O_4 (890 $mAhg^{-1}$). As expected, decrease in capacity trend is noted with increase in applied charge discharge rate. This may be due to the limited accessible surface area of the active material at higher discharge rates, because at lower discharge rates, the surface as well as the bulk of the material will be accessible for the electrochemical reaction and hence deliver higher reversible capacity. Except for the few initial cycles, the columbic efficiency is found over 99% irrespective of the applied current rates, which indicates the excellent reversibility of the system.

Electrochemical impedance spectroscopy measurement was carried out to understand the charge transfer and Li^+ ion diffusion kinetics in bare Co_3O_4 as well as the best performing composite (3D PG-600). The Nyquist plot obtained from EIS measurement carried out in the frequency range 100 mHz-100 kHz is shown in the figure 5.6d. The semicircle which corresponds to the charge transfer resistance is larger in diameter in the case of pristine Co_3O_4 as compared to 3D PG-600. The charge transfer mainly depends on the electrical conductivity of the electrode materials. The lower charge transfer resistance for 3D PG-600 can be due to the increased electrical conductivity because of the presence of graphene nanosheets.[11, 29]

In order to elucidate the nature of the microstructure of the 3D PG-600 nanocomposite which showed the best performance it was analyzed using FE-SEM and HR-TEM imaging and diffraction. For comparison, the Co3O4 was also subjected to the same analyses. Figure 5.7 shows the FE-SEM images Co_3O_4 and 3D PG-600 and the HR-TEM images of 3D PG-600. Apparent to note that from the FE-SEM images (Figure 5.7 (a-c)), the size of the typical Co_3O_4 spheres obtained from the simple solution process is between 100-200nm range with spherical shaped morphology. The FE-SEM images of Co_3O_4 spheres shows that the big spheres constitute of Co_3O_4 nanoparticles with size ranges from 5-20 nm. Surface morphology of the composites (Figure 5.7 (d-f)) clearly shows the presence of uniformly distributed Co_3O_4 nanoparticles over graphene nanosheets.

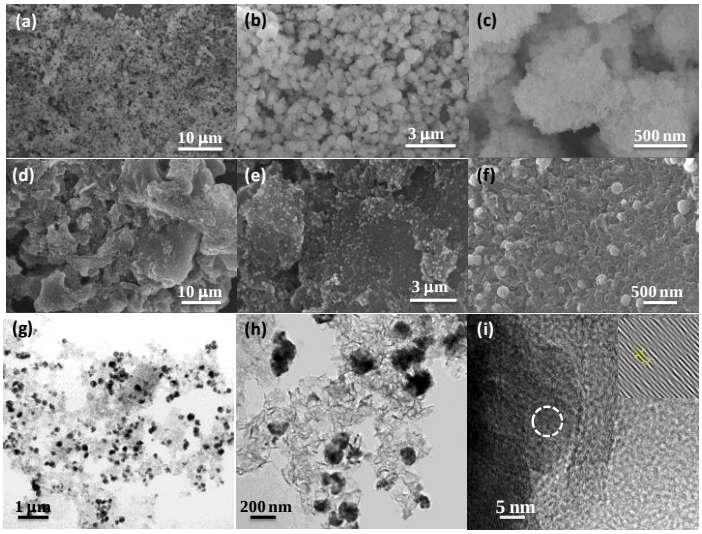

Figure 5.7 (a-c) FESEM images of Co_3O_4, FESEM **(d-f)** and HRTEM **(g-i)** of 3D PG-600 at different magnifications.

The uniform distribution and anchoring of Co_3O_4 nanoparticles over graphene nanosheets are clearly supported by the TEM images shown in figure 5.7(g-i). HR-TEM of the composites confirms the formation of graphene nanosheets and parallels the Raman data obtained for the composite.

Elemental mapping of 3D PG-600 shown in the figure 5.8 clearly shows uniform distribution of the elements carbon, cobalt and oxygen which also confirms Co_3O_4 is

uniformly distributed in the porous graphene matrix. Here, the graphene sheets act as supporting matrix for the Co_3O_4 nanoparticles, which can improve the high current performance and sustain the volume variation occurred during charge-discharge process. Therefore, improved electrochemical performances result for the case of 3D PG-600 nanocomposite.

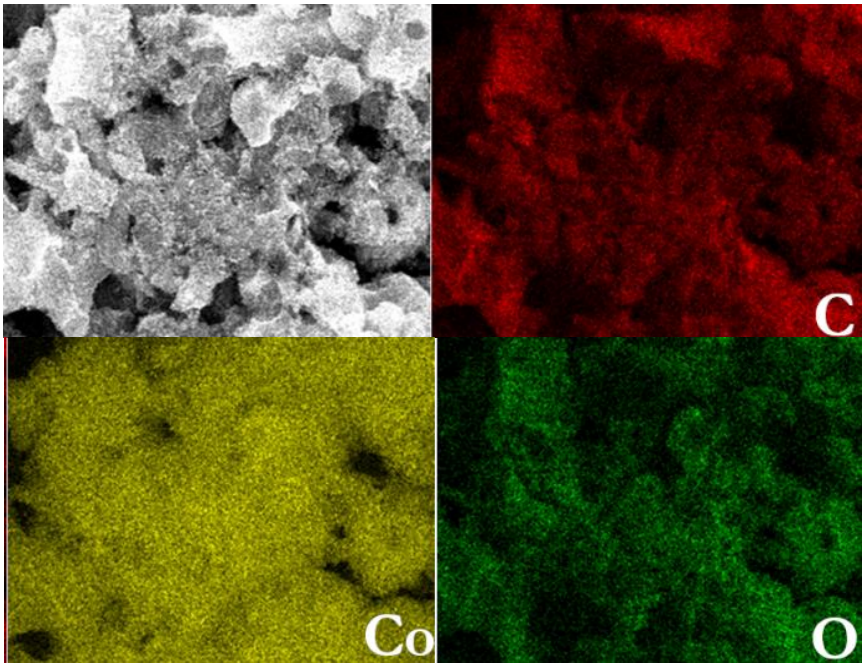

Figure 5.8 FESEM elemental mapping of 3D PG-600 for the elements Carbon (C), Cobalt (Co) and Oxygen (O)

BET specific surface area is also one of the important parameter for such conversion type anodes. Towards this end, N_2 adsorption-desorption analyses were also carried out for pure Co_3O_4, 3D PG and the best performing nanocomposite (3D PG-600). Figure 5.9a shows the N_2 isotherm for Co3O4 and 3D PG-600. The BET specific surface area values of 116.46 and 29.08 $m^2 g^{-1}$ were obtained for 3D PG-600 and pristine Co_3O respectively. The increase in the specific surface area of the 3D PG-600 nanocomposite is mainly because of the usage of the porous graphene with high surface area of 1100 m^2g^{-1} and the N_2 isotherm for 3D PG is given in figure 5.9b.

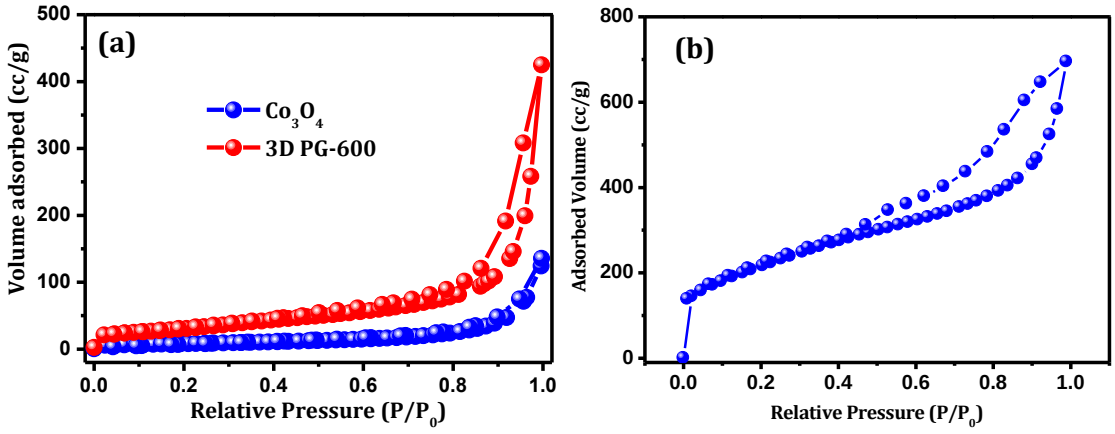

Figure 5.9 N_2 adsorption-desorption isotherms for **(a)** Co_3O_4 and 3D PG-600 and **(b)** 3D PG

5.4 Conclusion

In summary, composite of Co_3O_4 nanoparticles with 3D-porous graphene shows better stability and reversible discharge capacity as compared to bare Co_3O_4 nanoparticle system. Use of an optimum amount of high surface area conducting 3D-porous graphene matrix is shown to drastically increase the cyclic stability of the electrode material. The increase in the surface area and conductivity of the composite material as compared to Co_3O_4 results in increased capacity and better stability. The highest reversible discharge capacity was obtained for the composite 3D PG-300 case. Capacity retention of more than 60% was achieved for the composite 3D PG-600 at high current cycling. This procedure can be easily translated to other metal oxides to realize the betterment in battery performance as anode for LIB applications.

5.5 References

1. J. B. Goodenough and K.-S. Park, *Journal of the American Chemical Society*, 2013, **135**, 1167-1176.
2. V. Etacheri, R. Marom, R. Elazari, G. Salitra and D. Aurbach, *Energy & Environmental Science*, 2011, **4**, 3243-3262.
3. P. Poizot, S. Laruelle, S. Grugeon, L. Dupont and J. M. Tarascon, *Nature*, 2000, **407**, 496-499.
4. M. V. Reddy, G. V. Subba Rao and B. V. R. Chowdari, *Chemical Reviews*, 2013, **113**, 5364-5457.
5. F. Badway, I. Plitz, S. Grugeon, S. Laruelle, M. Dollé, A. S. Gozdz and J.-M. Tarascon, *Electrochemical and Solid-State Letters*, 2002, **5**, A115-A118.
6. P. Poizot, S. Laruelle, S. Grugeon, L. Dupont and J. M. Tarascon, *Journal of Power Sources*, 2001, **97–98**, 235-239.
7. S. Goriparti, E. Miele, F. De Angelis, E. Di Fabrizio, R. Proietti Zaccaria and C. Capiglia, *Journal of Power Sources*, 2014, **257**, 421-443.
8. Y. Wang, H. J. Zhang, L. Lu, L. P. Stubbs, C. C. Wong and J. Lin, *ACS Nano*, 2010, **4**, 4753-4761.
9. S. A. Needham, G. X. Wang, K. Konstantinov, Y. Tournayre, Z. Lao and H. K. Liu, *Electrochem Solid St*, 2006, **9**, A315-A319.
10. Z. S. Wu, W. C. Ren, L. Wen, L. B. Gao, J. P. Zhao, Z. P. Chen, G. M. Zhou, F. Li and H. M. Cheng, *ACS Nano*, 2010, **4**, 3187-3194.
11. B. G. Choi, S.-J. Chang, Y. B. Lee, J. S. Bae, H. J. Kim and Y. S. Huh, *Nanoscale*, 2012, **4**, 5924-5930.
12. S. Choi, J.-K. Lee and Y. Kang, *Nano Res*, 2015, 1-11.
13. P. Yadav, A. Banerjee, S. Unni, J. Jog, S. Kurungot and S. Ogale, *Chemsuschem*, 2012, **5**, 2159-2164.
14. A. C. Ferrari and D. M. Basko, *Nat Nanotechnol*, 2013, **8**, 235-246.
15. A. C. Ferrari, *Solid State Commun*, 2007, **143**, 47-57.
16. F. Tuinstra and J. L. Koenig, *The Journal of Chemical Physics*, 1970, **53**, 1126-1130.

17. F. Tuinstra and J. L. Koenig, *J Chem Phys*, 1970, **53**, 1126-&.
18. X. Yang, K. Fan, Y. Zhu, J. Shen, X. Jiang, P. Zhao, S. Luan and C. Li, *Acs Appl Mater Inter*, 2013, **5**, 997-1002.
19. H. Chen, M. B. Müller, K. J. Gilmore, G. G. Wallace and D. Li, *Adv Mater*, 2008, **20**, 3557-3561.
20. S. Q. Chen and Y. Wang, *J Mater Chem*, 2010, **20**, 9735-9739.
21. J. Lin, Z. Peng, C. Xiang, G. Ruan, Z. Yan, D. Natelson and J. M. Tour, *ACS Nano*, 2013, **7**, 6001-6006.
22. Y. N. Ko, S. B. Park, S. H. Choi and Y. C. Kang, *Sci. Rep.*, 2014, **4**.
23. N. Jayaprakash, W. D. Jones, S. S. Moganty and L. A. Archer, *Journal of Power Sources*, 2012, **200**, 53-58.
24. R. Z. Yang, Z. X. Wang, J. Y. Liu and L. Q. Chen, *Electrochem Solid St*, 2004, **7**, A496-A499.
25. G. Huang, F. Zhang, X. Du, Y. Qin, D. Yin and L. Wang, *ACS Nano*, 2015, **9**, 1592-1599.
26. M. Xu, F. Wang, Y. Zhang, S. Yang, M. Zhao and X. Song, *Nanoscale*, 2013, **5**, 8067-8072.
27. Y. Xiao, C. Hu and M. Cao, *Journal of Power Sources*, 2014, **247**, 49-56.
28. V. Aravindan, P. Suresh Kumar, J. Sundaramurthy, W. C. Ling, S. Ramakrishna and S. Madhavi, *Journal of Power Sources*, 2013, **227**, 284-290.
29. Y. Wang, F. Yan, S. W. Liu, A. Y. S. Tan, H. Song, X. W. Sun and H. Y. Yang, *J Mater Chem A*, 2013, **1**, 5212-5216.

Chapter 6

Research Summary and Future Scope

In this chapter some of the salient features of our work are highlighted and an attempt to summarize the entire PhD research has been made. In addition to this a broad vision for future research work has also been provided.

6.1 Research Summary

The present work has attempted to develop electrode materials for electrochemical energy storage devices to meet the requirement of future applications. The thesis deals with the synthesis of three dimensionally interconnected hierarchical porous carbon from different precursors and their applications in electrochemical energy storage devices as active material for electrodes and support for the active material. Porous carbon forms were synthesized from different polymers including synthetic as well as natural polymers as the source of carbon.

Alkali metal salt of polymer has been used for the synthesis of porous carbon for the electrical double layer capacitor (EDLC). Polymer salt with optimum ratio of carbon to metal can be used to synthesize high surface area porous carbon with optimum porosity.

Used white paper, a cellulose rich precursor, was also used as the carbon precursor. Hydrothermal carbonization of used papers followed by high temperature treatment in the presence of activation agent was performed to obtain porous carbon. The carbon was also tested for its supercapacitor performance in a non-aqueous solid state supercapacitor and cathode material for Li-ion hybrid capacitor.

Composite of Co_3O_4 particles with 3D porous graphene was synthesized by simple solvothermal route for Li-ion battery anode. The amount of graphene was optimized to achieve the best performance. The composites showed better performance as Li-ion battery anode in terms of stability as well as rate performance compare to bare Co_3O_4.

The chapter-wise summary is discussed in details below.

Non-templated synthesis of interconnected microporous carbon (IMPC) sheets having beehive type morphology by direct pyrolysis of poly(acrylamide-co-acrylic acid) potassium salt in inert atmosphere without any external activation agent was discussed in Chapter 3. The presence of the alkali metal in the selected polymer precursor results in a high specific surface area of 1327 m^2g^{-1}. Importantly, 80% of the pore volume is contributed by micropores with pore size in the range of 1-2 nm which is ideal for use as a material for the electrode of a supercapacitor. The rest of

the accessible surface area is found to be contributed by the small fraction of mesopores and macropores due to the interconnected structure. The presence of three different types of pores makes the material ideal for supercapacitor electrodes. The IMPC material was tested as an electrode in aqueous and non-aqueous supercapacitors. The material showed better performance as cathode material for Lithium-ion hybrid capacitor in comparison with the commercial supercapacitor carbon.

Hydrothermal processing followed by controlled pyrolysis of waste (used) white office paper (a globally collectable shredded paper waste) was performed to obtain high surface area carbon with hierarchical pore size distribution. The BET specific surface area of such carbon is 2341 m^2g^{-1}. The interconnected macroporous structure along with the concurrent presence of mesopores and micropores makes the material ideal for ultracapacitor application. Such waste paper derived carbon (WPC) showed remarkable performance in all solid-state supercapacitor fabricated with ionic liquid-polymer gel electrolyte. The Li-ion electrochemical capacitor constructed using WPC as cathode also showed an excellent energy storage capacity of 61 $Whkg^{-1}$.

Increased surface to volume ratio and tunable electronic and optical properties of nanomaterials have expanded their use in a variety of applications, importantly the energy conversion and storage applications. Composite of Co_3O_4 with 3D porous graphene was synthesized by a simple solvothermal route for Li-ion battery anode. The ratio of graphene to Co_3O_4 was optimized to get its best possible performance. Among the different compositions investigated, the composite PG-600 (with 50% PG) shows a discharge capacity of 700 mAh g^{-1} at a current density of 500mA g^{-1} and maintains 90% retention after 80 cycles. The high surface area of PG sheets helps the Co_3O_4 nanoparticles to form a uniform dispersion on it. The increased surface area and electrical conductivity of the composite resulted in an enhancement in the capacity, cycling stability and rate capability as compared to native Co_3O_4 phase.

6.2 Future Outlook

Development of high capacity electrode materials for Li-ion and Na-ion battery:

Presently, a single energy storage technology is not able to meet the requirement of future applications including electric vehicles or mobile electronics without compromising on other factors such as cost and safety. Intense research is still being done on the search for new alternatives for the current energy storage technology. The current focus of such research is on developing high capacity electrode materials for Li-ion battery. High capacity and high energy density anode materials for Li-ion battery with improved cyclic stability are still under development. This can be done by tuning the structure, morphology and composition of the active electrode material. The main disadvantage of conversion type anode materials is lower energy efficiency because of the large difference in the insertion and de-insertion potential. Alloy type anode materials are promising candidates as they possess high theoretical capacity as compared to insertion type electrodes and better energy efficiency. Modern Li ion battery development is mainly focused on Si and Sn based anodes. Silicon and tin based materials are ideal anode materials because of their high theoretical capacities 3579 $mAhg^{-1}$ and 990 $mAhg^{-1}$, respectively. However the main disadvantage is the huge volume expansion upon various charge discharge cycles which limits the cyclic stability of the device. Tremendous efforts have already been made to improve the battery performance of Si and Sn based anode. One promising strategy is to make composite of such active material with high surface area carbon. This can improve the cyclic stability of the electrode as the high surface area of the carbon support can compensate for the volume expansion and contraction of the material during insertion and de-insertion, respectively. Hollow carbon spheres with active material encapsulated in it can also use as anode material, as the hollow structure also prevents the pulverization of the electrode due to volume expansion.

One of the major obstacles for expansion of Li-ion batteries for large scale energy storage applications is the limited Li reserves and therefore increasing cost. Another area of research interest is thus to develop a low cost alternative for Li-ion batteries. Sodium ion batteries are considered as the promising candidate for electrical energy storage due the wide abundance and low cost of sodium products and similar

electrochemical intercalation nature of sodium as for lithium. Developing suitable cathode and anode materials for sodium ion batteries is still a challenge because of the larger ionic radius of sodium compared to that of lithium.

Like in the case of Li-ion battery, alloy type materials such as tin, antimony and bismuth etc. are promising candidates for Na-ion battery anode as they have high specific capacity and energy density as compared to other type of anode materials. The major issue is the stability because of the volume expansion and contraction during the charging / discharging cycles. Carbon supports can be used to improve the cyclic stability of the electrode materials. The major drawback of metal based materials is their capacity fading upon cycling. This is due to the volume expansion in the material after number of sodiation and de-sodiation during discharging and charging process. The stability can be improved by making alloys or by increasing the surface area. The surface area can be increased by making nanostructures or by making composite with carbon nanostructures or low dimensional forms. Carbonaceous materials are another option for Na-ion battery anode materials.

Polyanion with NASICON structure are promising candidates for sodium ion battery cathode. However Sodium Vanadium Phosphate (NVP) has low electronic conductivity which limits its capacity at higher charge discharge rate and hence lower power density. It has been observed that coating of NVP with thin layer of conductive carbon can improve the power density as it facilitates the charge transport because of the higher electrical conductivity, electrical contact in the electrode and reduced particle size. Carbon coated NVP can be synthesized *in-situ* by addition of carbon precursor along with NVP precursors. The high temperature heat treatment of the precursor will result in the desired composite of NVP with conducting carbon.

In all the above cases, carbon materials have an important role in improving the cyclic stability as well as the power density of the device. They acts as support for active material for different purposes such as to improve the electrical conductivity and to enhance surface area and accessibility. Different carbon forms such as porous carbon, graphene, hollow carbon spheres etc. can be used as active material support.

Hydrothermal process can be used to synthesize hollow carbon spheres encapsulated with metal nanoparticle (Sb and Sn) for lithium or sodium ion battery anodes.

List of Publications

1. **Dhanya Puthusseri**, Vanchiappan Aravindan, Srinivasan Madhavi and Satishchandra Ogale, *3D micro-porous conducting carbon beehive by single step polymer carbonization for high performance supercapacitor*: the magic of in situ porogen formation, **Energy Environ. Sci.,** 2014,7, 728-735

2. **Dhanya Puthusseri**, Vanchiappan Aravindan, Srinivasan Madhavi and Satishchandra Ogale, *Improving the energy density of Li-ion capacitors using polymer-derived porous carbons as cathode*, **Electrochimica Acta**, 2014, 130, 766-770.

3. **Dhanya Puthusseri**, Vanchiappan Aravindan, Bihag Anothumakkool, Srikumar Kurungot, Srinivasan Madhavi and Satishchandra Ogale, *From Waste Paper Basket to Solid State and Li-HEC Ultracapacitor Electrodes: A Value Added Journey for Shredded Office Paper*, **Small**, 2014, 10, 4395-4402.

4. **Dhanya Puthusseri**, Vanchiappan Aravindan, Madhavi Srinivasan and Satishchandra Ogale, *3D Interconnected Porous Graphene Sheets Loaded with Cobalt Oxide Nanoparticles for Lithium-Ion Battery Anodes*, **Energy Technology** (DOI: 10.1002/ente.201500497)

5. Reshma Bhosale, Rajesh Hyam, **Dhanya Puthusseri** and Satishchandra Ogale, *Chlorate Ion Mediated Rutile to Anatase Reverse Phase Transformation in the TiO_2 Nanosystem*, **Dalton Transactions**, 2011, 40, 11374-11377.

6. Rohan Gokhale, Sreekuttan Unni, **Dhanya Puthusseri**, Sreekumar K, Satishchandra Ogale, *An efficient heteroatom-doped carbon electro-catalyst for oxygen reduction reaction by pyrolysis of protein-rich pulse flour cooked with SiO_2 nanoparticles*, **Phys. Chem. Chem. Phys**, 2014, 16, 4251-4259.

7. Abhik Banerjee, Kush Kumar Upadhyay, **Dhanya Puthusseri**, Vachiappan Aravindan, Srinivasan Madhavi, and Satishchandra Ogale, *Crumpled-sheet-assembled perforated carbon cuboids by MOF pyrolysis: A highly effective cathode active material for ultra-high energy density Li-ion hybrid electrochemical capacitors (Li-HEC),* **Nanoscale**, 2014, 6, 4387-4394.

8. Malik Wahid, **Dhanya Puthusseri**, Deodatta Phase and Satishchandra Ogale, *Carbon from sugarcane bagasse with a new hydrothermal twist: Electrochemically efficient interconnected 3D sheet morphology,* **Energy & Fuels**, 2014, 28, 4233–4240.

9. Shraddha Chhatre, Vanchiappan Aravindan, **Dhanya Puthusseri**, Abhik Banerjee, Srinivasan Madhavi, Prakash P Wadgaonkar and Satishchandra Ogale, *High surface area porous carbon for ultracapacitor application by pyrolysis of polystyrene containing pendant carboxylic acid groups prepared via click chemistry*, **Materials Today Communications,** 2015, 4, 166-175

10. **Dhanya Puthusseri**, Yogesh Gawli, Malik Wahid, Ajay Kumar and Satishchandra Ogale, *Nitrogen and Phosphorous co-doped carbon derived from phytic acid doped polyaniline pyrolysis as stable anode material for Sodium ion battery*, **Manuscript under preparation.**